FLOW CONTROL OPTIMIZATION IN A JET ENGINE SERPENTINE INLET DUCT

A Thesis

by

ABHINAV KUMAR

Submitted to the Office of Graduate Studies of
Texas A&M University
in partial fulfillment of the requirements for the degree of

MASTER OF SCIENCE

August 2007

Major Subject: Aerospace Engineering

FLOW CONTROL OPTIMIZATION IN A JET ENGINE SERPENTINE INLET DUCT

A Thesis

by

ABHINAV KUMAR

Submitted to the Office of Graduate Studies of
Texas A&M University
in partial fulfillment of the requirements for the degree of

MASTER OF SCIENCE

Approved by:

Chair of Committee,	Othon K. Rediniotis
Committee Members,	Paul Cizmas
	Luis San Andres
Head of Department,	Helen L. Reed

August 2007

Major Subject: Aerospace Engineering

ABSTRACT

Flow Control Optimization in a Jet Engine Serpentine
Inlet Duct. (August 2007)
Abhinav Kumar, B.E., Mumbai University
Chair of Advisory Committee: Dr. Othon K. Rediniotis

Computational investigations were carried out on an advanced serpentine jet engine inlet duct to understand the development and propagation of secondary flow structures. Computational analysis which went in tandem with experimental investigation was required to aid secondary flow control required for enhanced pressure recovery and decreased distortion at the engine face. In the wake of earlier attempts with modular fluidic actuators used for this study, efforts were directed towards optimizing the actuator configurations. Backed by both computational and experimental resources, many variations in the interaction of fluidic actuators with the mainstream flow were attempted in the hope of best controlling secondary flow formation. Over the length of the studies, better understanding of the flow physics governing flow control for 3D curved ducts was developed.

Blowing tangentially, to the wall at the bends of the S-duct, proved extremely effective in enforcing active flow control. At practical jet momentum coefficients, significant improvements characterized by an improved pressure recovery of 37% and a decrease in distortion close to 90% were seen.

DEDICATION

I dedicate this thesis to all my aggie friends for their constant support and affection and most importantly to my family back home in India who is the very reason for whatever little I have achieved.

ACKNOWLEDGMENTS

I would like to sincerely thank Dr. Othon Rediniotis for an opportunity to contribute to this project and for his continual support and guidance in my education and research. I also thank my committee members, Dr. Paul Cizmas and Dr. Luis San Andres, for their support and advice.

I extend thanks to my fellow graduate students involved in this project, Aaron Kirk, Nathan Tichenor and Gaurav. Success of this project can be undoubtedly attributed to their help and assistance at every phase. Additionally, I would like to thank Dr. Lance Traub, whose expert knowledge and advice on experimental aerodynamics has been invaluable.

This acknowledgement would be incomplete without a mention of the technical staff at Texas A&M University Aerospace Engineering Department, Joshua Wiemar and Rick Allen; their help in the fabrication of the many complex parts that this project required has also been invaluable.

Finally, I would like to thank Dr. Rhett Jeffries from the Air Force Office of Scientific Research for the generous grant that allowed this research to be possible.

TABLE OF CONTENTS

LIST OF FIGURES

Page

Page

Page

Page

LIST OF TABLES

INTRODUCTION

General

Advanced jet engine inlets are increasingly evolving into complex serpentine geometries. Serpentine inlet ducts as opposed to conventional diffusing ducts tremendously increase the stealth capabilities of an aircraft by reducing infrared and radar signature. An S – shaped inlet can essentially block the line of sight of a compressor intake thus sealing it from incoming radar waves along with the prevention of the heat signature being sent out by hot gases produced in the combustor.

The benefits of using serpentine ducts are further realized in reduction of aircraft weight and size. These features prove more beneficial for Unmanned Aerial Vehicles (UAVs) which offer lesser size and design constraints as opposed to manned aircraft which have to accommodate for cockpit and support systems. Studies have estimated a significant weight and size reduction of UAVs through use of serpentine jet engine inlets.

In spite of the aforementioned benefits which are offered through use of serpentine ducts, they induce significant flow distortion at the engine inlet, detrimental to the engine performance, mechanical performance of the blades and fuel efficiency. Inlet flow distortion is a serious issue and has been a matter of concern for many previous aircrafts including F-111, F-14, Mig 25, A300 etc[1].

This thesis follows the format of the *AIAA Journal*.

Flow distortion, which is mainly attributed to the presence of large secondary flow vortices, is characterized by presence of zones of extremely low pressure recovery. The rotor when passing through the low pressure zones can be subject to fluctuating stresses which can lead to severe fatigue loads. Since the flow in these low pressure zones enters at large oblique angles with respect to the compressor due to large rotational components in the plane of the engine face. They can result in a rotational stall analogous to the stall over an airfoil at high angles of attack. Flow control is employed to reduce flow distortion and enhance pressure recovery for the internal flow in such ducts. This thesis presents results from flow control attempts on a similar inlet duct as part of ongoing research at Texas A&M University.

Background

Subsonic internal flows are commonly found in most contemporary air breathing systems. The inlets often show variations in cross section and curved centerlines. Apart from the viscous effects resulting in thick boundary layers, there are strong secondary flow structures which can have detrimental effects on both engine health and performance. Secondary flow structures are specific to geometric variations, bend steepness etc, and hence every case poses a need for careful flow investigations to gain an understanding of the extent and nature of distortion. Apart from separation at bends of high gradient, curved ducts show a classical pattern of counter rotating vortices, a result due to a pressure differential in the near-wall regions of the duct[2]. The flow towards the inside sees a steeper bend resulting in higher acceleration and subsequently higher velocity as compared to the flow in the outer regions of the duct. The slow moving flow near the boundary layer immediately reacts to the pressure drop due to increased velocities and starts to migrate towards the inside of the duct. The flow in the core region is pushed towards the outside due to centrifugal effects leading eventually to two counter rotating vortices as seen in Figure 1. A typical S-shaped Duct would have two bends which would result in two locations for vortex liftoffs. The vortices at the first bend would have more time to diffuse and hence would be weaker at the engine face than the distortion caused due to the second bend, which would have traveled a shorter length. Hence the engine face would see one strong and a mild pair of counter-rotating vortices.

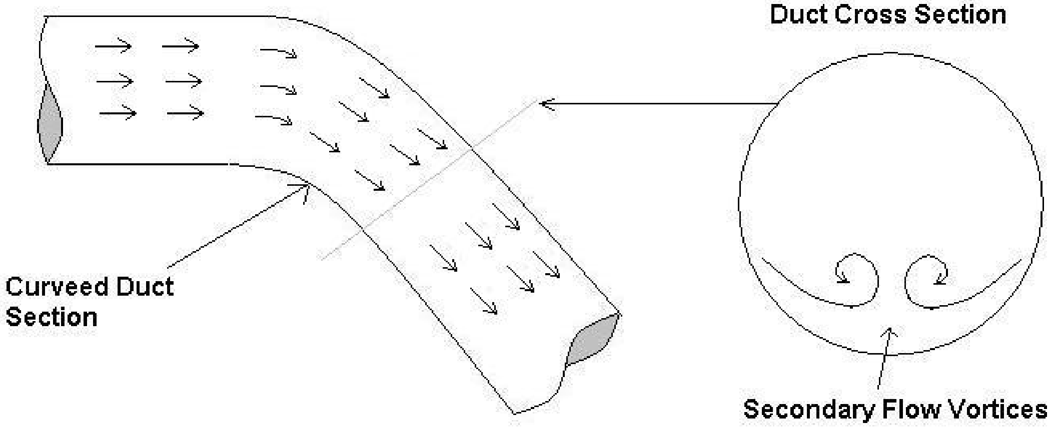

Figure 1: Secondary flow vortices in a curved duct

Many researches including Scribben, Ng and Burdisso[3, 4] have tried to analyze the distortion is serpentine ducts with reference to engine performance. It is realized that though curved serpentine inlets have various benefits over conventional inlets, the flow distortion is significant enough to actually offset the advantages. This has opened new areas of interests in the field of flow control, to provide remedies for controlling distortion due to bending of the centerline. Flow control has grown to become a fairly developed field and encompasses various techniques and procedures which have proven effective for many previous flow distortion problems. Flow control evolved from passive control techniques which included guide vanes and vortex generators. Though these methods are fairly effective, a need was realized for active control techniques for higher effectiveness or control of complex secondary flows. Fixed passive control structures pose further disadvantages as opposed to active flow control methods which will be discussed shortly. Flow control devices may simply energize the flow by adding high momentum fluid or may introduce a specific vorticity which may counter the secondary flow vorticity. The former technique works better for separation delay or control while the latter proves more effective for curved ducts where secondary flow vortices are dominant in distorting the primary flow. This thesis provides analyses employing both techniques, however due to the presence of heavy secondary flow vortices, use of vorticity introduction into the flow field would be discussed more extensively. Many secondary flow control attempts have been made with remarkable success through the use of vortex generator vanes. A study carried out by the NASA/MOD Joint program[1] on the M2129 S duct showed through the use of CFD that not only vane vortex generators prove effective for a wide range of boundary conditions; they reduce engine face distortion and flow unsteadiness by upto 80%. In a similar attempt Anabtawi et al.[5] used flat plate vortex generators on a curved diffuser designated for use with the BWB concept. Their experimental analysis show significant improvements in engine face distortion through alteration of the flow structure and separation control. Various other efforts including those by Reichert and Wendt[6, 7] derive positive conclusions.

In spite of the aforementioned successful implementations, passive flow control possesses serious deficiencies in terms of adaptability with the change in boundary conditions, a requirement, increasing realized for tackling dynamic flow complexities. Passive flow devices are physically intrusive hence come along with a drag penalty as stated by Sullerey et al.[8]. Moreover in the eventuality of mechanical failure, VG vanes can be sucked into the compressor posing serious hazards. Contrary to fixed vane vortices, active control offers a control loop and hence the ability to adjust to the flow conditions. Micro-jets are seen widely used for flow control applications. Micro-jets which are characterized by high momentum and low mass flow through small orifices enhance mixing between high and low energy layers finally leading to delay or suppression of separation. Kumar and Alvi[9, 10] used an array of 400μm microjets on a simple Stratford ramp (Figure 2).

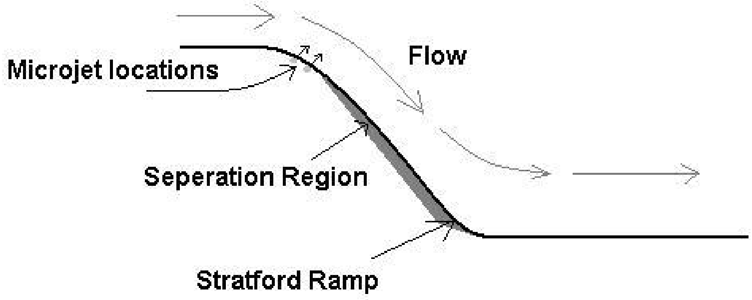

Figure 2: Stratford ramp[9]

Compressed nitrogen was used for actuation as it has properties comparable to air. The studies showed successful suppression of flow separation due to adverse gradients created by the ramp through use of micro jets actuated at super sonic velocities. A study conducted at the Indian Institute of Technology[8, 11] used 4mm diameter jets at varied skew and pitch angles with respect to the mainstream flow to counter vorticity of secondary flows in addition to reenergizing the boundary layer through turbulent mixing. Such a control is governed by the principle of vorticity signature which states, secondary flow control is achievable through governance of the strength and orientation of vorticity being introduced by flow control devices. This technique is likely to be more effective for controlling engine face distortion as it globally restructures the flow through introduction of opposite vorticity into the secondary flow field. In all previous micro-jet studies, the possibility of altering the interaction of jets with the mainstream flow through variation of jet slot geometry and orientation could not be explored. Recent advances have used synthetic jets ejected through rectangular slots instead of small circular orifices as the case with micro-jets. The synthetic jets through straight slots are capable of introducing vorticity into the flow along with mixing of boundary layer with mainstream flow. Research conducted at Georgia Institute of Technology by Amitay et al.[12] demonstrated the use of synthetic jets through rectangular slots. The duct used by them however was a simple two dimensional diffuser hence the flow was deficient of secondary flow vortices. The researchers used a rectangular jet slot array arranged in the stream-wise location placed within the flow separation region. They used 17 slots which were individually addressable to control the span-wise non-uniformities in separation. The jet velocities were limited to 11 m/s at an excitation frequency of 1032Hz. The researchers were able to demonstrate complete flow reattachment up to a velocity of 75 m/s (M = 0.2) and a partial reattachment up to a velocity of 105 m/s (M = 0.3).

In a similar research carried out at Virginia Polytechnic Institute and State University[13], flow control through the use of synthetic jets was attempted on a 2-D serpentine inlet. Suction plenum was placed close to the separation location immediately followed downstream by the blowing plenum. Suction was achieved through suction holes towards the inlet duct profile while blowing holes were made to blow almost tangential to the surface of the duct to add maximum tangential momentum to the flow than momentum normal to the surface. Suction and blowing was achieved individually through use of compressed air; ejector pumps powered by compressed air were used to create low pressure forcing air out of the suction plenum. Plenum chambers were required for uniform flow through all the holes. The researchers used sensitive microphones to detect transition from laminar to turbulent boundary layer hence offer much insight on the flow characteristics including separation location and intensity.

Though most of the above discussed studies worked extremely well for 2D serpentine duct/diffusers, the principle of vorticity signature could not be well demonstrated. Straight slots as discussed earlier can be used to induce desired vorticity in the core flow by careful manipulation of the slots orientation. In a study conducted by Bridges and Smith[14], the orientation of the orifice slot was shown to have significant influence on the interaction of the jet with boundary layer and mainstream flow. They tried different yaw angles (the angle between the axis of the slot and velocity vectors) to document the relationship of yaw angle with vorticity. As stated earlier, at 0° yaw angle the synthetic jet introduced a pair of counter rotating pair of vortices with stream-wise vorticity. Though the origin of vortices from a jet is still not quite clear, the relation of the yaw angle with vorticity is being understood. In this study, as the yaw angle was slowly raised the vortex upstream of the slot diminished while the one downstream of the slot strengthened (Figure 3). This lone vortex was however observed to be closer to the wall as compared to counter rotating pair for the zero yaw case, a clear indication towards a decrease in penetration ability of the jet with increase in angle. These results were verified by CFD analysis presented in the results section of this thesis. CFD analysis showed an almost complete disintegration of vorticity at higher angles (40°). Clearly the control of vorticity simply through the change of orientation pointed at the possibility of countering secondary flow vorticity through use of jets.

Hence, having explored all the features and characteristics of fluidic actuators with rectangular slots, they were found to be more appropriate for the duct geometry being studied in the current research. Moreover the fluidic actuator models designed for this particular application is are driven by a centrifugal fan, blowing the same air derived from the suction module back into the duct. This eliminated the need for external flow for bleeding requiring pressure chambers and complicated plumbing, clearly not feasible for realistic applications.

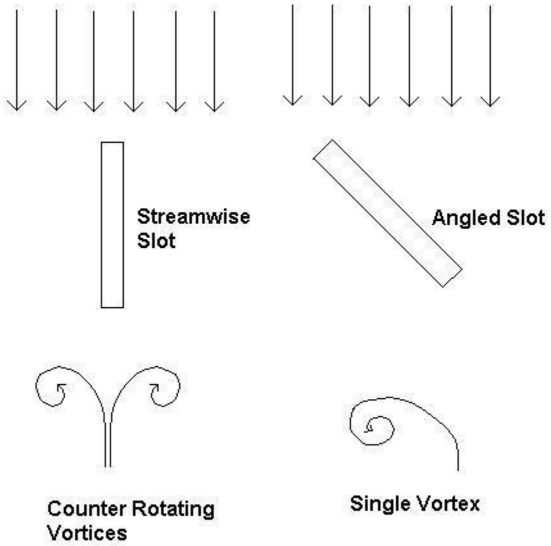

Figure 3: Effect of orientation on the interaction of synthetic jet with flow

Further to the numerous studies done in the area of flow control applied to serpentine ducts, much research work was carried out at Texas A&M University as part of the initial attempts made to understand the duct flow characteristics and evaluate distortion suppression methods[15]. Most of the setup used during these tests remained mostly unchanged over the entire analysis phase and is presented in the setup section of this thesis.

Surface flow visualization tests were carried out on the duct model as part of initial investigations to better understand and recognize the separation locations along with secondary flow vortex liftoff locations. Titanium dioxide particles suspended in an organic medium was applied to the whole duct to generate oil traces on the walls. The heavier titanium dioxide particles adhere to the wall while, the organic medium quickly evaporates during test conditions. The traces are created by viscous shear stress components dictated by the flow conditions at the wall. Figure 4 shows the formation of vortices through wall traces at the first bend cross section of the duct. The picture shows a clear span wise separation pattern indicated by an abrupt transition from laminar wall traces to extremely turbulent ones. The Vortex cores depict the liftoff locations for the counter rotating vortex pair. Further insight into the flow pattern was gained by careful investigations of the wall traces.

Figure 4: Flow visualization

Even though it was understood, suction by itself was not expected to significantly reduce flow distortion, removal of low energy boundary layer could delay flow separation or even prevent the flow from separating. To study the effects of pure suction, tests with suction itself were carried out. The suction plenum was directly connected to vacuum pumps capable of delivering high pressure differentials. High mass flow rates, at an inlet Mach of 0.18 through the throat, as opposed to a Mach of 0.09 which was used for the tests discussed in later section of this thesis, were used. The suction was measured as the percentage of total mass flow entering the duct. Suction amounts of

1.25%, 1.75% and 2.25% were applied to develop a relation between amounts of suction pressure recovery. As expected, the separation location was pushed further downstream by application of suction at the bends indicated by wall static pressures. However an increase in suction did not aid in delaying separation any further but pressure recovery was greatly increased. However as discussed earlier, the migration of boundary layer could not be avoided as suction could not impose any countering vorticity in the flow field. As compared to the baseline, suction of 2.25% greatly increased pressure recovery but could do little to decrease the extent of distortion as shown in Figure 5. The factor Cp_{loss} is defined in equation (2) presented in the setup section of this thesis. However a suction of as much as 2.25% of the total mass flow rate entering the duct would be too expensive to realize in practical applications.

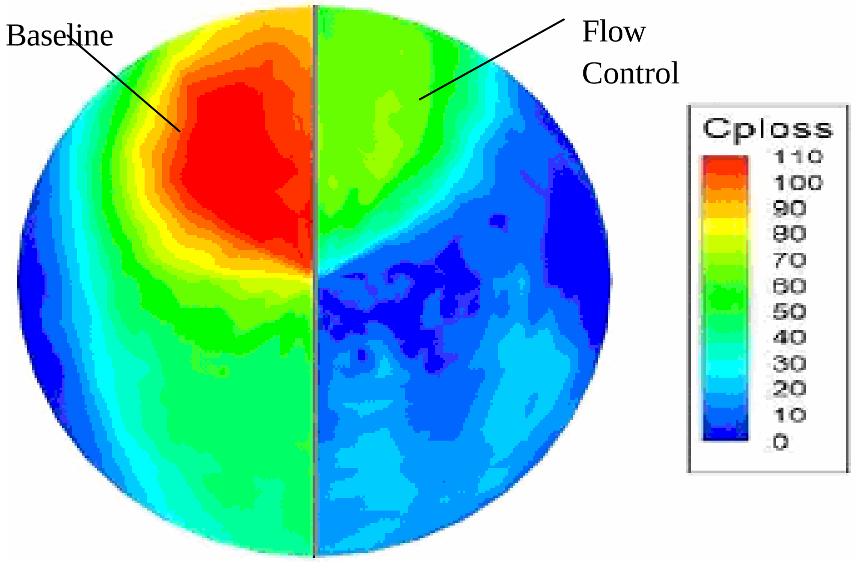

Figure 5: Effect of pure suction at engine face

Suction and blowing is realizable and practical for real applications. Blowing was achieved through venting the high pressure air from the suction plenum in the blowing plenum. The actuator used for this application is discussed in detail in the later sections of this thesis. Suction and blowing tests were carried out at velocities of 30 m/s (Mach = 0.09) and the tests were carried out over a range of C_μ's which is simply the combined momentum through the blowing slots normalized by the total momentum entering the duct. Blowing and suction at the bends showed a certain improvement over the baseline results for high values of C_μ, however for smaller values there were no significant improvements. Higher amounts of blowing however showed an increased pressure recovery and lower amounts of distortion which were gauged by DC_{60}, a distortion descriptor defined in equation (3) given in the setup section. Interestingly the distortion was reduced even though the jets introduced zero net vorticity into the flow through stream-wise jet slots. Figure 6 shows engine face total pressure loss plots for the suction blowing case for the maximum attempted C_μ of 0.024 against the baseline pressure loss contours.

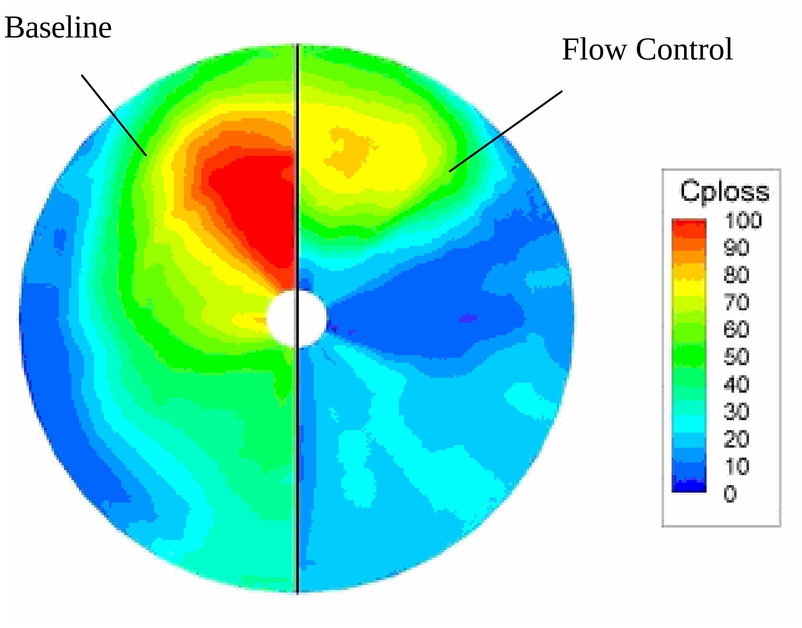

Figure 6: Effect of suction-blowing at engine face

CFD Analysis

CFD analysis is probably the first step in the field of fluid flow analysis. A sound CFD analysis was necessitated by the obvious need for a good understanding of the baseline flow of the inlet duct. Various CFD studies have been conducted on inlet ducts with or without flow control with the aim of accurately modeling the phenomena and the effects of flow control[2, 16]. Accuracy of CFD modeling is dictated by various parameters. CFD validation and accuracy is a topic always open to debate and hence has to be carefully dealt with. Marvin[17] states that CFD research is still led by issues related to flow physics understanding, validation and modeling. Few of the more commonly encountered issues include appropriate mesh generation, specification of boundary conditions, selection of the correct turbulence model and scheme, manipulation of model constants and under-relaxation parameters, etc. These issues are particularly important as they are in general very specific to the flow physics and the problem itself.

In this particular study, CFD results were compared with experimental results for validation. Worthy results were used to further probe into more intricate details of the flow which could not be captured by experimental results. They were also used to guide future experiments and actuator designs. Most experimental investigations were pre-tested using CFD. Many researchers have done CFD analysis on complex internal flows similar in characteristics to the geometry in investigation. Peifen and Jue[16] performed simulations on a similar inlet for a cruise missile under maneuvers. They used a Renormalization Group (RNG) k – e model along a with a two layer zonal wall model for capturing near wall phenomenon, to solve RANS in 3D curvilinear system. They demonstrated a good agreement with experimental results and repeated the simulations for various flight conditions. These simulations are particularly helpful in cases where flight conditions are difficult to achieve in laboratory such as a missile under steep maneuvers. They also aid in probing into details which are otherwise very difficult to look into using conventional experimental techniques. Most experimental techniques are intrusive except PIV, LDV etc which are difficult to use for internal flows. Conventional techniques, even though easy to use, have issues such as resolution of various time scales and length scales, even more dominant when examining near wall regions. Though CFD has various benefits over experimental anaylsis especially pertinent to the case at hand, formulation is always an important issue and requires careful deliberation. Grid generation is unarguably the most significant step in pre-processing. The grid represents the numerical domain where eventually the conservation equations are solved. It is therefore important to have an appropriate mesh with the right quality. Xiong, Ya, Changsheng & Yutao[18] demonstrate the use of custom grid fitting techniques using mapping and controlling functions for grid concentration near boundary and shock propagation regions in their simulation on a ramjet inlet. While custom grid fitting offers more control on the desired quality and scheme of mesh, it is recommended for simple 2D or axisymmetric geometries only. For complex 3D geometries such as the serpentine duct, it is usually advisable to use commercially available codes such as GRIDGEN, ICEM, GAMBIT etc. as they offer various control features for appropriate grid generation. Bahar et al.[19] demonstrated the use of commercial grid generation codes to generate a mesh around a medium range cargo aircraft. In spite of an Euler solution, the geometric complexities forced various grid variations in terms of scheme and concentration. They controlled the grid by surface mesh generation which is particularly important in handling highly curved regions (localized areas of high gradients which tend to concentrate streamlines). Most codes are able to generate structured, unstructured and hybrid grids which is desirable for modeling complex geometries such as the inlet duct. They also provide the feature of graphical representation of the mesh created, which gives a chance for visual examination.

Complex flows need to be given much thought before the right model or scheme can be decided upon. Traditionally many attempts have been made in literature to employ custom codes for modeling complex flows. Ding and Weng[20] modeled separation on a missile inlet using similar practice. They tested the standard k – e model and the RNG $k - e$ model to make a distinction between the two and use the one more appropriate for their case. Selection of the right model is rarely intuitive and must be validated before results can be relied upon. This often requires simulations with different models and schemes to facilitate the selection of the one which most closely resembles experimental results. Most commercial codes include most of the widely accepted models and hence give a chance to compare the results with little effort. Advancements in commercial CFD allow geometries to be imported directly from solid modeling software; this eliminates the need for defining databases for geometry-description. Taskinoglu and Knight[21] exported an inlet duct geometry designed in commercially available CAD program Pro/Engineer and later exported it to commercial grid generation code GRIDPRO/az3000. They finally solved the 3D flow problem in GASPex using a Wilcox $k - ?$ model. The technique discussed in the above example is convenient and easy to implement. Most of the commercial codes are able to provide similar interfacing.

Many flow control applications including the ones used in this study are difficult to implement in experimental analysis. Their orientation, positioning and profiles are very crucial for their effectiveness. It is an expensive routine in experimental analysis to try all likely configurations and possibilities before identifying the one most effective for the specified problem. It is in scenarios like these, where CFD analysis proves extremely effective. Researchers have tried incorporating passive and active flow control devices in CFD models to test their effects[22]. In passive control techniques, micro-vanes and vortex generators can be easily integrated to a geometry using a standard 3D modeling software. These geometries can then be exported to a Grid generation code and appropriately meshed. In case of active flow control, actuators can be integrated by simply specifying the designated body surfaces as desired boundary conditions, either constant or periodic depending on the type of control. If well formulated, these simulations show a very good match with experimental results. Jirasek[22] successfully demonstrated the efficacy of vortex generators for flow control in an RAE M2129-S duct using a novel vortex generator model termed as the jBay model. It was clearly argued that since both geometrical characteristics of the VGs (Vortex Generators) and their orientation highly depends on the flow characteristics and the type of problem, it is highly recommended to use advanced CFD in conjunction with experimental analysis. Through careful use of CFD, good agreement between experimental and computational results was achieved. Success in active flow control techniques which may require suction or blowing through actuators has been demonstrated as well.

SETUP AND PROCEDURE

CFD Problem Setup

The inlet duct geometry has an extremely complex definition. Unfortunately there is little literature available on the development and evolution of complex and secondary flow structures which eventually distort the flow. Difficult flow physics and geometry made the inlet duct a particularly challenging CFD problem. Issues ranging from mesh generation to turbulence model selection posed unique challenges. As stated earlier in this text, attempts have been made to model similar geometries[2, 22] however these problems are very sensitive to minor changes in offset angles and cross-sectional variations. Moreover the M2129-S duct modeled by Jirasek is simpler than the geometry tested in this study. The problem however was approached in a stepwise and systematic fashion.

Grid

The geometry being symmetric about the mid plane allowed the use of only half of the actual geometry spilt about the mid or symmetry plane. It is a well accepted practice to break a complex geometry into multiple domains and grid them individually as pointed by Gribben, Badcock and Richards[23]. Discretizing the domain into multiple zones gives more control over the mesh type and quality; this allows meshes to be specific to the zones giving the flexibility of choosing the ideal scheme and density. The inlet duct geometry was subject to the same treatment, the geometry was split into thirteen domains using the 3D modeling software SOLIDWORKS and this proved advantageous in defining the splitting planes as shown in Figure 7.

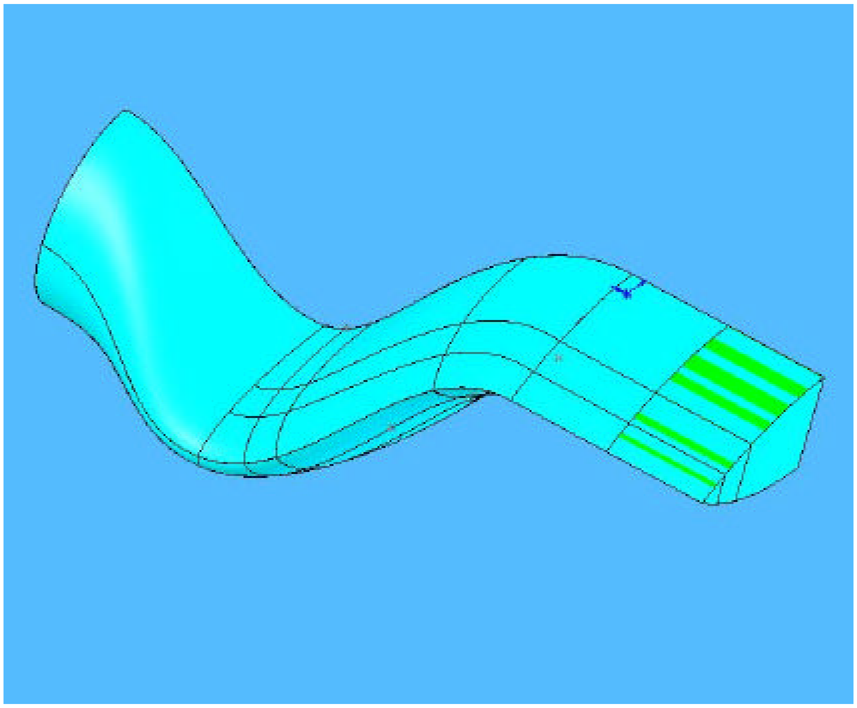

Figure 7: Duct geometry showing multiple zones

Even though the grid itself is generated as multiple segments, the final grid is connected and is treated by the solver as a continuous grid without intermediate boundaries as depicted in Figure 8.

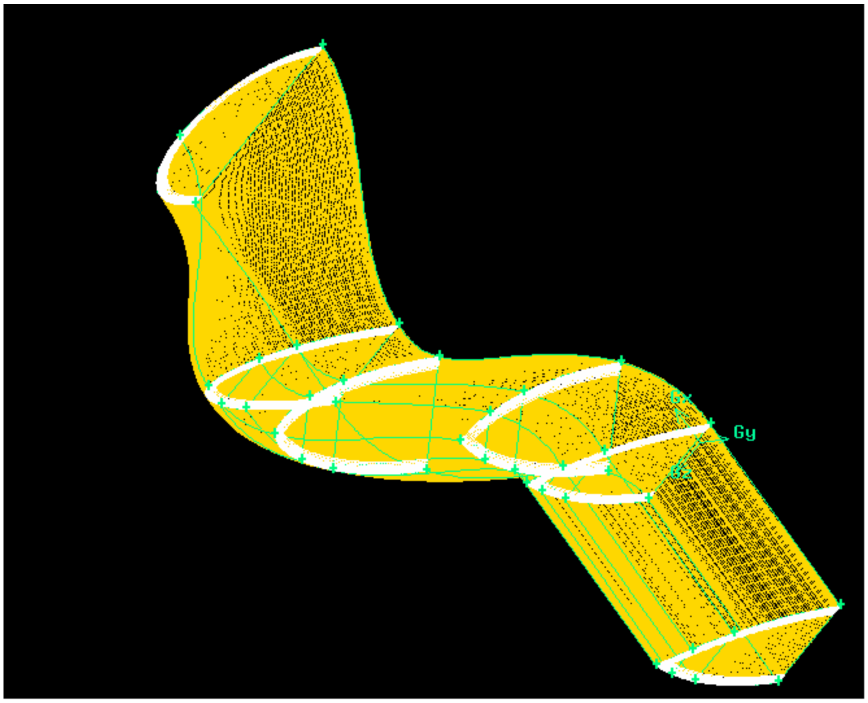

Figure 8: Final mesh generated on the multi-block grid

The final grid is hybrid and consists of a combination of both structured and unstructured meshes with varying schemes in different domains as shown in Figure 9.

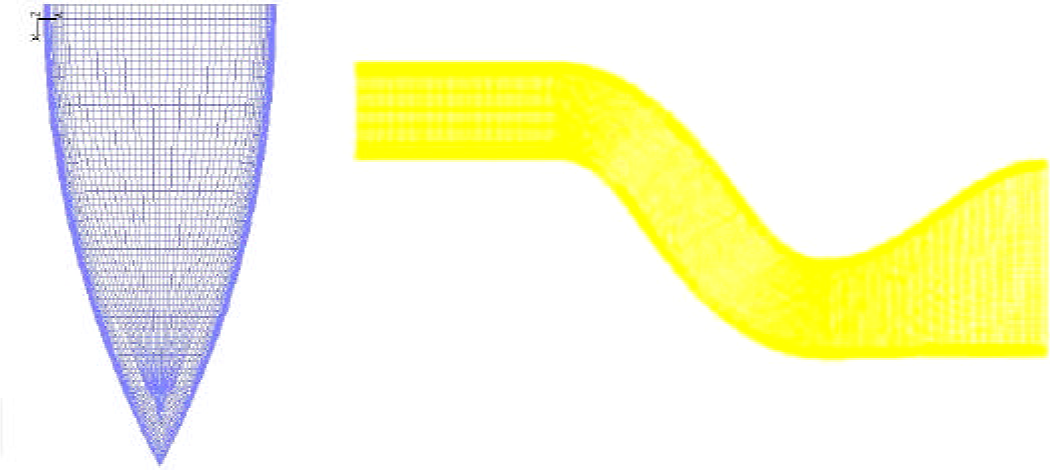

Figure 9: Inlet face and symmetry face grid

Grid quality is often an issue which is easily overlooked in computational analysis and its consequences greatly undermined. Grid quality can significantly affect the results and lead to erroneous conclusions as clearly pointed by Logan and Nitta[24]. They pointed out that ideally a solution should be grid independent however this may never be perfectly attainable. Grid convergence simply refers to the ability of the grid to least interfere with the solution. It may be stated that this does not assure the trustworthiness of the solution as there are many other issues to CFD validation which are foreign to grid convergence. The simplest test for grid convergence is the usage of three different meshes with varying quality starting from coarse to fine. Grid convergence is assumed if there is a fair agreement between the results from the different meshes. For the inlet duct geometry, three individual meshes with varying mesh quality are generated. The node density among these grids varies with the ratio of 1:2:4 implying the medium quality having twice as many nodes as the coarse one and the fine grid having four times as many as the coarse grid as depicted in the Figure 10 showing the grid at the outflow faces of the three grids.

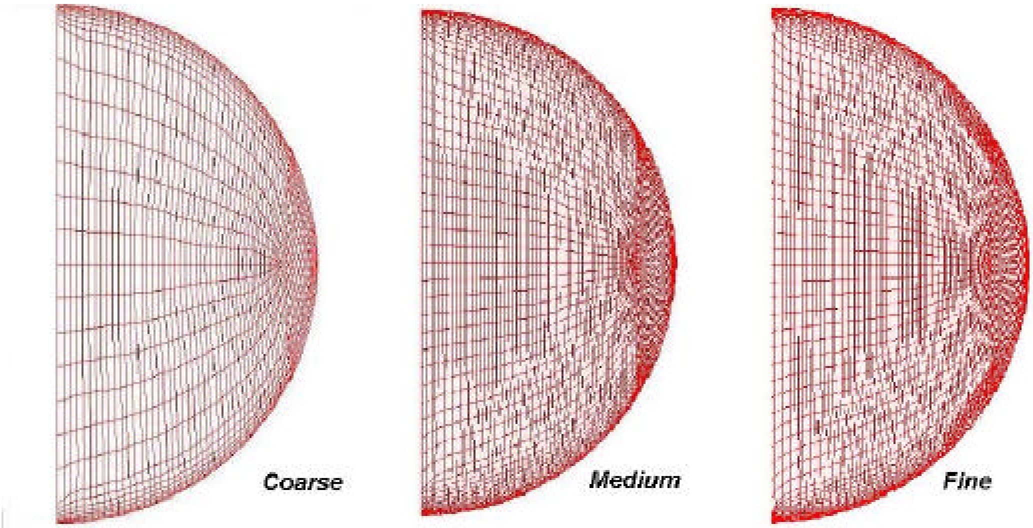

Figure 10: Mesh at outflow face

The baseline simulations were run on all three meshes for testing grid convergence. All three instances had the same setup and the residuals were allowed to fall below a particular specified level. Figure 11 shows the total pressure contours at the outflow faces of the three meshes.

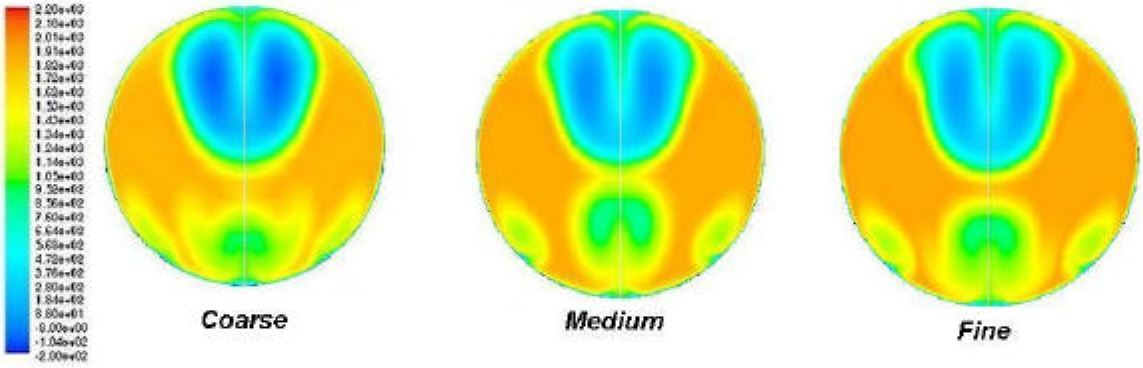

Figure 11: Total pressure contours at outflow

Even though there are significant differences in the three results, the fine and the medium meshes show a fair agreement for practical purposes. Hence the medium quality mesh is used for all computations to save on computation time which would otherwise be expensive on the fine mesh.

Problem Definition

The accuracy of a CFD simulation depends almost entirely on the problem definition. Correct selection of boundary types and specification of boundary conditions along with the correct model for turbulence or laminar flow is most crucial. The type of scheme and order can affect the accuracy as well; however these parameters can be traded off with computational cost if desired. The flow through the inlet geometry was well below 0.3 local Mach number, hence incompressible assumptions were acceptable. The selection of the correct boundary type is often more complex than apparent in most cases. The boundary types must be able to replicate the test scenarios to a reasonable level. The selection is hence governed by the understanding of the flow characteristics at the boundary planes. Presence of reversed vectors at the exit planes, compressibility effects, wakes, turbulence levels and leakages can have significant effects on the problem definition. Often characteristics or Riemann invariants are used to impose the correct boundary conditions for complex problems as stated by Bahar et al.[19]. For the inlet duct geometry the incompressible flow assumption holds well, also the inlet velocity is known, experimental results show no evidence of reversed flow vectors at the engine face. Moreover the static pressure at the engine face is unknown and non uniform which made velocity inlet - outflow combination as the ideal choice for the specified problem. FLUENT features velocity inlet boundary conditions which provide the option of specifying magnitude normal to the face or individual velocity components and also the turbulence data for turbulence models. The outflow boundary condition can be used in cases where the exit plane velocity and pressure are unknown and/or non uniform as in the case with the inlet duct, provided the compressibility effects can be neglected.

Selection of the correct turbulence model is probably the most important step in CFD problem setup. A well posed problem on a good grid can give highly erroneous results as a result of inappropriate model selection. For the inlet duct geometry the standard k-e, k-e (RNG) and the k – ? (SST) model were considered. The standard k-e model incorporates the transport equations for k (turbulent kinetic energy) and e (dissipation rate) along with the five standard conservation equations. The k-e model lacks molecular viscosity and hence is unable to capture effects very close to the wall (especially the laminar sub-layer) and relies on wall function for near wall profiles, it is thus preferred for fully turbulent flows. The RNG model uses the instantaneous form of the Navier-Stokes equations through a mathematical concept called “Renormalization Group” (RNG). It features model constants different from its standard k-e counterpart and also has additional terms in the evolution equations of k and e. The RNG k-e model has been observed to give slightly better results than the standard k-e model. The SST (Shear Stress Transport) k – ? model acquires its name from its ability to account for principal shear stress along with turbulent viscosity. The SST model has advantages over both the standard k – ? and the standard k-e model. It also encompasses a cross diffusion term and blending functions for correct behavior in both near and far wall regions. The standard k-e and the standard k – ? models were tested on the inlet duct and their results compared to experimental results. It is in general very difficult to have an exact match between computational and experimental results especially for a complex geometry given the constraints for mesh generation and lack of sufficient understanding of flow physics. For practical purposes such as flow control in this particular study, defining parameters such as separation and vortex lift-off locations, total pressure loss, vortex patterns, separation frequency are good enough comparisons for trusting CFD results. The k – ? model came closest to the experimental results in the comparison study which is visible in the total pressure contours at the engine face shown in Figure 12.

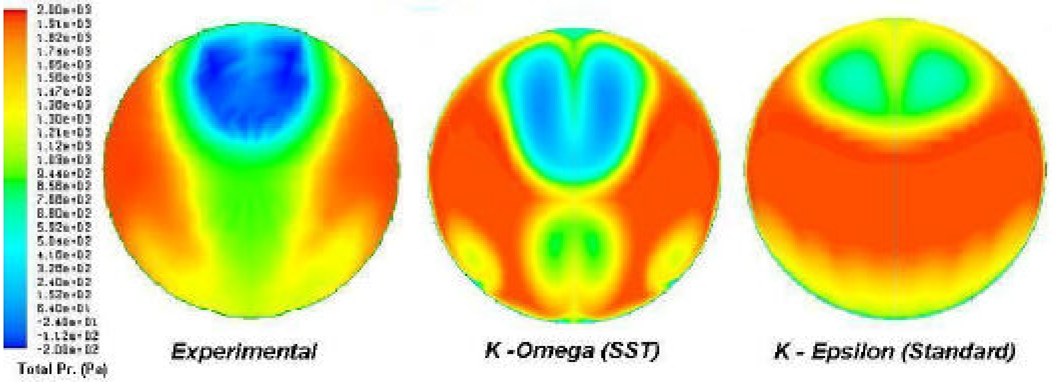

Figure 12: Comparison of turbulence models to experimental results

The k – ? SST model by definition is better equipped to handle the inlet duct geometry as it is able to handle both near wall and far wall effects similar to the k-e RNG and the two layer zonal wall model used by Peifen and Jue[16] for modeling flow inside a cruise missile inlet under maneuvers. The k-e model under-predicts separation and boundary layer location hence showing weak vortices formed due to the second bend. It, however, completely fails to show separation at the low gradient first bend depicting the model's short-coming to capture the laminar sub layer resulting due to absence of molecular viscosity. The k – ? SST on the other hand correctly predicts the location of separation at both bends as well as the correct boundary layer migration pattern. It shows two pairs of counter rotating vortices from each of the bends replicating the classic two bend duct flow pattern.

The problem setup often requires specification of various parameters other than model and boundary conditions, solver selection being an important step of formulation. FLUENT allows for choosing between coupled or segregated solvers. Solvers in general deal with the way conservation and other evolution equations are discretized. The segregated solver sequentially solves the conservation equations, it updates properties which are then used to solve for velocities in the momentum equation and the values may then be updated by using a pressure velocity coupling obtained through the momentum equation. Finally the energy equation is solved and species and turbulent stresses are updated and the solution is tested for convergence, if the convergence criteria are not met the steps are repeated. The coupled solver on the other hand solves for all conservation equations together and updates turbulent stresses before checking for convergence. The segregated solver is the preferred solver for incompressible problems such as the low speed flow through the inlet duct hence making it the right solver for the problem in hand. The Segregated solver can only accept an implicit scheme which is the preferred formulation for problems which may pose strict or complex stability conditions. Other parameters include using a steady state solver for a steady state solution as desired by the problem and a cell based gradient method ideal for an FVM formulation. Further controls include type of pressure velocity coupling, under-relaxation parameters and discretization of individual flow variables. For the specified case second order discretization was selected for all variables including pressure, momentum, turbulent kinetic energy and specific dissipation rate. A simple pressure – velocity coupling suitable in most cases was specified and under – relaxation parameters were varied during the initial iteration to speed up or slow down convergence to resolve stability issues if any. As for convergence, the individual variable residuals were allowed to drop down to significantly low values, in most cases the residuals either almost ceased to drop any further at these values or dropped at a very slow rate. Researchers suggest that for convergence the residuals must drop to at least three orders below the starting value and most of them did drop below 1E-4 which satisfied the convergence criteria given the start values as shown in Figure 13 depicting the residuals for the baseline simulation.

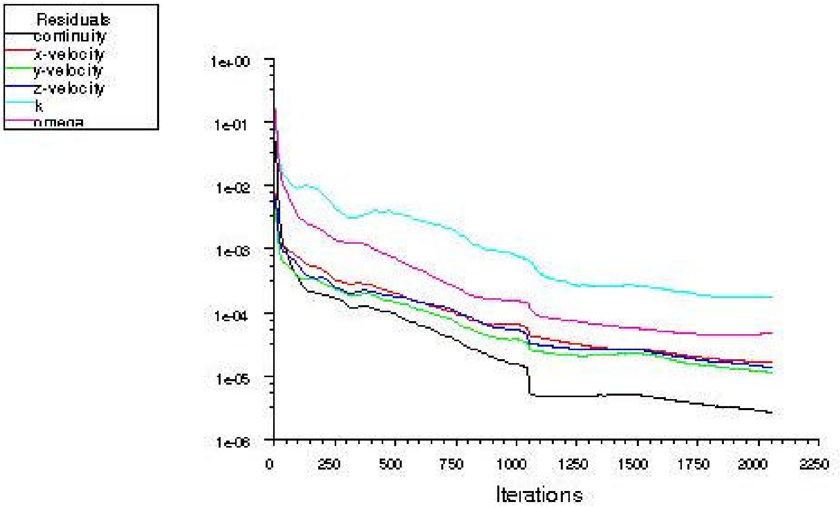

Figure 13: Residuals for baseline simulation on k – ? SST model

Experimental Setup

This section will discuss the experimental setup used for the various experiments carried out as part of this research. The overall geometry and specifications of the duct will be discussed followed by a brief description of the fiberglass sections developed as part of the previous research including the actuator designs. Most importantly the various actuator configurations will be explained, developed as part of the ongoing research. Finally the wind-tunnel setup along with the various data acquisition systems including both hardware and software will be discussed.

Compact, Serpentine Jet Engine Inlet Duct

The Serpentine inlet duct provided by Lockheed Martin had a fairly complex geometry as compared to the relatively simpler curved ducts such as the M2129 S duct[6, 7, 25, 26] geometries used in earlier studies. The inlet duct geometry shown in Figure 14 is divided into a number of clearly divided sections. The duct consists of a Bell-mouth

Section, Constant Area Section, Forward Effector Pack, Offset Section, Aft Effector pack and finally the Cross-Section Transition Section. The Bellmouth with a contraction ratio of 7.4 and a length of 10” provides for a uniform, low turbulence flow field also preventing separation at the lip of the inlet section. The constant area section spanning 10” in length and an aspect ratio of 4 acts as the inlet section leading the duct flow to develop.

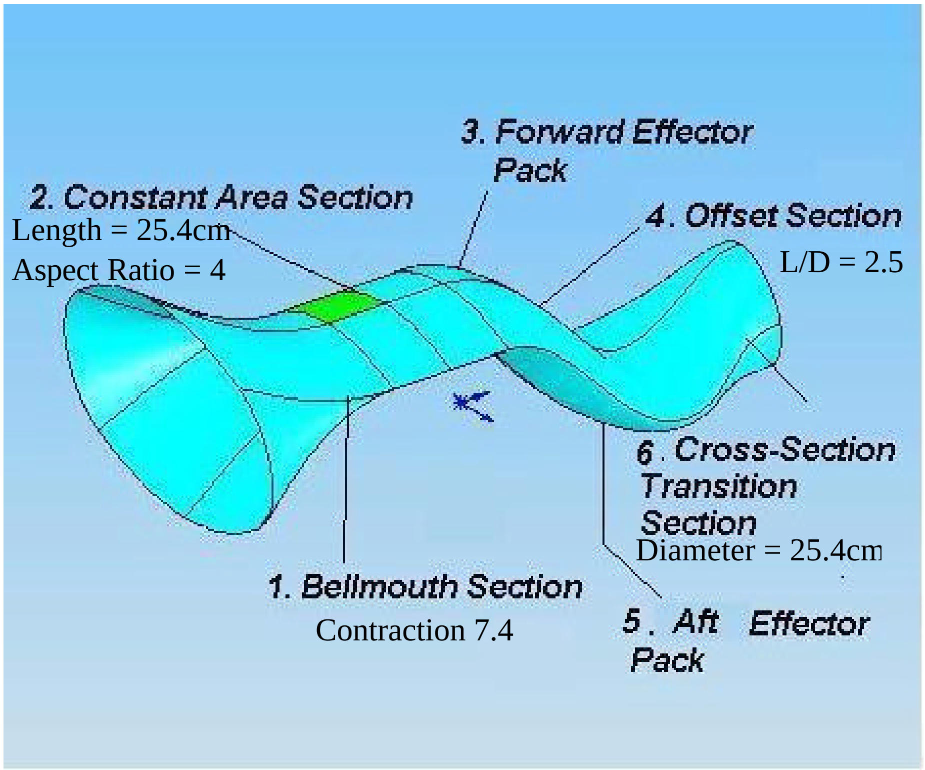

Figure 14: Serpentine duct geometry

The duct has a forward and aft effectors pack providing the serpentine geometry with two 45 degree bends. The bends are connected by an offset section between them; the second bend finally leads to the transition section leading the elliptical cross-section to transition to circular. The exit diameter is 10” and the overall duct length is 25.4” giving an overall L/D of 2.5. The inlet duct is roughly 50% scale of a practical inlet duct employed for UAVs.

Test Duct Models

As part of the background research[15] the initial baseline results were obtained on duct model donated by Lockheed Martin Aeronautics. The original duct model manufactured of resin proved fine for initial experimentations where only understanding of the baseline flow characteristics was important. However for integration of flow actuators for active flow control as part of the subsequent research endeavors, machining the resin duct was found impractical. As part of the background research at Texas A&M University, test duct sections made out of fiberglass enforced with wooden ribs and flanges were made. To produce multiple fiber glass models, molds of the duct pieces were formed out of the original resin duct and used for setup. These molds were later used to reproduce the fiberglass duct parts for varied configurations. The final duct sections made out of fiber glass with flow control actuator modules integrated are shown in Figure 15.

Figure 15: Fiberglass duct section with flow actuators

Testing Facilities

Being an internal flow problem, the engine face of the duct geometry had to be somehow interfaced with the cross-section of a suck down wind-tunnel acting as a compressor in a real case scenario. The open-loop wind tunnel used for the experimentations had an approximately 1.5’ X 1.5’ square cross-section. The setup used as part of earlier research on the serpentine duct had remained mostly unchanged through the entire length of the project. The interfacing was carried out by a 10” circular cross section to a 1.5’X1.5’ square cross-section diffuser. The main tunnel needed to be separated from the duct vibrating due to separating flows, by a rubber coupler. The coupler connected a steel pipe with a flange bolted to the duct engine face. The steel pipe incorporated a slot spanning half the upper circumference for probe access and later providing a slider mechanism for the probe rake. The 7-hole probe used for initial testing was attached to a sting holding the probe normal to the engine face. The sting was held by a traverse mechanism allowing horizontal and vertical movement. Figure 16 shows the duct model mounted to the wind tunnel along with all the other attachments.

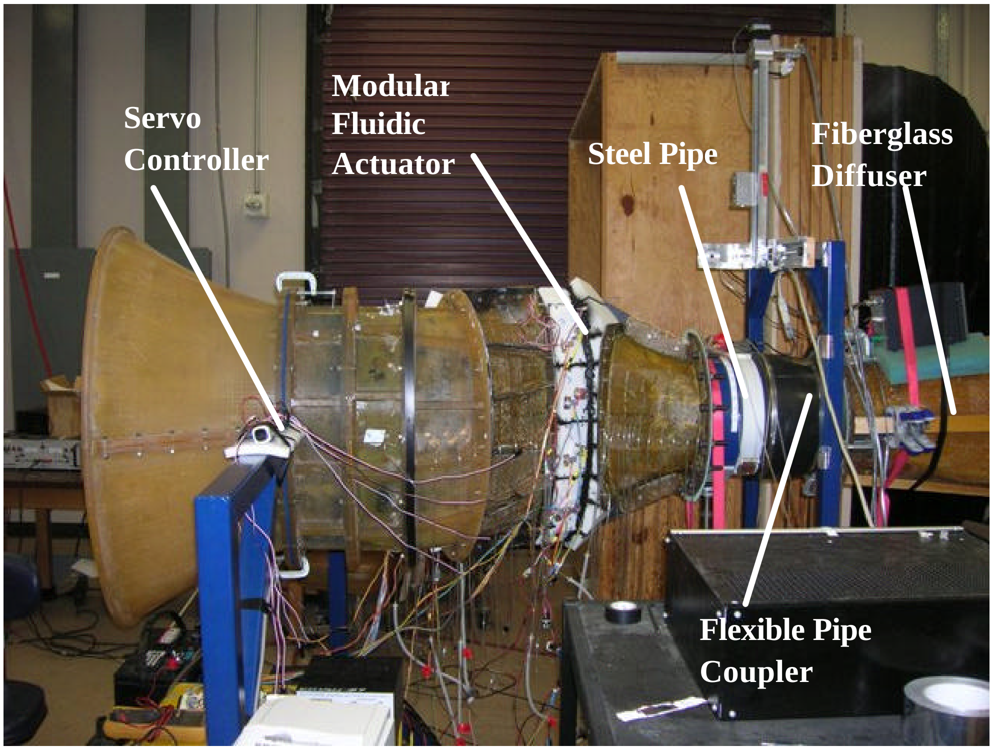

Figure 16: Experimental setup showing the duct model attached to the wind tunnel

The tunnel was powered by a centrifugal blower, 0.6096 m in diameter capable of delivering a maximum flow rate of 3.3 kg/s through the duct corresponding to a velocity of roughly 65 m/s or 0.19 local Mach through the constant area segment of the duct. The Reynolds number based on the exit diameter for the flow is 1.1 X 10^6.

Data Acquisition Devices

Electronically Scanning Pressure Sensors (ESP)

ESPs or electronically scanning pressure sensors shown in Figure 17 are an array of multiple piezoresistive pressure transducers. A standard 32 channel Pressure Systems ESP-32 HD scanner was employed. These sensors are electronically multiplexed at rates up to 20,000Hz through a single onboard instrumentation amplifier. Which means the sampling frequency per port for the ESP is limited to 625 Hz. ESPs are typically very accurate pressure measuring devices with an accuracy of ±.05% of full scale deflection (FSD).

Figure 17: Electronically scanning pressure sensors

Two ESPs were available for the research carried out at Texas A&M University. The first ESP was used for rapid scanning of pressure signals through the conventional seven hole probe scanning the engine face and locations else where. Later experimentations however stressed mainly on the engine face scanning through the use of a probe rake. Also static pressure taps were placed on each side of the duct to gather a fair idea about the static pressure distribution. Both the probe rake and static pressures were scanned by a single ESP by alternate usage.

ESPs are sensitive to minor changes in temperature and reference pressure and hence must be calibrated carefully before usage. The calibration procedure requires four inputs to the ESP, switches *C1* and *C2* which control the positioning of the calibration position valve.*C1* switches the ESP from run mode to calibration mode which basically cuts-off all the ports from atmosphere and makes them sense a common pressure from the calibrator through the *Cal* port. *Cal Ref* is the reference pressure for the calibration input pressure. The Pref port is used only during the run mode to provide a common reference to the various pressure ports.

Figure 18: ESP pin diagram

The ESP connector contains 15 pins as shown in Figure 18 with designated purposes. The pins A0 to A5 are the digital addresses; together they form the 6 digit binary address referring to the port being sent out at output pin (11). The Pins 8 and 9 form the sensor supply Vs+ and Vs- respectively. An additional 12 V supply is required on the pins 6 and 7. Finally pins 10 and 13 form the supply ground and sensor ground respectively. The ESP input/ output cable is directly connected to the Data acquisition unit.

A pressure regulating device (calibrator) was used to control the flow to the calibration port of the ESP. The calibration pressure was monitored using a barocell manometer. Five different pressure values in the range expected to be captured during experimentation were fed into the calibration port of the ESP which indeed gave out five different voltage values for each of the port corresponding to the respective pressure inputs. This data was used to finally come up with a 32 distinct curve fits for each of the 32 ports of the ESP. The whole system was controlled by Aero-acquire, data acquisition software. The signal to the various ports of the ESP, namely *C1, C2, Cal* and *Cal ref* were sent through the main data acquisition and control unit provided by Aeroprobe. The calibration curve generated is a fourth order polynomial, hence it is able to resolve high orders of non linearity. It basically requires five different known pressure inputs to correlate the respective voltages and come up with a generalized relation. The relation has a typical form presented in equation (1).

$$P_X = C_0 + C_1(V_X) + C_2(V_X)^2 + C_3(V_X)^3 + C_4(V_X)^4 \qquad (1)$$

Where:
P = Pressure to be measured
C_0 = offset (psi)
C_1 = sensitivity (psi/volt)
C_2 = non-linearity (psi/volt^2)
C_3 = non-linearity (psi/volt^3)
C_4 = non-linearity (psi/volt^4)
V = transducer voltage at P

Acquisition Hardware and Software

The analog signals from the ESP were fed into the hardware supplied by Aeroprobe. The Aeroprobe hardware, the schematic of which is shown in Figure 19 is controlled by the Aeroacquire software and acts as the main data acquisition console. The data acquisition unit is controlled by a 70psi pressure feed. This is required for the functioning of the internal valves. The console also integrates pressure signal inputs for calibration and working of the ESP including C1, C2, Cal ref, Cal signals explained earlier. The data acquisition unit is also accountable for sending multiplexing signals to the ESP and receiving back the analog signals from the piezoelectric pressure sensors. The Aeroacquire software allows specification of various control parameters relevant for data acquisition. These include the sampling rate for ESP sensors which was set to 256 Hz sampled for 10 seconds assuming an almost steady state flow for most of the experimental runs. The software also allows the use of a calibration file for the ESP which can be created using the Aeroacquire software itself as explained in the earlier sections. The program can output instantaneous pressure values for each of the 32 ports of the ESP being written into an rpf file. The rpf file can be reduced and averaged to get averaged pressure values over the sampling interval. Earlier efforts in research were concentrated towards the use of a 7 Hole probe. Aeroacquire also provides the option to use probe calibration files which can convert the 7 individual pressure signals to 3 velocity components and total and static pressure for the location being measured by the probe. The software also allows for control of stepper motors to move the traverse mechanism.

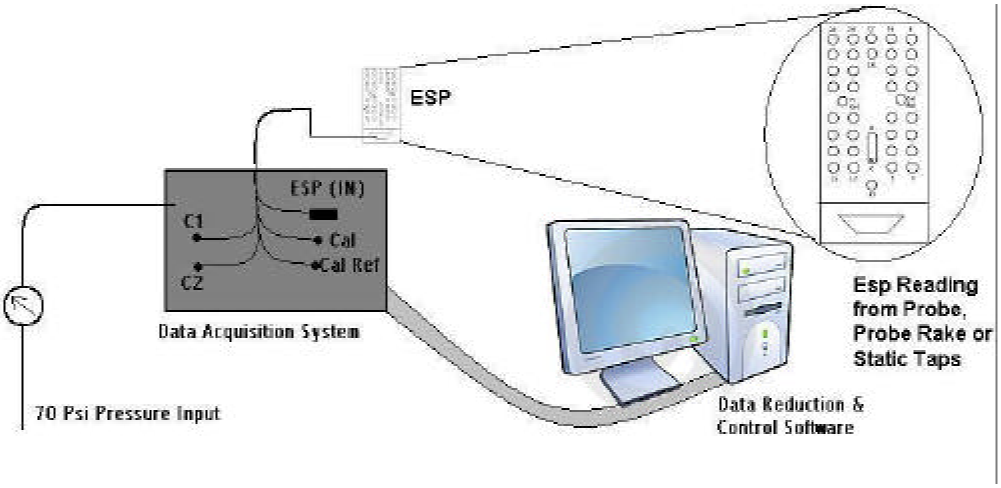

Figure 19: Data acquisition array used for experimentations

Static Taps

Static pressure taps correspond to the wall pressure which is in turn governed by the edge velocity hence giving a good idea of the state of the core flow. For the duct, static pressure taps of 1/16” diameter, 18 on the bottom surface and 25 on the top surface were placed along the length to give a fair idea of the static pressure distribution along the wall corresponding to the centerline region. Static tap plots for the current research proved particularly useful as the distribution profiles pointed at the internal flow conditions distinguishing the attached flows from separated ones.

Probe Rake

The engine face flow represents the most crucial parameter of the current research. The distortion at engine face is seen directly by the compressor blades leading to a decrease in efficiency or further detrimental effects including rotating stall. In an ideal case scenario, the total pressure should remain constant through the engine face at inlet, however due to distortion caused by secondary flow structures and viscous diffusion, the exit plane of the inlet duct corresponding to the engine face sees a highly distorted flow with massive total pressure variation. It is for this reason; a detailed total pressure plot was needed for the engine face. Earlier distributions were acquired using the probe moved by a double axis traverse mechanism, however this proved extremely time consuming and tedious for which a faster and more efficient probe rake mechanism was developed. The probe rake, which is basically a stand alone mechanism, can do a survey of half the engine face through angular traverse by sliding on the steel pipe bolted to the engine face. The rake which consists of two perpendicular arms has 16 pressure probes on each of the arms out of which 15 are standard 1/16" diameter steel tubes while one is a fast response piezoelectric sensor capable of resolving high frequency fluctuations in the total pressure. The probe rake was supported on a rim which could fit in a custom groove on the steel pipe allowing for easy sliding. The same slot which was used for probe survey was used to provide for the movement of the rake as shown in Figure 20. During experimentations, the probe rake was moved manually using an angular scale as reference, graduated at 10 degrees. Tubing attached to the steel tubes was given access through the slots on the rim. As explained earlier, the probe rake could survey only half the face, however due to assumed symmetry of flow due to duct symmetry, the data points were simply mirrored about the mid axis to get pressure plots over the entire face. The uncertainty in the movement of probe rake was limited to 1 degree.

Figure 20: Probe rake at the engine face

In order to evaluate the extent of distortion at the engine face and to monitor subsequent improvements with flow control efforts, two flow description parameters were used. The two parameters namely Cploss, averaged($Cp_{loss,avg}$) and DC_{60} were defined exactly as per the SAE ARP1420[27] guidelines. The first parameter, $Cp_{loss,avg}$ is the ratio of the averaged losses over the engine face to the dynamic pressure at the engine face. Hence higher values of $Cp_{loss,avg}$ represent a higher loss or lower pressure recovery at the engine face. The $Cp_{loss,avg}$ is defined as in equation (2).

$$C_{Ploss,avg} = \frac{P_{tot\infty} - P_{totef,avg}}{q_\infty} * 100 \tag{2}$$

In the above equation, the term P_{tot8} denotes the total pressure at the inlet. This is the reference total pressure which should be conserved throughout the flow assuming no losses. The term $P_{totef,avg}$ represents the total effective averaged pressure at the engine face gathered from the probe rake. The losses are normalized by the dynamic pressure at the engine face, q_8. The dynamic pressure is a better normalizing parameter than total pressure as the plots for different inlet velocities can be compared.

The main distortion descriptor used was DC_{60}. The parameter tries to relate the region of maximum losses to the averaged losses over the entire face. The engine face is virtually divided into numerous overlapping 60 degree wedges, the total pressure over which is averaged. The $P_{min60,avg}$ in equation (3) is the minimum of total averaged pressure of all the wedges. $P_{totef,avg}$ is as exactly defined in equation (2) while $q_{ef,avg}$ is the effective dynamic pressure at the engine which is simply the average of ideal flow dynamic pressure minus the losses. For all industrial applications, a DC_{60} of 20% or lesser is acceptable.

$$DC_{60} = \frac{P_{totef,avg} - P_{\min 60,avg}}{q_{ef,avg}} * 100 \tag{3}$$

Fluidic Actuator

As part of background efforts to integrate fluidic actuators and attempt flow control on the duct, a novel fluidic actuator design was developed[15]. The actuators integrated distinct blowing and suction modules contrary to true SJAs (synthetic jet actuators) which use a common orifice for an alternating suction and blowing flow and have a zero net mass flux. The actuator also integrated a rotary slot to provide for pulsed blowing. Typical SJA's are powered by rotary, reciprocating mechanism or even oscillating membranes as suggested by Gilarranz et al.[28]. However for the current research, the geometry posed challenges due to its extreme complexity, for which a far more simplified actuator setup was suggested integrating separate suction and blowing modules.

Various efforts were concentrated on ascertaining the locations of the fluidic actuators, experimental analysis included use of static taps for the wall static pressure profile of the baseline and surface flow visualization tests. These aided in determining the near accurate separation and vortex liftoff locations for the baseline flow. Further aid was derived from computational results which could provide clear oil flow traces and other details which could not be attained through conventional experimental techniques. The suction slots were placed just above the separation location, which as evaluated by earlier studies is the most suited location for boundary layer removal to aid in delay of separation. As discussed earlier, suction by itself was not expected to aid in secondary flow control, for which the placement and positioning of the blowing module remained a crucial issue. The entire actuator assembly had to conform to the internal duct profile for which, the complexities in geometry and space constraints dictated the development of the blowing module. The blowing module was placed approximately 1" downstream of the end of the suction module in a setup similar to the one described by Harper et al.[29]. The schematic of the cross section of the fluidic actuator is shown in the Figure 21. Four such actuators were placed side by side each connected and conforming to internal duct profile. The intake region of the suction plenum was covered by a perforated plate enhancing boundary layer removal. As shown in the schematic, the flow enters the suction plenum pulled by the centrifugal fan, the centrifugal action further accelerates the flow into the blowing plenum, where after the flow re-nters the duct energizing the core flow. Figure 22 shows the placement of the fluidic actuators relative to the duct geometry.

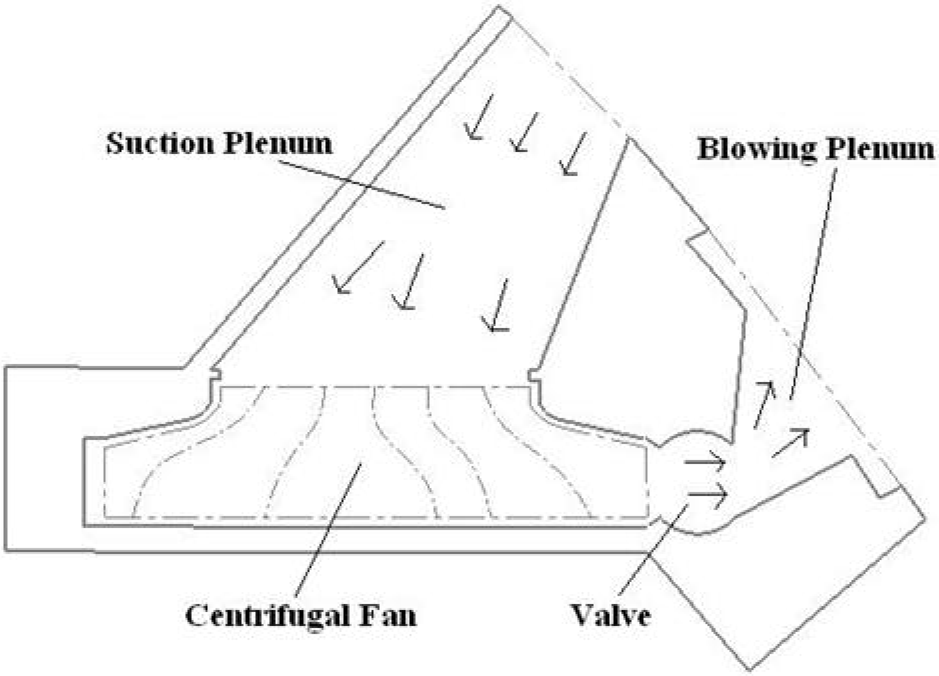

Figure 21: Schematic of fluidic actuator

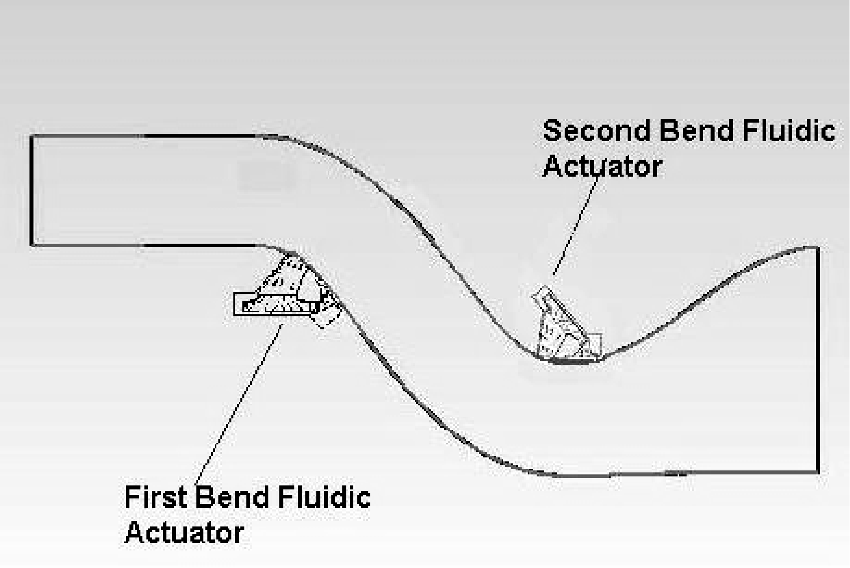

Figure 22: Placement of fluidic actuators

These modular fluidic actuators were designed on Solidworks 3D modeling software and manufactured using a rapid prototyping technology available at Texas A&M University using molten ABS plastic for layer by layer deposition. The blowing slots were integrated into replaceable plates manufactured separately. This was done to exercise flexibility in changing slot configurations without the need of remanufacturing the entire blowing plenum. Figure 23 shows the first bend blowing module with 5 slot stream-wise plates installed. The modular actuator spanning the entire width of the bend was made constructed out of 4 isolated chambers. This was done to simplify the design over the complex elliptic cross-section and also to exercise flexibility for possible individual control of the actuator sections at different locations. Figure 23 also shows the more complex second bend blowing module with connected individual compartments.

The absence of plate configurations expose the blowing plenum showing the embedded slots allowing the air to enter from the suction plenum. Rotary slots were installed for previous pulsed blowing attempts. Figure 24 shows the entire first bend SJA module connected to the throat section. The perforated suction strip over the suction module can be seen immediately upstream of the jet slots. The picture also shows the connected motors responsible for driving the centrifugal fans.

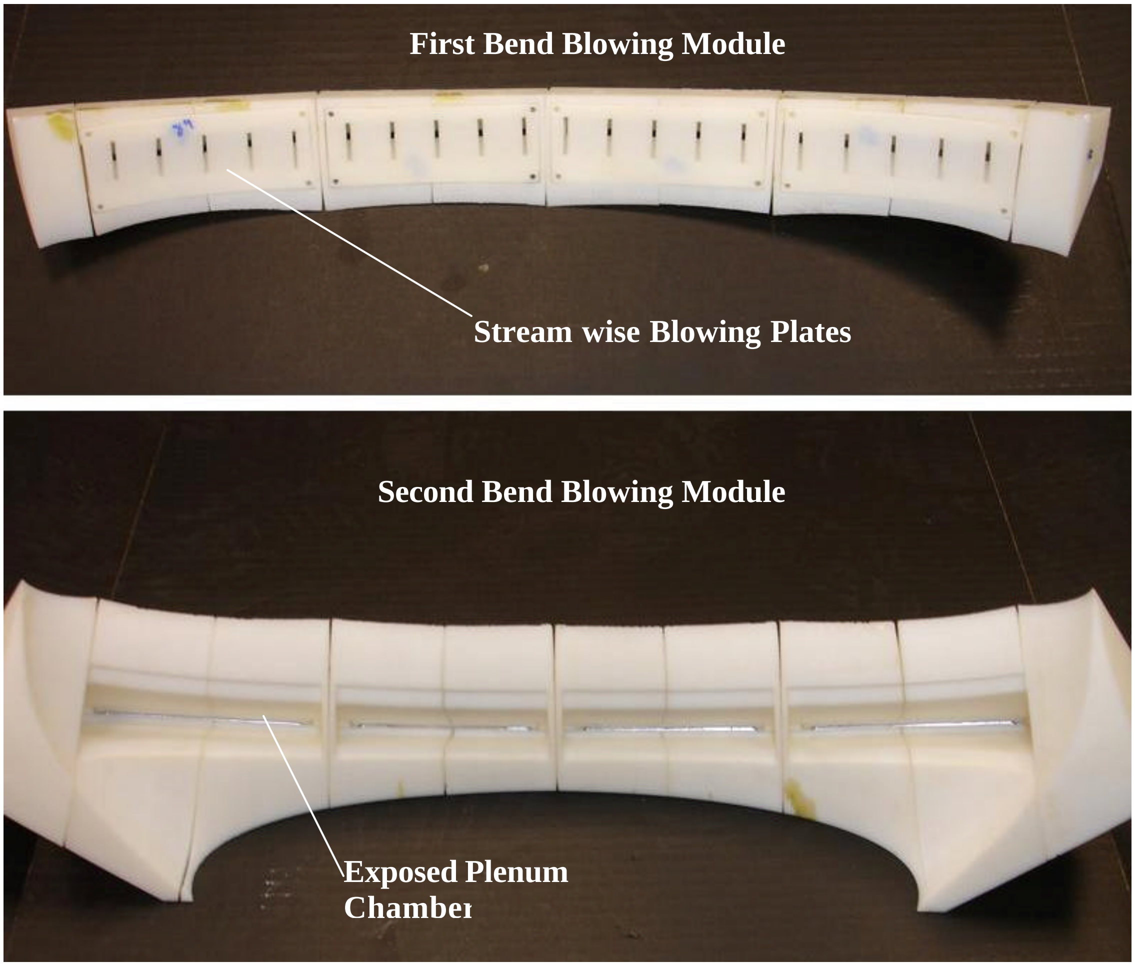

Figure 23: Blowing modules for first and second bend

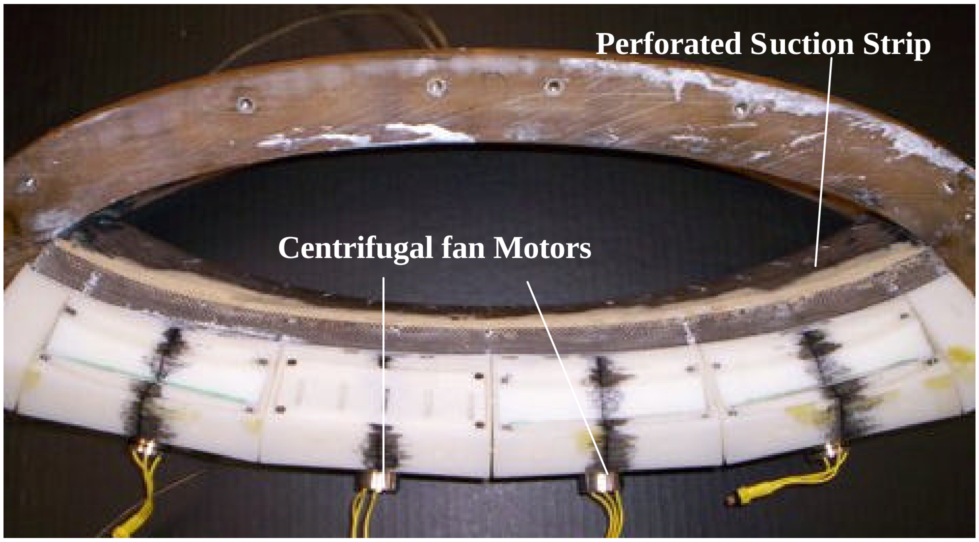

Figure 24: Complete 1st bend actuator module

Uncertainty Analysis

A sound uncertainty analysis was performed to quantify the various uncertainties present in the experimental readings presented in this thesis. Uncertainty in an experiment can be attributed to the various errors present during the measurement of a certain value. Sources of uncertainty can be largely divided into two groups. One due to random fluctuations in the readings observed with steady conditions over time. This uncertainty which is mainly termed the precision limit is the lack of repeatability. The second type is the bias uncertainty and is due to the fixed error incurred during experimentations. The bias uncertainty mainly arises from instrument errors.

For the experiments conducted the precision limit was calculated by taking data sample set over a span of 10 seconds at a frequency of 1024 Hz for the ESP. The standard deviation was calculated about the mean reading. An absolute uncertainty was assumed to be double of the standard deviation for a confidence level of 95%. The bias uncertainty was assumed as the specified uncertainty of the instrument manufacturer for a confidence level of 95%. This was obtained individually for the manometer and the ESP. Viskanta et al.[30] combined the two uncertainties with a relation given in equation (4).

$$U_Y = \sqrt{P_y^2 + {B_y}^2} \qquad (4)$$

In the above relation, U_y represents the uncertainty of the variable Y, P_y is the precision uncertainty in Y while B_y is the bias uncertainty in the Y. In general the uncertainty ($w(Y)$) in a dependent variable Y was best defined in a relation given by Kline and McClintock[31] given in equation (5).

$$w(Y) = \sqrt{\sum_{i=1}^{n} \left(\frac{\partial Y}{\partial x_i} w(x_i) \right)^2} \qquad (5)$$

In the above equation n is the number of x_i independent variables contributing to the uncertainty in Y while $w(x_i)$ represents the individual uncertainties of variables x_i.

The averaged random uncertainties calculated from the individual standard deviations observed during experiments were 0.04155 torr for static taps and 0.06846 torr for probe rake. The instrument uncertainty as specified by the ESP manufacturer is 0.05% of full scale. Full scale for the particular sensor is 20” of water and hence the ESP uncertainty was found out to be 0.1868 torr. The total averaged uncertainty in static taps was calculated to be 0.046 torr and 0.071 torr. Additionally the instrument uncertainty of the manometer as provided by the manufacturer is 0.00748 torr and 0.05% of the reading for barocell manometer used in the calibration of ESP.

CFD RESULTS AND DISCUSSIONS

The aim of this study was to develop a good understanding of the physics governing the flow through the inlet duct and later study the effects of flow control through fluidic actuation and was done through conjunction of CFD and experimental analysis. Many prior studies have been conducted in the similar fashion including a study of flow through curved ducts conducted by Towne[2]. Towne made certain assumptions valid for low speed viscous flows through curved ducts and reduced them to a simpler form. He then solved the flow through the duct using an explicit formulation on a coordinate system following the duct curvature. Through careful formulation he could attain a good agreement between computational and experimental results. This section discusses CFD results of the baseline flow reaching important deductions followed by flow control results. The CFD problem setup explained in an earlier section was adopted for all simulations with minor variations if required. Most of the processing was carried out in batch mode on the two supercomputers at Texas A&M University. Of the available machines either SGI Altix 3700 or an IBM Regatta p690 were used for simulations. The SGI Altix comprises of 32 pairs of 1.3 GHZ Itanium-2 64-bit µ - processors whereas IBM Regatta p690 has 32 1.3 GHZ processors. Most simulations were carried out on a requested memory of 3GB and 4 processors.

The boundary conditions used for simulations were fairly standard and known from experimental settings and testing conditions. The velocity normal to the inlet plain was specified at 60 m/s. The turbulence in the inlet flow is specified as turbulence intensity and turbulent viscosity ratio, turbulence intensity is the percentage ratio of the root mean square of fluctuations to the average velocity. For low disturbance and controlled cases a value of less than 1% is achievable, a value of 0.5% was assumed for the experimental runs. Turbulent viscosity ratio is the ratio of turbulent viscosity to molecular viscosity and is proportional to Reynolds number, for the inlet duct flow, a value of 10 was preferred. The outflow condition simply takes mass weight age as input which equals 1.0 for the baseline case ignoring compressibility effects. The convergence in most cases was achieved within 1500-2000 iterations run for about 10-12 hours. Initial iterations were carried out in the interactive mode to monitor stability and manipulate under-relaxation parameters if necessary.

Baseline Results

Baseline results presented here show the most important characteristics of the inlet duct flow. The results obtained in the baseline cases compare well to the ones obtained by Mohler for his simulations on the M2129 S-Duct[26]. The bends cause high static pressure gradients to appear between the near wall and core regions of the duct as visible in Figure 25 showing static pressure contours at the symmetry plane. The region after the second bend shows chaotic pressure recovery contours as a result of flow separation.

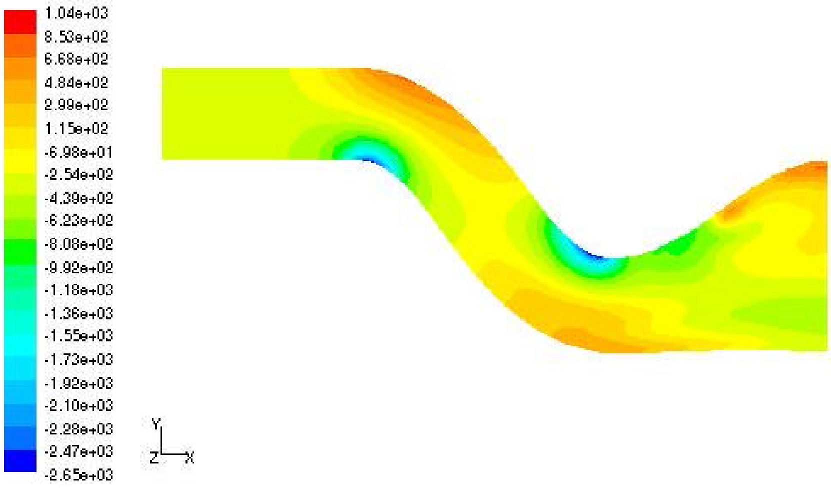

Figure 25: Static pressure contours for symmetry plane

The total pressure which refers to the total energy contained in the fluid shows heavy depletion in many zones on the symmetry plane (refer Figure 26). The green zones close to the wall are mainly due to viscous diffusion and relate to the boundary layer growth. Further downstream the core flow sees heavy losses due to separation and secondary flow formation showing a total pressure recovery as low as 60%. Separation and vortex formation result in heavy turbulent mixing, eddy formation and flow retardation. Recovery of total pressure is the main aim of the current study which is why it is important to identify sources of losses.

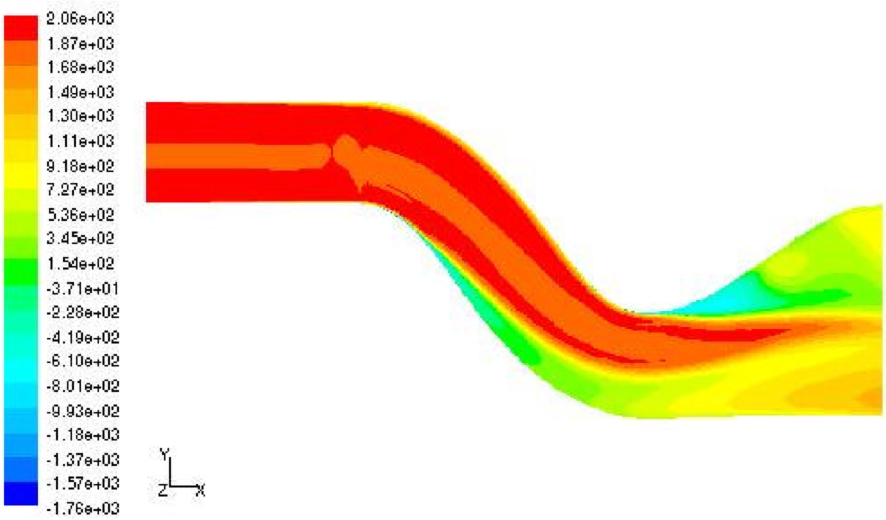

Figure 26: Total pressure contours for symmetry plane

The simulations show strong evidence of flow separation and boundary layer migration. The velocity vectors on the symmetry plane show slowing down velocities at the near wall region of the duct especially near the centre of the duct where the migration effects are substantial. The reversed vector regions can be clearly seen diffusing into the mainstream flow at the first and the second bend shown as blue regions in Figure 27.

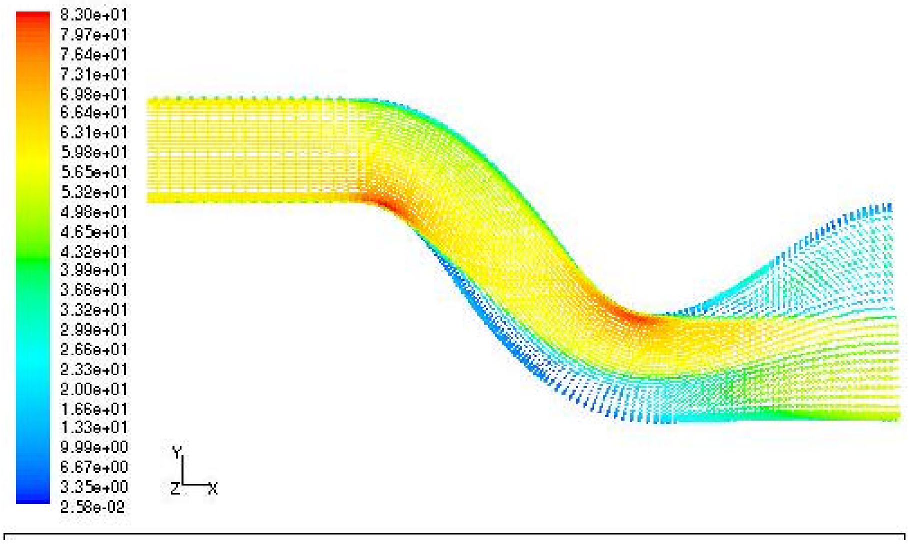

Figure 27: Velocity vectors at symmetry plane

The high pressure in the mean flow is dictated by the edge velocity which increases at steep bend followed by steep deceleration or recovery. This in turn results in a steep rise in pressure immediately after the bend causing the low energy fluid very close to the wall to stagnate and reverse direction, the reversed flow vectors then diffuse back into the high speed main stream fluid giving the classic separation pattern as visible in Figure 28. Separation in general decreases efficiency as it is a source of energy losses which is finally visible in decreased stagnation pressure as a result of low momentum fluid. It can also be seen that separation bubble generally ends with reattachment of the boundary layer.

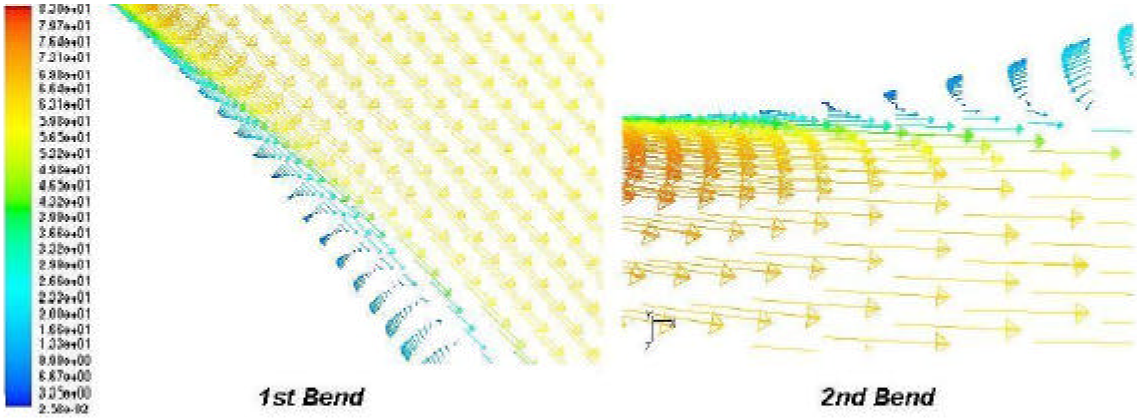

Figure 28: Separation at the bends (symmetry plane)

The most significant feature of the curved duct flows is boundary layer migration observed in many previous studies[2, 4, 5, 8, 15]. The core flow while trying to negotiate a steep bend experiences a centrifugal force which in turn translates as a pressure differential between the inside and outside of the duct attracting fluid elsewhere to the center of the duct. The slow moving boundary layer with a small centrifugal force reacts quickly to the pressure gradient and migrates to the center along the walls. The accumulation eventually pushes out existing fluid into mainstream giving the characteristic liftoff effect. Anabtawi et al.[4] stated that in a two bend system it could be thought that the secondary flows due to second bend may cancel out the effects of those due to first bend. However, the secondary flows due to both the bends remained and propagated well into the engine face with no evidence of cancellation effect. This is an important insight in the understanding of secondary flows in S shaped ducts theorizing the irreversible nature of boundary layer migration and that the boundary layer continues to migrate even after the first bend. The CFD simulations for the problem in question gave similar results showing clear evidence of boundary layer migration. Figure 29 shows the migration pattern of pathlines near the wall at first bend using oil traces which are analogous to surface flow visualization techniques in experimentation.

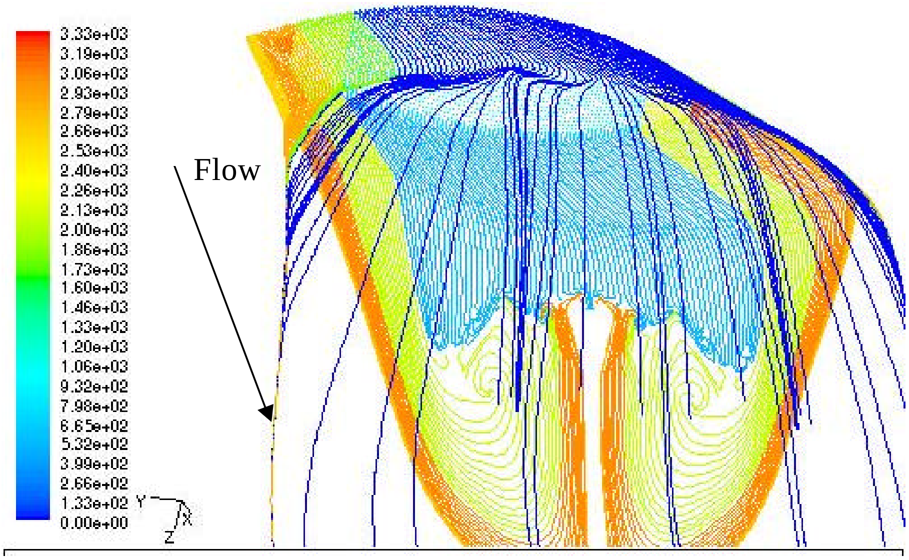

Figure 29: Boundary layer migration at first bend

The path-lines on the bottom experience maximum influence from the second bend. The light blue streamlines on the surface show separation due to bend gradient. The yellow and orange streamlines can be seen migrating from the outside of the cross-section to the inside. The onset of counter-rotating vortices can also be seen in the circulation patterns immediately after the bends. The gap at the centre of the wall depicts the liftoff of the path lines due to fluid accumulation at the centre finally resulting in strong secondary flows. The second bend has a much steeper bend with a sharp variation in cross-section transitioning from elliptical to circular cross section. The high gradients produce a much higher centrifugal force and a stronger separation. The migration of boundary layer was visibly more aggressive for the second bend giving out secondary flows with much higher distortion effects. Figure 30 shows the migration as caught by oil flow traces at the second bend. Interestingly the irreversibility of migration is verified by the continuing center gap at the bottom surface, an after effect of first bend migration.

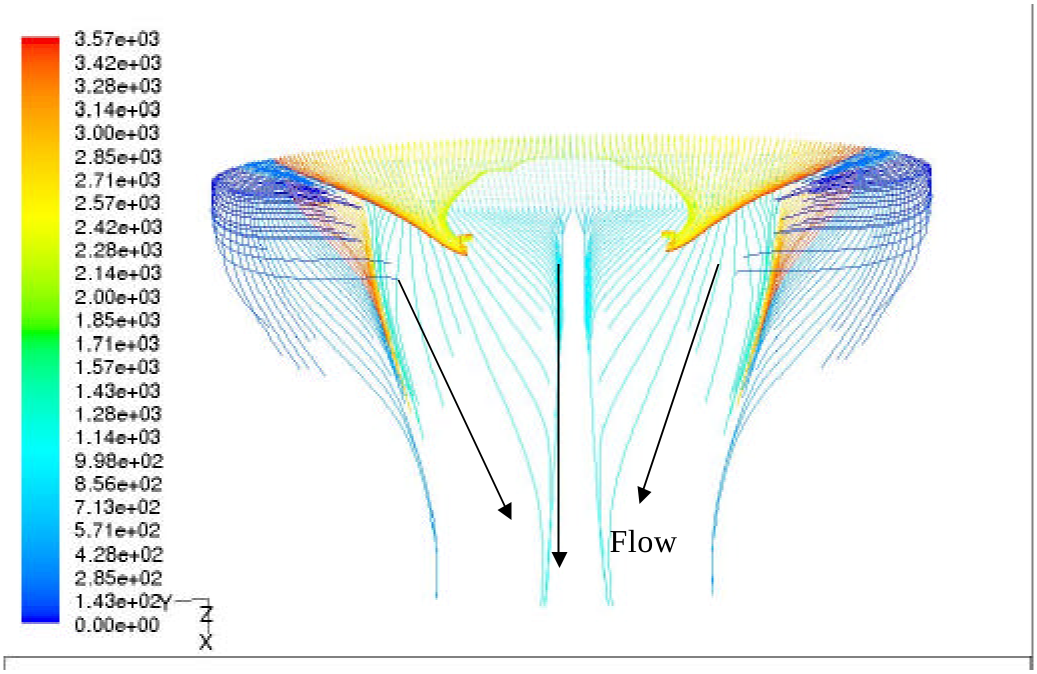

Figure 30: Boundary layer migration at second bend

The migration patterns finally results in the counter rotating vortex pairs at the engine face. As discussed earlier in this text, the vortex pair due to second bend is stronger as it has traveled a shorter length hence undergoing lesser diffusion in addition to the steeper second bend for the problem in question clearly visible in the engine face vector plot shown in Figure 31. The vectors at the lower regions of the engine face show signs of weaker or suppressed vortices due to higher diffusion into the core flow. This is the characteristic pattern of flow distortion for the inlet S-duct flows. The effectiveness of flow control is monitored by the suppression of distortion.

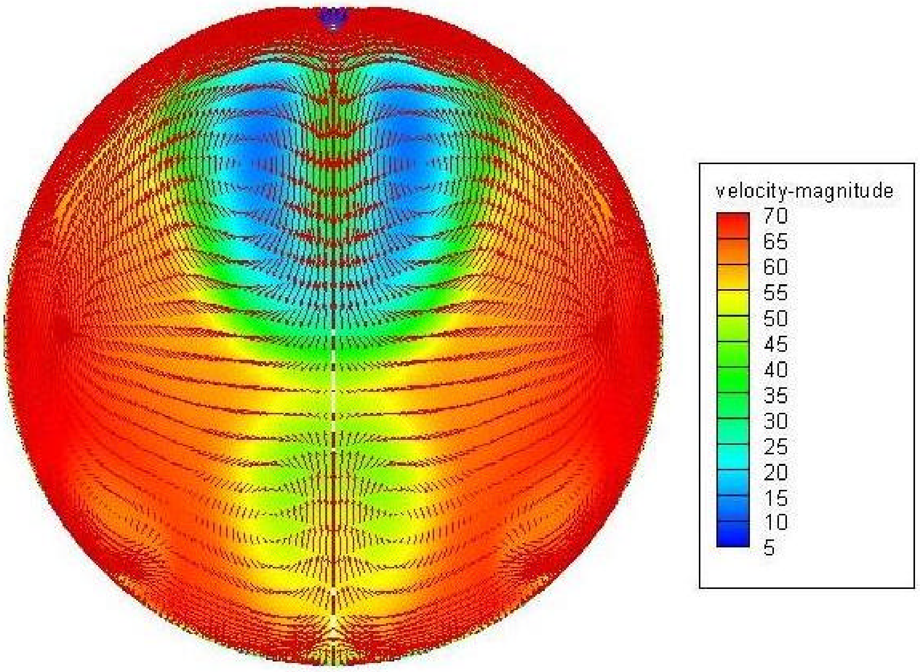

Figure 31: Vector plot at the engine face

First Bend Flow Control Results

Flow control in the S shaped duct was attempted using fluidic actuators through suction or blowing. For initial investigations only suction was integrated immediately downstream of the first bend. This was done to study the effectiveness of suction for separation suppression or delay which may result in higher pressure recovery at the engine face. However, no substantial effect on secondary flows was expected as secondary flows relate to generation of vorticity structures which must be countered by use of vorticity signature by active flow control devices. The low energy fluid in the boundary layer is highly susceptible to adverse pressure gradients leading to separation. Suction tries to energize the boundary layer by pulling the main stream flow into the boundary layer reenergizing it. Almost complete pressure recovery can be achieved through pure suction for curved ducts with square or rectangular cross section as demonstrated by Kumar and Alvi[10] for the Stratford ramp using microjets for flow control.

Suction for the inlet duct problem was achieved by modeling a suction slot as an outflow boundary condition on the bottom duct wall immediately after the first bend. The slot had a width of 1" and a span covering the entire bottom span of the duct cross-section. The suction was allowed to consume 1% of the total mass flow rate entering the duct through the velocity inlet. The initial studies were aimed at purely studying the effect of flow control at the first bend. To save on computational time and expense, the duct portion following the offset section was removed. This was based on the assumption that the disturbances at the second bend were not expected to influence flow characteristics at locations following the first bend. Baseline simulations were conducted on the modified duct geometry (second bend and cross-section transition portion removed) to have baseline comparison for flow control simulations. Figure 32 and Figure 33 show baseline velocity vectors at symmetry plane and at the outflow plane respectively. The symmetry plane clearly shows strong reversed flow vectors depicting the extent of separation. The outflow plane velocity vectors show strong secondary flows. The vortex pair shed due to migration of the boundary layer at the first bend is visible on the bottom of the outflow vector. The slow moving vortex cores, characteristic to viscous vortices contributes to maximum total pressure losses across the duct cross section. Two weaker vortex cores can also be seen close to each edge of the elliptical cross section. The exact physics for the formation of these vortices is still unclear but they exhibit opposite vorticity to the core vortices in the centre of the duct hinting at the tertiary nature of these vortices.

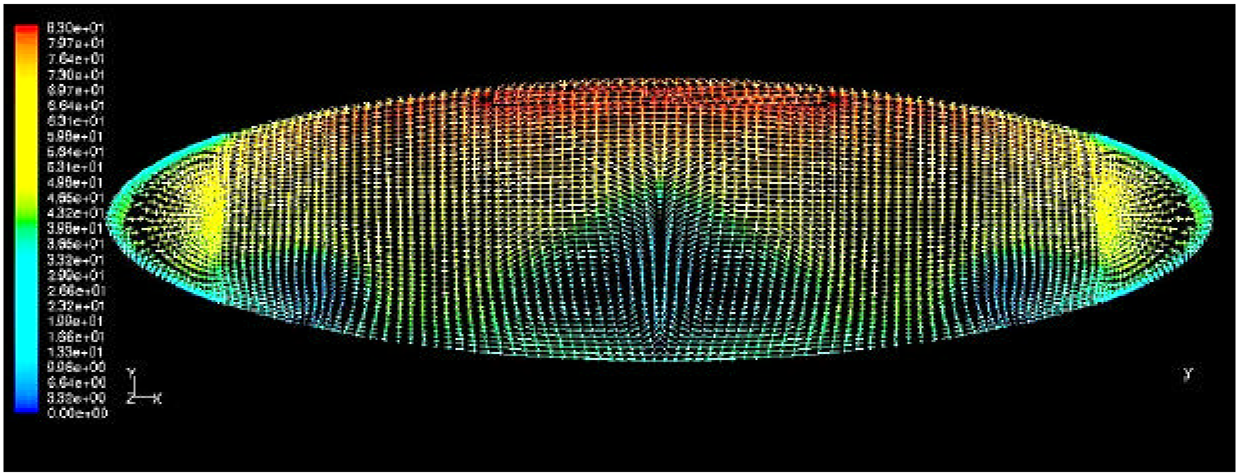

Figure 32: Outflow face velocity vectors

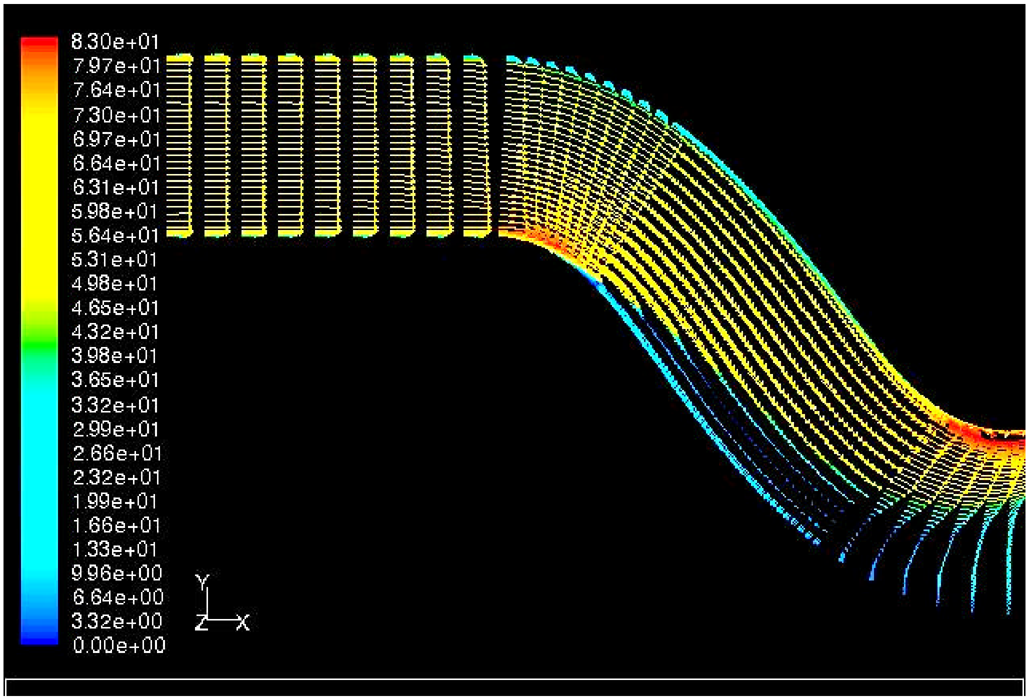

Figure 33: Symmetry face velocity vectors

The suction case showed significant improvement over the baseline results. The suction definitely proved effective in reenergizing the near separating boundary layer immediately after the first bend. The separation was delayed significantly. The separation origin or the saddle point shifted from 12.5” in the axial direction to17”. Oil traces shown in Figure 34, following the first bend show a fair amount of improvement over baseline oil traces (Figure 29). The flow separation pattern clearly appears to have moved down, the boundary layer migration looks much weaker than in no control case but it still exists as seen by converging flowlines, the gap in the centre of the duct is still representative of the massive liftoff zones showing flow lifting off the lower wall.

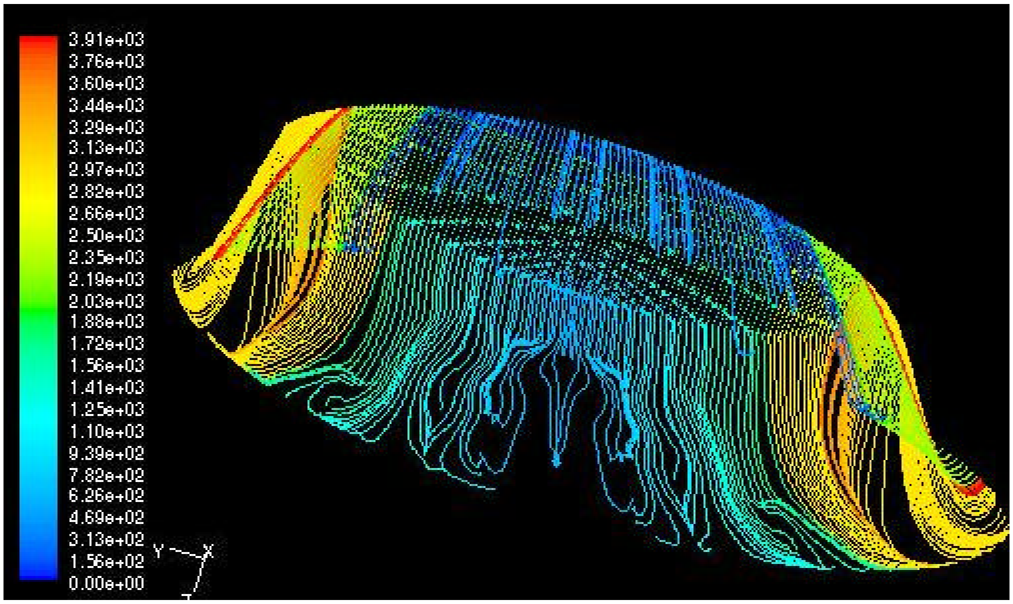

Figure 34: Oil traces on offset section immediately after first bend

The vector sketches reaffirm the partial success of suction at first bend. Figure 35 shows the velocity vectors at the symmetry plane. Clearly a far better behaved flow compared to the no control case is visible. The reversed flow vectors conclusive of flow separation have shifted to a far more down stream location with reduced intensity. This also indicates an increased pressure recovery. Figure 36 shows some interesting features. Instead of showing a single pair of secondary flow vortices, the suction case shows multiple vortices at the outflow. As discussed earlier, suction by itself would not be much effective in suppressing secondary flows; however, the current study shows it can definitely decrease the intensity giving higher total pressure, if not a reduced distortion itself. The multiple vortices seen at the outflow have opposite vorticity with respect to their immediate neighbors. Suction definitely gave encouraging results for the case in hand.

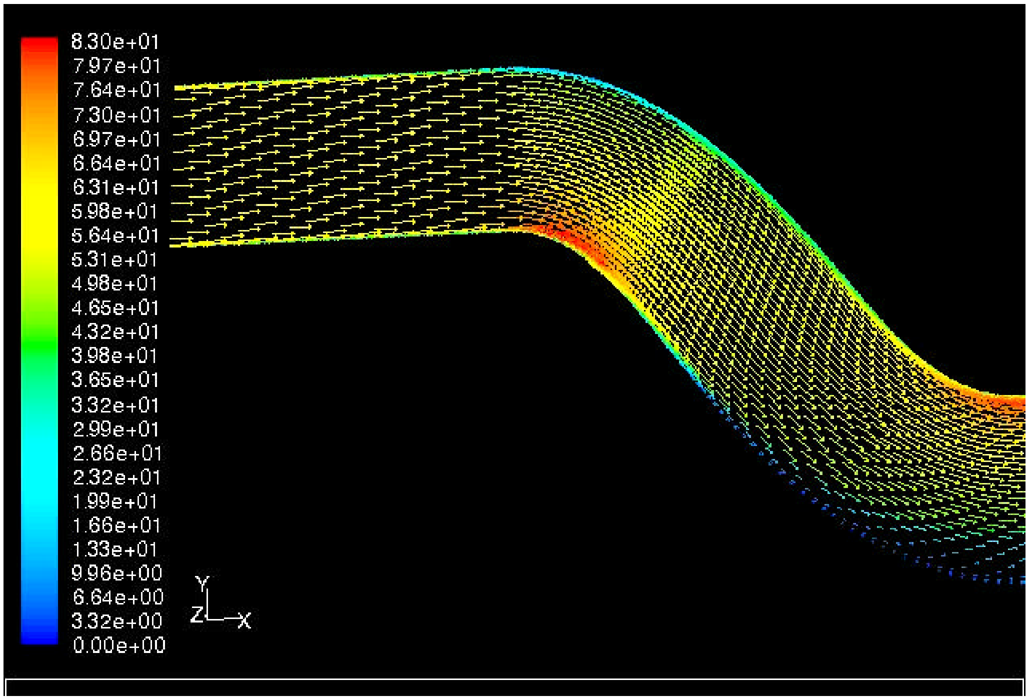

Figure 35: Velocity vectors at the symmetry plane

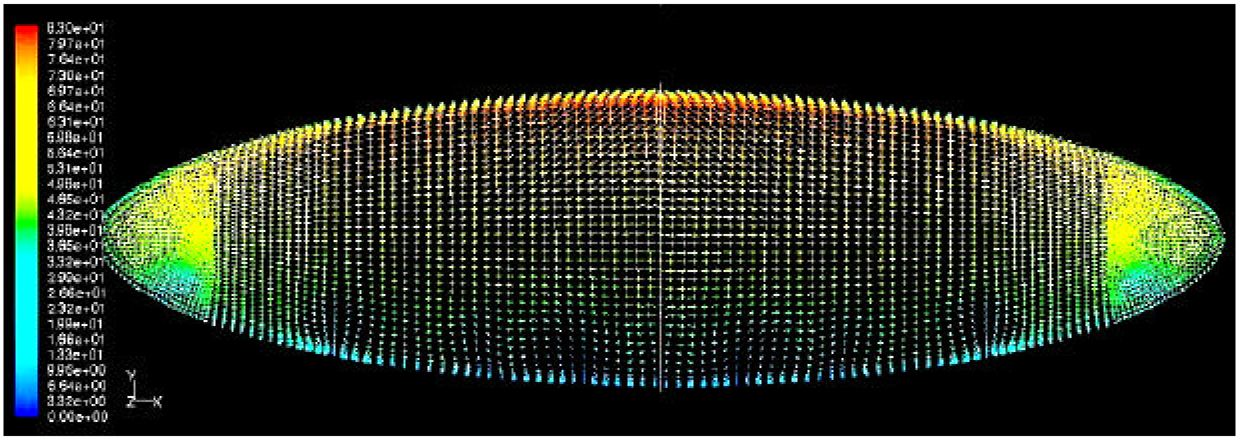

Figure 36: Velocity vectors at the exit plane for the suction only case

Flow distortion remains the main focus of the study. Even though suction by itself was promising for the first bend, it still gave considerable flow distortion at outflow. The first bend distortion contributes to a small percentage at the engine face after going diffusion over the length of the duct. The investigation on first bend also gave significant guidelines for the extent and type of flow control which would be required for the steeper and closer to engine face, second bend. Various studies have used micro jets for injecting high momentum fluid in the core flow but jet injection slots were used for the current study because of their various advantages over authentic micro jets as already cited.

Twelve stream-wise slots were used for blowing. All slots were 2mm wide and 1” in length along the stream-wise direction. The equally spaced slots were all placed parallel to each other 1” downstream to the end of suction slot on the bottom surface of the offset section as visible in Figure 37 showing the underside of the duct.

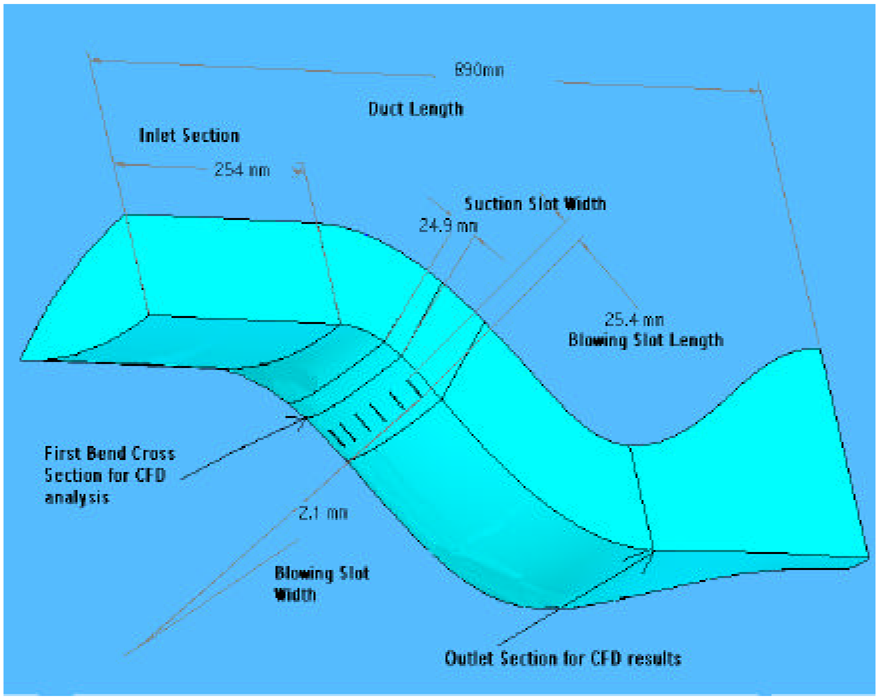

Figure 37: Suction and blowing dimension at the first bend

The actual actuator used for experimental analysis, consists of a connected suction and blowing plenum hence it was necessary to maintain mass conservation for computational studies as well. The blowing was thus done at 1% of the total mass inlet.

Suction and blowing together proved to be very effective for achieving flow control at the first bend. The actuator jets blew at approximately 40 m/s as shown in Figure 38. The high momentum jets could reach into the core flow and redistribute the vorticity and enabling pressure equalization, achieving almost complete pressure recovery.

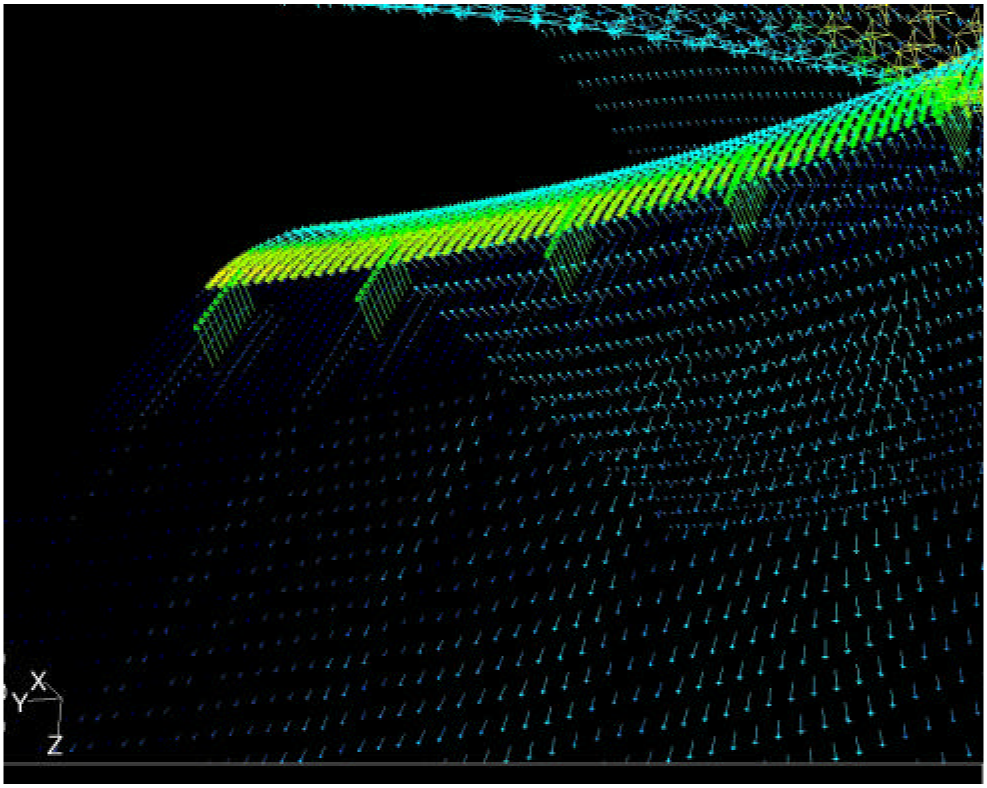

Figure 38: Jets blowing through actuator slots

The oil traces for the suction and blowing in Figure 39 show elimination of flow separation marked by absence of disintegrating flow-paths, which was expected as the jets can energize low energy fluid by turbulent mixing along with inducing vorticity in the core flow. Elimination of separation marks a noteworthy accomplishment for this study as it aids substantially towards total pressure recovery. The path-lines at the wall remain largely streamlined with minimal convergent behavior and negligible vorticity evident of almost complete elimination of secondary flows which can be attributed to the effectiveness of vorticity introduction in the core flow through two blowing slots. Further details towards effects of flow control through fluidic actuators can be obtained through the vector plots.

The velocity vectors reveal the true flow characteristics following steady blowing and suction. The symmetry plane velocity vectors (Figure 40) don’t show any sign of flow reversal and strong evidence towards complete elimination of separation is seen in the oil traces. The vectors also show a higher dynamic pressure close to the wall, indicating a higher over all pressure recovery at the exit plane, finally translating to the engine face.

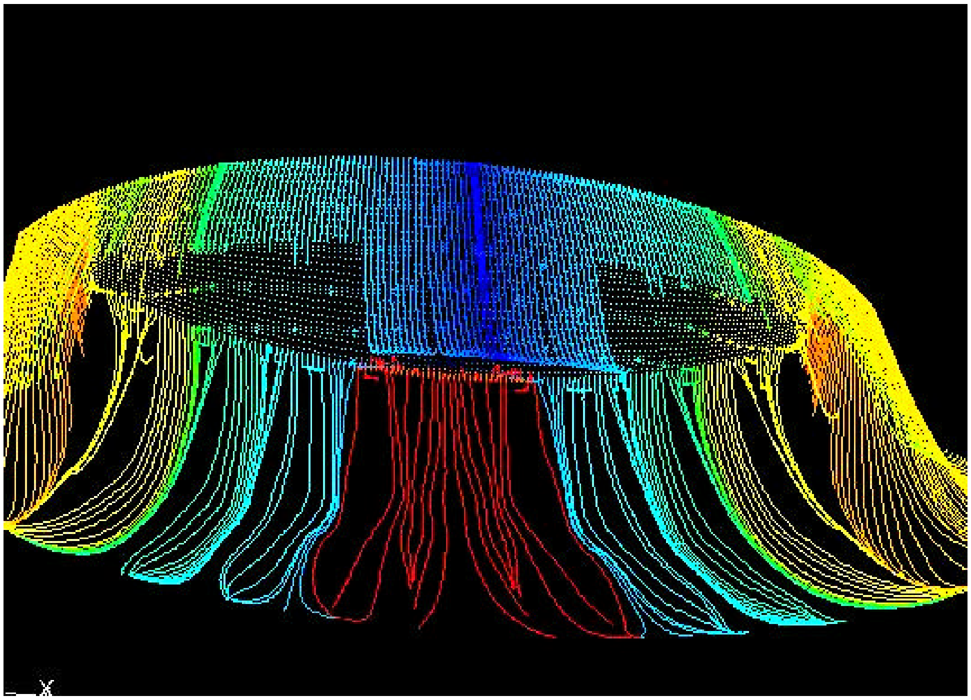

Figure 39: Oil traces on the offset section following first bend

The outflow vectors show interesting flow characteristics at the exit plane. The high momentum jets blowing into the flow induce counter-rotating vortices along the slot length giving mushroom-like structures visible at the exit plane. These counter rotating vortices are sensitive to slot orientation as explained by Bridges and Smith[14] in their study on effects of slot orientation. However, for the case in discussion, stream-wise slots were used (perpendicular to the flow front) which give vortices of equal strength. So even though the net vorticity introduced is zero, the vortex pairs enhance mixing of layers with varying dynamic pressures enabling a more homogenized flow field delaying or eliminating separation and to some extent the formation of secondary flow vortices. The exit plane shown in Figure 41 show interestingly twelve mushroom like structures, each representative of a pair of counter rotating vortices of equal strength depicting the turbulent mixing of the actuator jets into the core flow. The velocity vectors at exit plane show no signs of secondary flows.

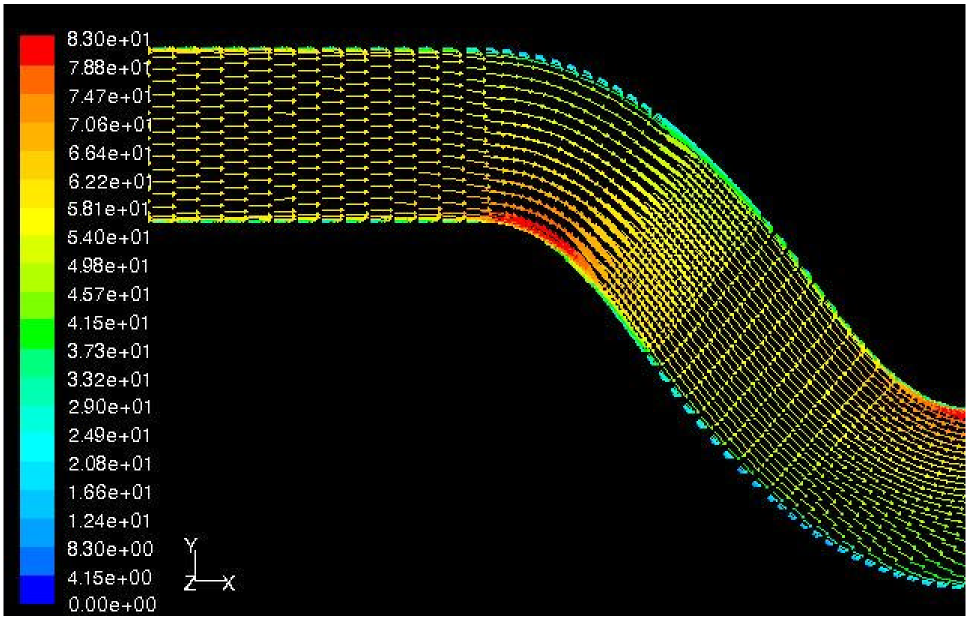

Figure 40: Velocity vectors at symmetry plane for suction blowing plane

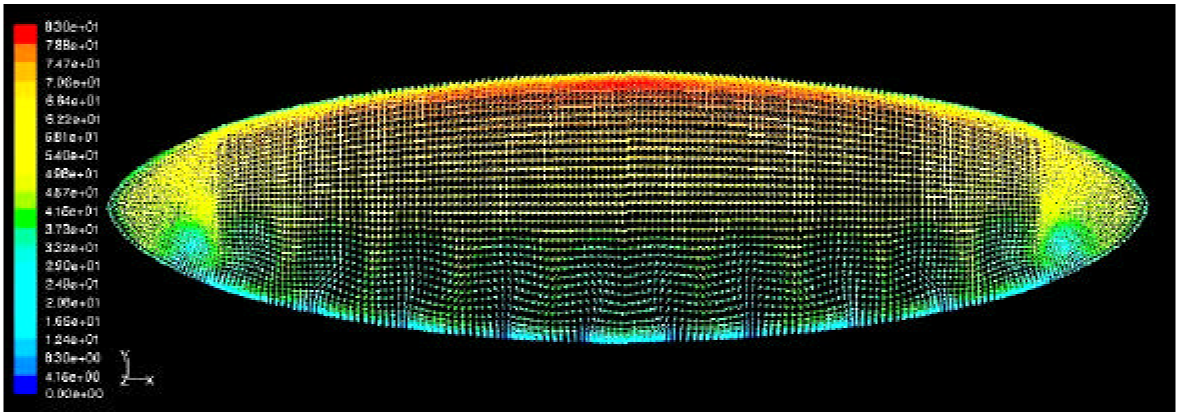

Figure 41: Velocity vectors at exit plane for suction blowing case

A final comparison of total pressure for the no control, suction and steady blowing & suction case is shown in Figure 42.

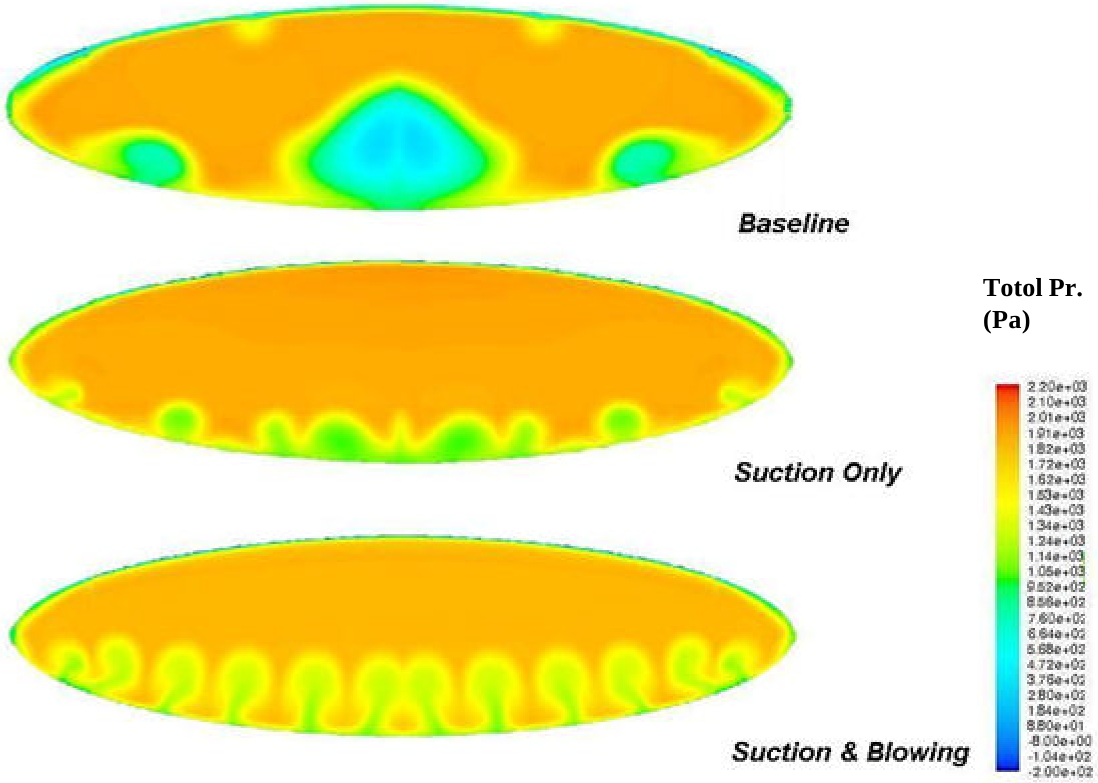

Figure 42: Total pressure contours for studies at first bend

Second Bend Flow Control Results

Flow control at the second bend was particularly of more interest due to higher contribution to flow distortion. The second bend clearly sees a much higher gradient across and also goes through a steep cross sectional variation, transitioning from elliptical to circular over a small length. The aforementioned characteristics of the second bend lead to a more violent secondary flow production and separation patterns.

Suction by itself was clearly not expected to be very helpful in pressure recovery. Strong secondary flows such as the ones produced by the second bend require strong jets enabling turbulent mixing and vorticity redistribution. This can be achieved only through the use of jets blowing high momentum flow in the mainstream flow along with suction. Similar to the treatment used for the first bend, suction and blowing was attempted at locations close to the second bend. The need for integrating flow at the complex second bend and cross-section transition required use of unstructured grid which would have other wise become an extremely complex grid generation problem in GAMBIT. Figure 43 shows the grid modification following the offset section, showing a mainly unstructured grid concentrated close to the boundary layer.

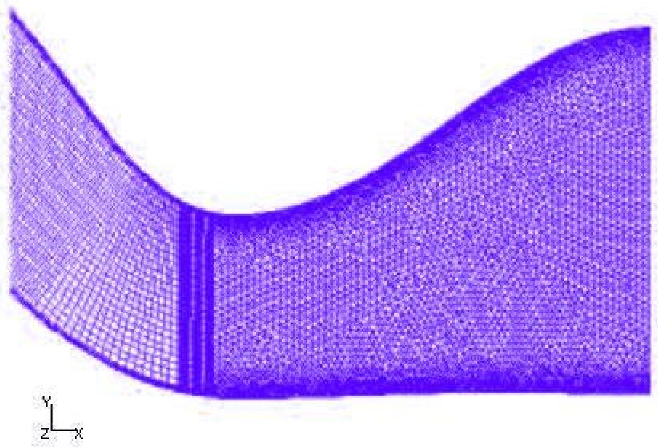

Figure 43: Hybrid grid showing use of structured grid for offset section followed by unstructured grid

The change of mesh made the computations more time consuming and computationally heavy, firstly due to increased grid points and secondly due to the inherent nature of unstructured grids to consume more resources. There were noticeable differences for the baseline flow compared to the earlier simulations; this included secondary flow vortices at the engine face due to the second bend being slightly smaller and weaker. The flow distortion however appeared more or less to the same extent making its severity almost comparable to the original baseline case. Figure 44 and Figure 45 show the symmetry plane and engine face vectors respectively for reference.

Over the entire length of the inlet duct, the distortion effects due to the first bend diffuse into the flow hence decreasing their contribution to engine plane distortion. Clearly as pointed earlier in this text, the second bend due to its severity in geometry and proximity to the engine face accounts for maximum pressure loss and distortion. The separation and migration patterns are similar to those seen for the first bend but vary in intensity. This clearly points at the possibility of having the need to use more effective flow control than that used for the first bend.

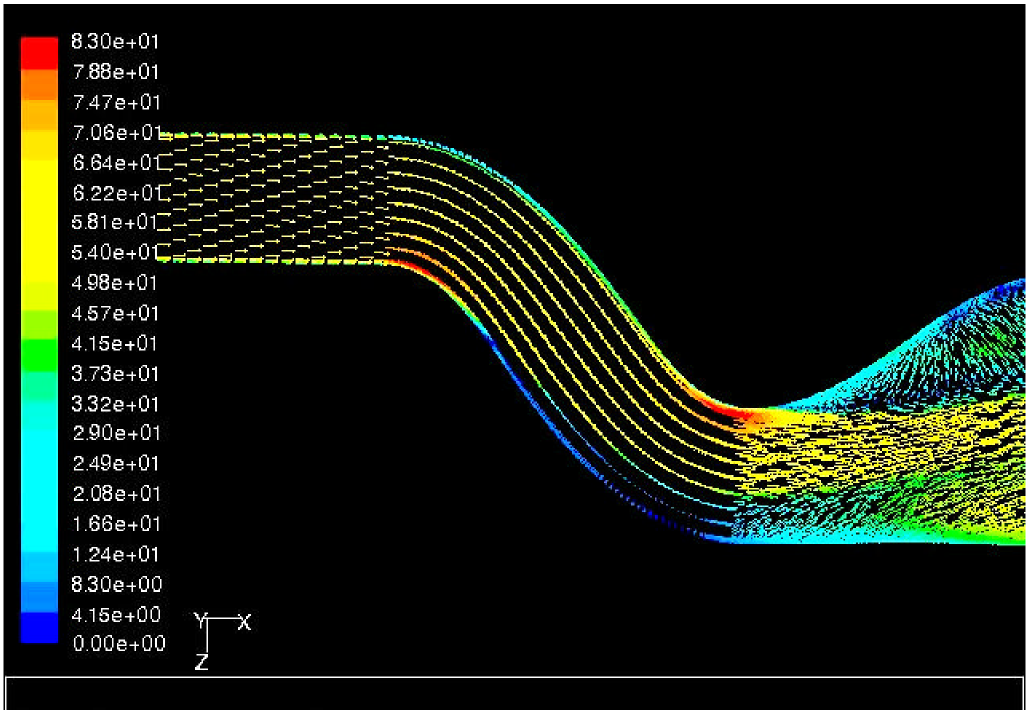

Figure 44: Velocity vectors at symmetry plane

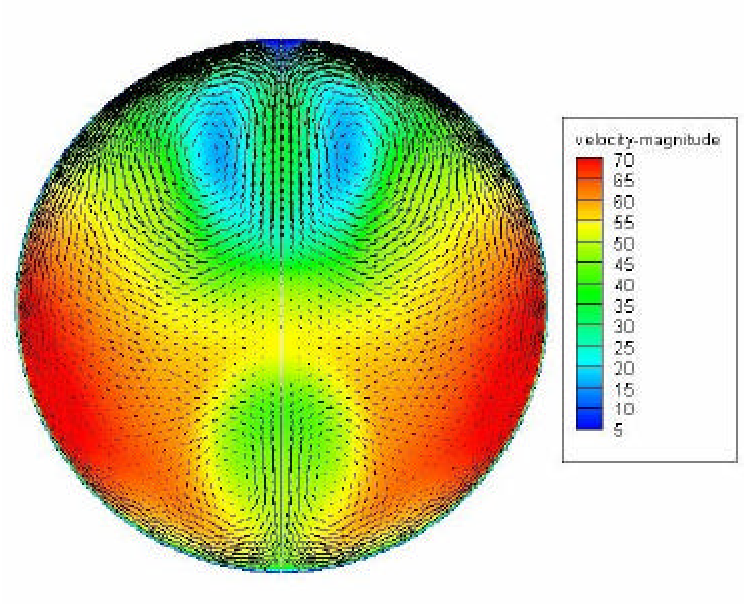

Figure 45: Velocity vectors at outflow plane

Fluidic actuators were integrated for flow control, defined in a way similar to the first bend. The suction slot was placed a small distance upstream of the first saddle point. The blowing slots were similar in dimension to the first bend slots; however 20 individual blowing slots were used for the second bend compared to 12 slots used for the first bend. The slots were made to blow air at a $C\mu$ of .02 which is basically a ratio of the momentum through the slots to the momentum entering through the velocity inlet. For a velocity inlet of 60 m/s. the jet velocity worked out to approximately 70 m/s. Again through mass conservation the suction was made to consume mass flow equivalent to the rate discharged through the slots.

The vector plots shown in Figure 46 and 47 show velocity vectors for the symmetry plane and outflow vectors respectively for the suction-blowing case applied at the second bend. Clearly the vectors at the symmetry plane show a considerable separation delay as marked by the downstream location of the reversed flow vectors, however, contrary to the effect seen for the first bend, the separation could not be eliminated. The outflow vector plots show interesting features. The vector plots vortices stretched towards the duct extremities as opposed to being in the middle for no flow case. This can be mainly attributed to a delayed or weaker boundary layer migration due to flow turbulent mixing caused by high momentum SJA jets. The total face also sees a higher dynamic pressure due to delayed separation. The vortex strength is apparently a little higher for the flow control case than the no control case probably because of delayed evolution of vortices causing lesser viscous dissipation close to the wall and giving concentrated core vortices. Over all, suction and blowing definitely aids in total pressure recovery and flow distortion reduction. However, significant distortion is still prevalent as evident in the vector and total pressure plots.

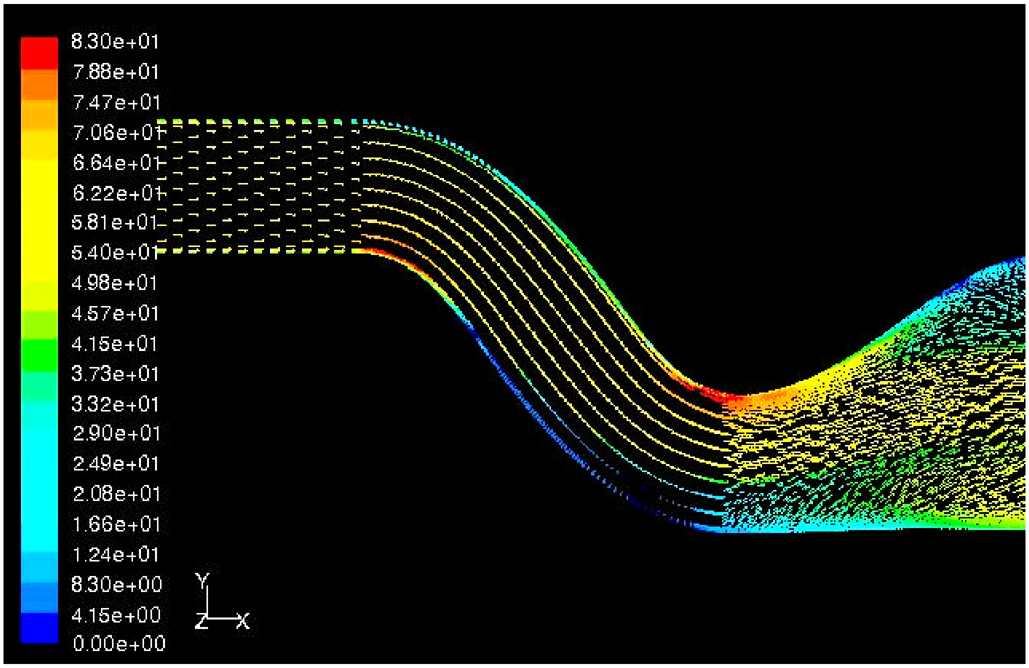

Figure 46: Velocity vectors at symmetry plane for suction-blowing at second bend

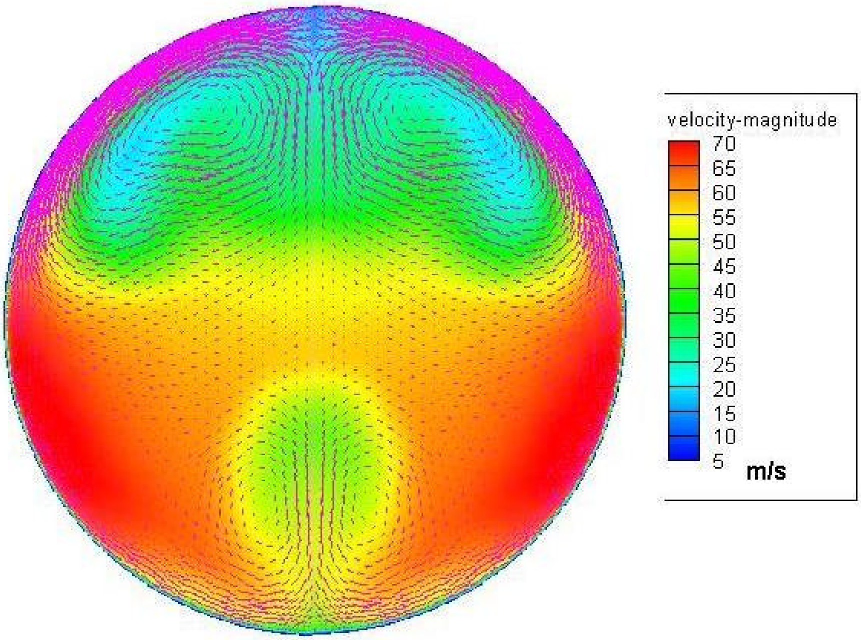

Figure 47: Velocity vectors at engine face for suction-blowing at second bend

Beyond conventional SJA, the only practical option was to introduce vorticity signature in the flow. This required changing the orientation of the blowing slots with respect to the direction of the flow. As discussed earlier in the text, a slot lined parallel to the stream would give a jet with equal strength vortices; however changing the orientation would expose the broad side to the mainstream flow suppressing the upstream vortex and strengthening the downstream vortex.

For studying the effects of slot orientation on jet vorticity a computational test grid was used. The test section had a rectangular cross section, large enough to allow for sufficient diffusion. The slot used had dimensions same as the ones used for experimental and computational simulations. The inlet velocity for the test chamber was maintained at 60 m/s with the jet blowing at 32.5 m/s.

Various cases are discussed in this section pertaining to different slot orientations including slots streamlined with the inlet flow, slots at 30 & 45 degree to the inlet flow, two stream-wise slots blowing into the mainstream flow separated by a small distance and slot blowing at 30 degrees to the slot fact normal. The first case, jet blowing through a slot lined up parallel to the flow vectors shown in Figure 48, clearly shows two vortices evolving with almost equal and opposite vorticity. The slight difference in vorticity and jet orientation is probably due to minor numerical instabilities. Figure 49 shows a jet through a slot aligned at 30 degrees to the velocity inlet. The interaction of the jet with the mainstream flow shows formation of a single strong vortex closer to the wall. This shows the success of introducing desired vorticity into the flow through controlling slot orientation. Figure 50 depicts a jet pattern for a slot aligned at 45 degree to the flow inlet; the pattern is representative of weak disintegrating vortex like structures. This could be an effect of high momentum losses due to large exposure of the broad side of the slot to the mainstream flow. This also indicates a limit to which the slot orientation can be changed to reap benefits from vorticity control. The next case shown in Figure 51 shows two individual slots streamlined, separated by a small distance ejecting jets into the mainstream. The interaction of vorticity produced by jets close to each other can be easily seen. The vortices facing each other exhibit opposite vorticity hence weakening each other. The final case shown in Figure 52 shows maximum vorticity control but is the most difficult to realize in practical scenarios. This involves actually controlling the direction of the inlet jet with respect to the duct surface. For the studied case, the jet was made to blow at 30 degree to the slot normal. A clear strong single vortex in the region of jet inclination can be seen.

Figure 48: Blowing configuration slot at 0 degrees

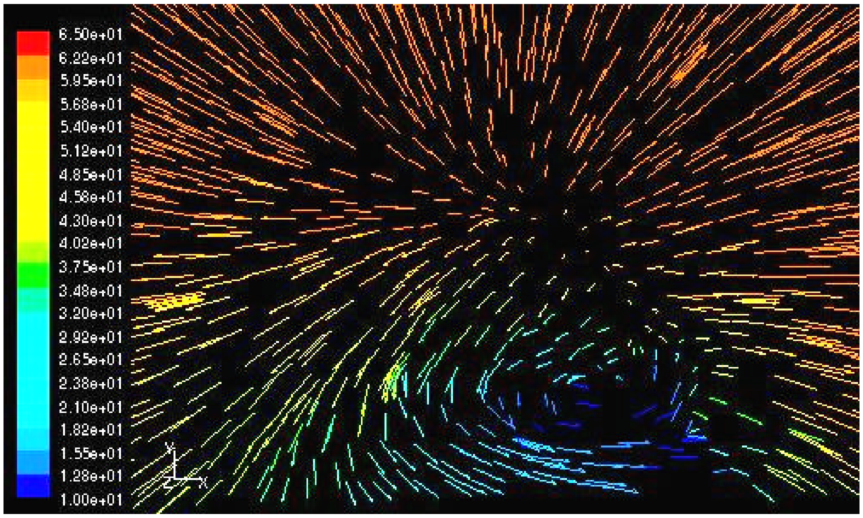

Figure 49: Blowing configuration slot at 30 degrees

Figure 50: Blowing configuration slot at 45 degrees

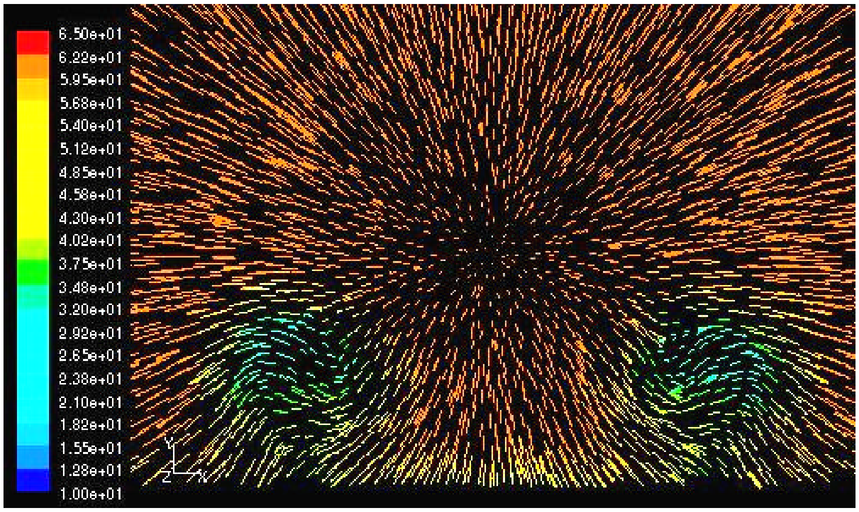

Figure 51: Blowing configuration for two slots 0 degrees close to each other

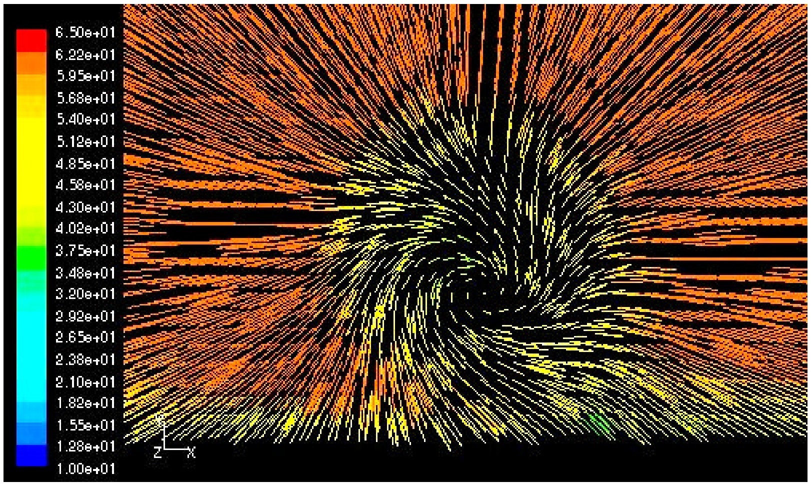

Figure 52: Blowing configuration for jet blowing at 30 degrees to the slot normal

From the slot orientation simulations, last discussed, the slots lined at 30 degrees to the flow direction, appeared to be the most feasible option for the case in hand. The problem remained largely similar to the case with stream-wise slots, with slots orientated in a way as to oppose the secondary flow vorticity. The results for the 30 degree slot blowing and suction are shown in the vector plots below. Figure 53 shows vector plots at the symmetry face whereas Figure 54 shows vector plots at the outflow face. The symmetry plane shows dominant reverse flow vectors in the cross-section transition section unexpectedly worse than the stream-wise slot case; the heavy separation could be representative of momentum losses due to an exposed jet. A single vortex may also be incapable of providing sufficient turbulent mixing, energizing boundary layer to withstand high gradient bends. The vector plots for the outflow face, show strong dominant secondary flow vortices clearly showing the ineffectiveness of the 30 degree slot case. The results depicted are clearly quite different from the expectations and require further investigations as the reasons currently are not clear and can be best attributed to the loss of penetration depth into the mainstream flow due to jet momentum losses at high angles to local flow vectors.

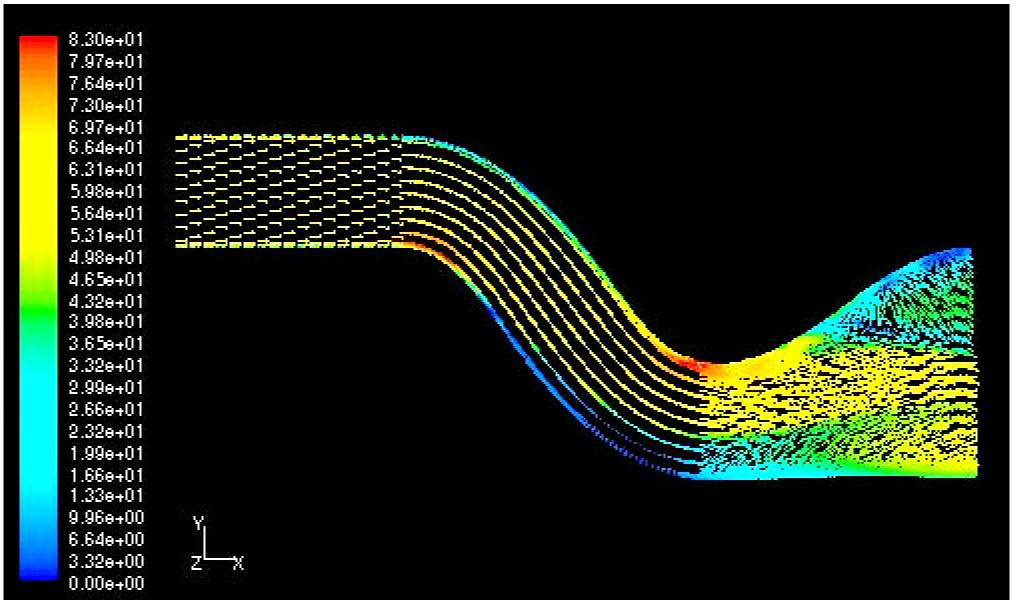

Figure 53: Velocity vectors at symmetry plane for 30 degree slots

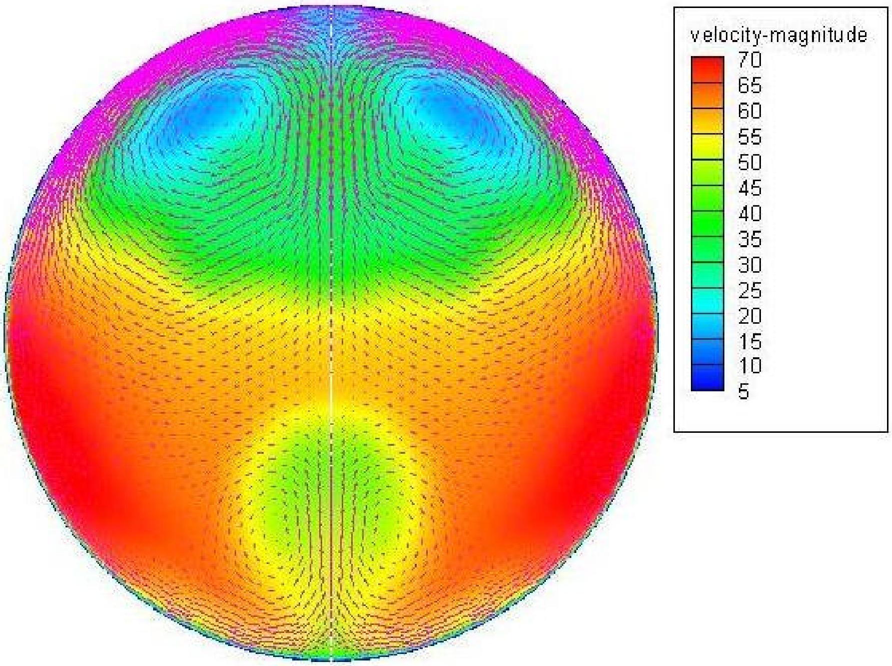

Figure 54: Velocity vectors at outflow plane for 30 degree slots

The total pressure contours as shown in Figure 55 show the comparison for the no control, suction and blowing through stream-wise slots & suction and blowing through 30 degree slots for the second bend at the engine face. The no control case shows excessive total pressure losses from separation and secondary flow formation. The control case with streamline slot shows an appreciable pressure recovery and vortices stretched to the face edges showing a weakened separation and delayed migration. The 30 degree slot case however, shows strong secondary flow vortices with little improvement over the no control case, exhibiting the need for further investigation of the problem.

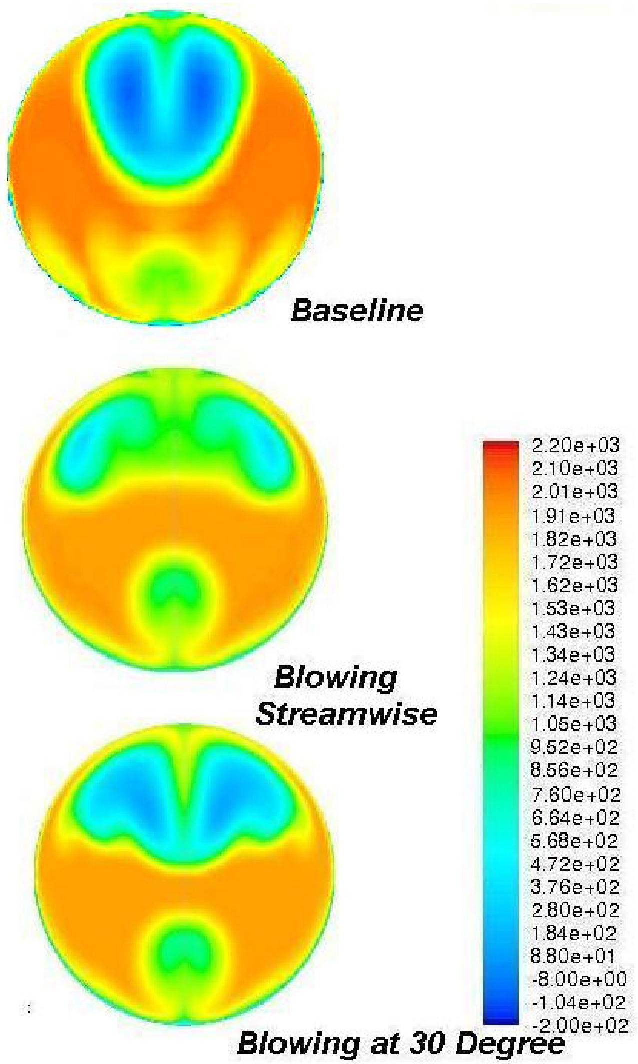

Figure 55: Total pressure comparison for second bend flow control attempts

Improvements from practical amounts of normal blowing jets were below expectations. The conventional flow control techniques at the second bend failed to parallel benefits of flow control seen at the first bend. The angled slots case failed to deliver any significant improvements over the baseline case. On the contrary, blowing through slots at 30 degrees performed worse than the stream wise slots. The angled slot results were clearly unexpected as the introduction of vorticity was assumed to aid in the manifestation of flow control through vorticity signature. The perceived failure could be attributed to many reasons; however no single explanation is convincing enough to explain the observations and would require aid from further studies. In the wake of the aforementioned results, a more radical configuration design was attempted. Unlike all the previous flow control attempts, the idea was to experiment with tangential blowing. Tangential blowing attempts to directly reenergize the deficient boundary layer through jets as opposed to mixing of different fluid layers. The benefits of using tangential blowing were reported by Sun and Hamdam[32] in their computational studies with flow control on a NACA 0012. Tangential blowing was achieved through 16 equally spaced slots spanning the width of the duct at the onset of the second bend. Each of these slots was 1.5 mm to 25.4 mm. Since a perfectly tangential slot is unattainable in real scenarios, a small angle of 10 degrees was imposed between the jet axis plane and the duct surface (Figure 56). The jet momentum coefficient was set at .0014 with the slots blowing at 30 m/s.

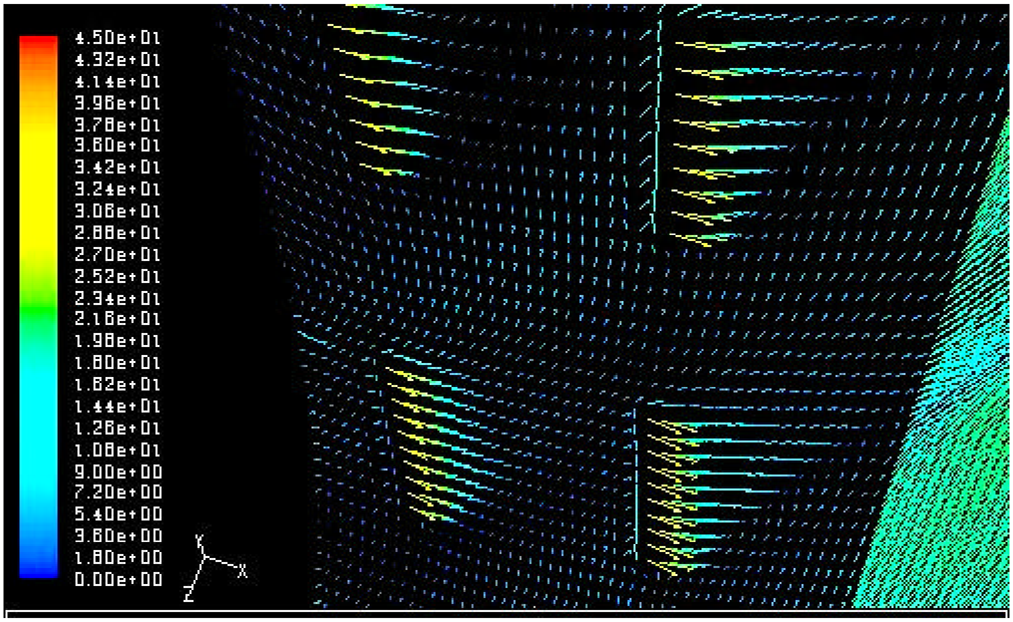

Figure 56: Tangential blowing jets

Tangential blowing with slots blowing at 30m/s proved to be fairly effective in controlling separation and reducing distortion as shown in the comparison between baseline and flow control case shown in Figure 57. Flow control which was applied only to the second bend shows a definite improvement. The distortion, marked by the heavy pressure loss region due to secondary flow vortices shows a significant reduction in size and severity, marking a higher pressure recovery and delayed or weakened boundary layer migration possibly due to redistribution of wall pressure due to tangential blowing.

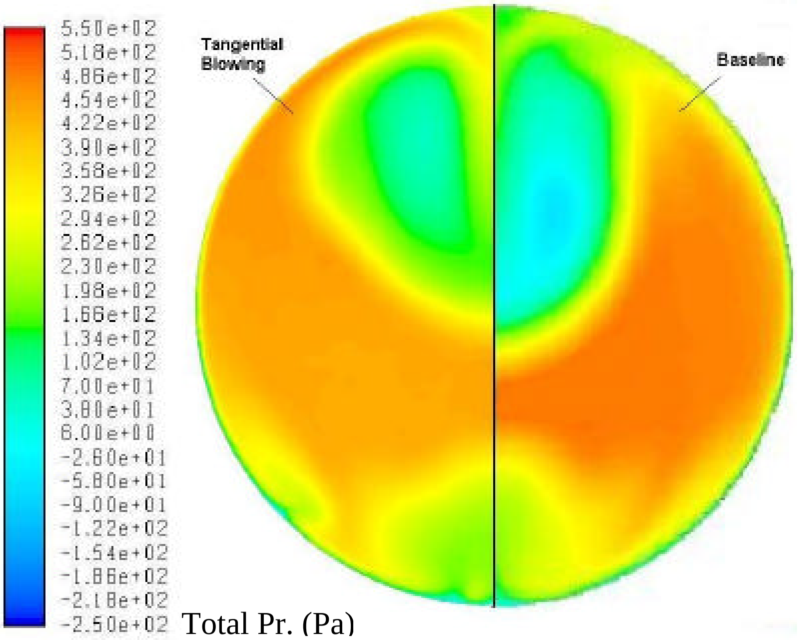

Figure 57: Effect of tangential blowing at engine face

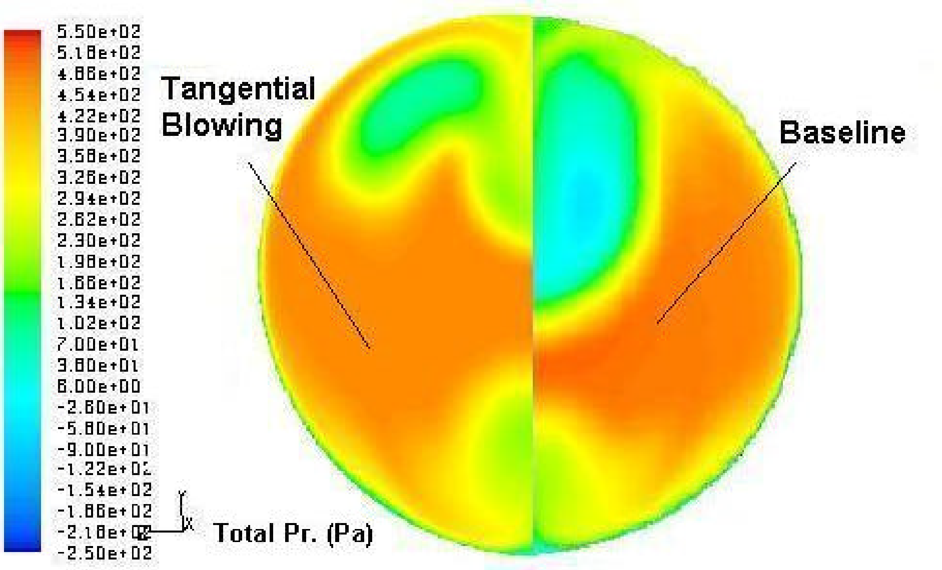

Figure 58: Tangential blowing at higher jet momentum

Higher jet velocities were attempted to simulate the maximum possible jet momentum in experimental simulations. The higher momentum case with tangential jets blowing at 35 m/s showed a definite change in distortion pattern as compared to the 30 m/s case. Higher jet momentum (figure 58) shows a small vortical structure stretched closer to the wall. This is a definite indication towards a delayed liftoff as compared to the discussion following results in Figure 57. The weakened and smaller vortex at the engine face is also representative of further decreased distortion attributing more credibility to tangential blowing.

Tangential blowing proved to be more effective than normal blowing in terms of distortion reduction and hence appeared to be a plausible solution for this particular problem. Tangential blowing, unlike the normal blowing attempts, did not introduce a net vorticity in the core flow and theoretically exhibits no such mechanism to attack counter rotating vortices. However, blowing tangentially to the wall definitely redistributes wall pressures possibly decreasing the span-wise pressure differential hence theoretically weakening the foundation of boundary layer migration.

EXPERIMENTAL INVESTIGATIONS

Bench Top Tests

The fluidic actuators designed for studies presented in this thesis were subject to bench top testing to monitor their performance as a function of the pressure gradients across the blower fan or the suction and blowing plenum. These tests were conducted in a way similar to the descriptions presented by Guy et al.[33] in their study pertaining to synthetic jet velocity measurement. The pressure across the centrifugal fan in the actuator assembly decreases the jet velocity through the slots. A study which measures the synthetic jet characteristics is important to relate synthetic jet velocity to the fan RPM and pressure gradient. The tests were conducted for both the 3 slot and 5 slot cases (Figure 59 & 60). The calculated uncertainty of the bench top tests was limited to a maximum 1.43 m/s for a 95% confidence level.

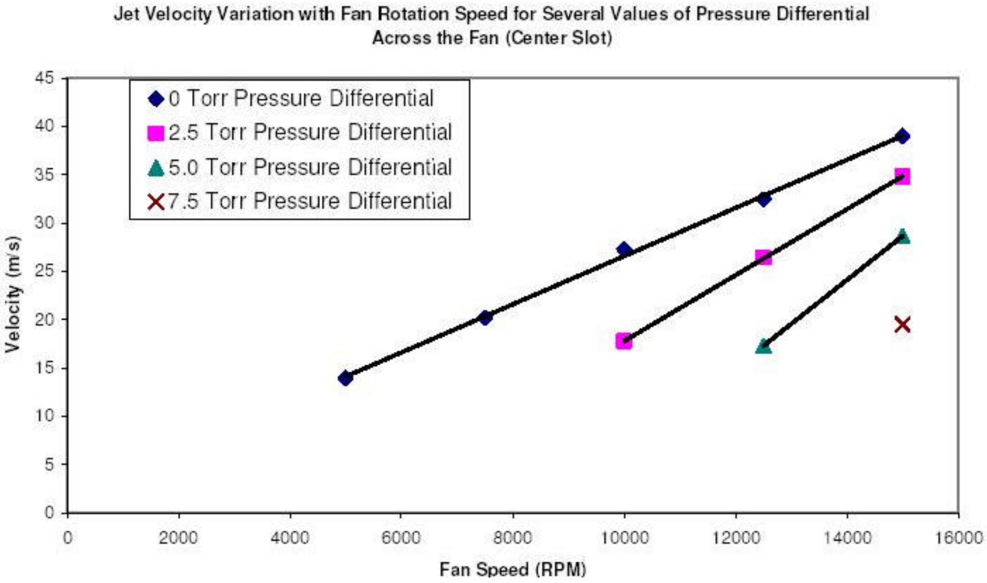

Figure 59: 5 Slot plate performance

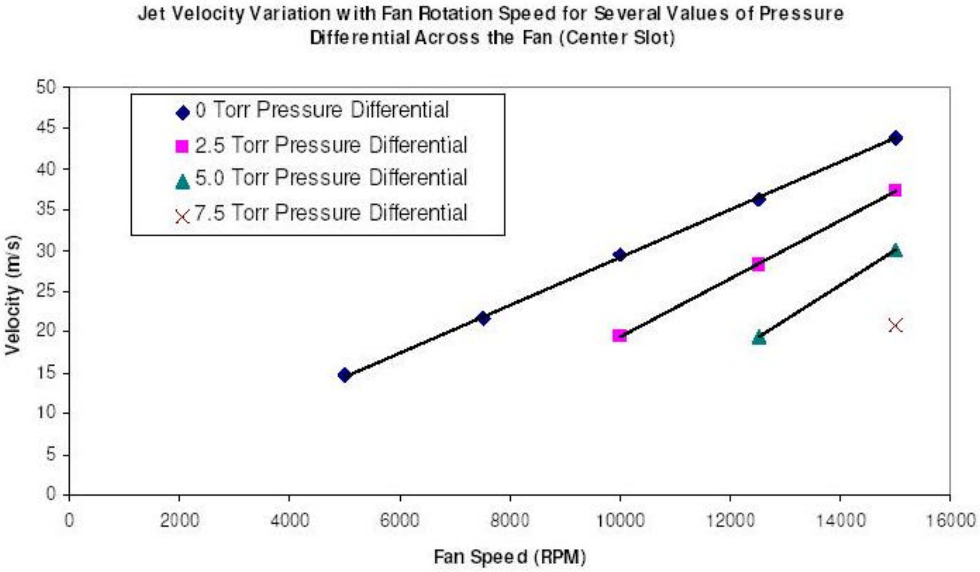

Figure 60: 3 Slot plate performance

Experimental Results

Experimental simulations were carried out for various SJA slot configurations. The configurations were changed simply by replacing the slot plates. Experimental analysis for each configuration included a complete probe rake survey of the engine face to obtain total pressure face contours and acquisition of wall static pressure distributions for both the top and bottom surface of the duct along the mid axis.

Engine face surveys were done by the probe rake as described earlier. Earlier research at Texas A&M had used 7 hole probe for engine face surveys, though the total pressure contours obtained from multi-hole probe and probe rake were identical, the 7 Hole Probe could generate 3 dimensional velocity vector plots on the engine face. Even though, vector plots provided useful insights on the secondary flow characteristic at the engine face, for all practical purposes the total pressure contours were sufficient. Losses in total pressure were indicative of presence of large secondary flows which related to the core problems with serpentine duct flows. The 32 single hole probes were read real time by an ESP. Static pressure distributions were obtained by using by reading the pressure values at 25 pressure taps on the top surface and 18 taps on the bottom surface through the same ESP used or probe rake survey. Wall static pressures can provide valuable insights into the flow characteristics. Wall static pressures distributions proved to be particularly useful in relaying separation location, extent and recovery, also providing a parameter to gauge the effectives of flow control apart from face plots.

Previous research at Texas A&M had concentrated on interaction of jets through stream-wise slots only. As observed in earlier research, this orientation can introduce a pair of equal strength counter rotating vortices with zero net vorticity, however to use the principle of vorticity signature angled slots similar to the ones described by Bridges and Smith[14] were used in later attempts. The slots were oriented so as to introduce the correct vorticity into the flow to oppose the locally encountered secondary flow vorticity. Since the Slots were spread span-wise, each slot had to be oriented in order to account for the local mainstream flow conditions. Also since the secondary flow vorticity revered direction at the symmetry axis of any cross-sectional plane, the slots also were actually mirrored about the symmetry plane to produce opposite vorticity at either side. The blowing strength was measured by a non dimensional factor called C_μ. The factor follows the definition (equation (6)) derived from the one used by Amitay et al.[34] in their tests 2-D diffuser ramps.

$$C_m = \frac{\left(r \cdot U^2 \cdot l \cdot w \cdot n \right)_{jet}}{\left(r \cdot U^2 \cdot A \right)_{duct}} \tag{6}$$

The variables in the above equation follow the standard definitions, ? is the density, U is free stream velocity at inlet for the duct and the exit velocity of the jet for SJAs. A is the area of the duct inlet; l is the length of the slot, w is the width while n is the total number of slots. The uncertainty in C_μ comes from various variables incorporated in equation (iv). Uncertainty in U_{duct} comes from the uncertainty of the handheld manometer while the errors may come from pitot tube placement and tubing. Density was also read from the manometer which was calculated by simple ideal gas law. The uncertainty in density was mainly due to uncertainty of the manometer in reading atmospheric pressure and temperature and also due to minor compressibility effects; however these effects could be safely neglected. The uncertainty in U_{jet} was probably the highest contributor to uncertainty in the value of C_{μ}. As the values for the jet velocity were obtained from bench top tests conducted for a range of pressure differentials. These results assumed a constant jet velocity over the entire span of the slot, moreover the same velocity over all the slots. The values used also related to a zero pressure differential across the SJA fans, however, real time data gathered from the differential pressure sensors used to monitor pressure differential across the suction and blowing surfaces showed a small adverse pressure gradient of less than 0.5 torr, which could have related to further reduced values in velocities, not accounted for. The uncertainties in l and w were encountered mainly due to loose tolerances attained through rapid prototyping of components; these tolerances were small enough to not significantly influence the uncertainty of C_{μ}. The uncertainties in the values for Cμ were approximated close to 5% using the approach described earlier. For all the experimental runs, the inlet duct velocity was maintained at 30 m/sec. For each configuration SJA jet velocities were varied by changing the centrifugal fan speed from 0 RPM for baseline to 15000 RPM in steps of 2500 RPM.

5 30 Degree Slots

As an initial attempt to counter vorticity in agreement with the concept of vorticity signature, slots at 30 degree to the local free stream were employed. 5 slots were used on each of the four plates as with the case with earlier attempts at Texas A&M University. The 5 – 30 degrees slot plates as shown in Figure 61 were installed for both the first and second bend actuator setups. The static pressure distributions over the length of the duct are shown in Figure 62 and 63. One of the major problems encountered due to the installation of SJAs was their interference with the external profile of the duct, making a large portion of the external duct area near the bends inaccessible for installation of static taps. Integration of surface taps with SJAs was ruled out due to the many possible geometry complications. These drawbacks eventually made the distribution curves deficient of various points near the bends; however the important flow characteristic could still be captured and interpreted. The Bottom Surface distributions show a steep dip at the first bend. The recovery region however shows a slightly erratic distribution for lower RPMs of the centrifugal fan. The recovery curve shows a definite smoothening along with an increased slope for higher RPMs indicative of delayed or eliminated separation. The top surface distribution which captures the more crucial second bend shows a similar trend with increase in RPM. Though none of the distributions show a complete elimination of separation, a definite delay trend can be seen with increase in jet velocities. RPMs under 10000 show no significant improvement over baseline, however higher RPMs show a smooth steep recovery though eventually leading to separation in the later part of the transition region of the duct. The total pressure contours at the engine face (Figure 64) show an agreement with wall pressure data. The plots compared to baseline show an improvement with an increase in C_μ or jet momentum. The secondary flow vortices; move closer to the wall with increase in fan velocities representing a delay in flow separation and vortex liftoff locations. The vortices at higher amounts of flow control are denser but show lower diffusion hence giving higher total pressure elsewhere. These observations point at a later boundary layer migration eventually a delay in liftoff of secondary flow vortices. Though even at higher RPMs a significant distortion can be seen, a reduction of 32% in distortion and an improvement of 24% in Cp_{loss} is observed for C_μ of 0.024 as seen in Table1. The weaker distortion from first bend shows an almost complete elimination over distortion from second bend which shows its dominant presence even for the lowest distortion case. The 5 30 degree slots fail to show an improvement over their stream wise equivalent. This was unexpected and gave rise to speculations on the effects and implementation of angled plates to exploit vorticity signature.

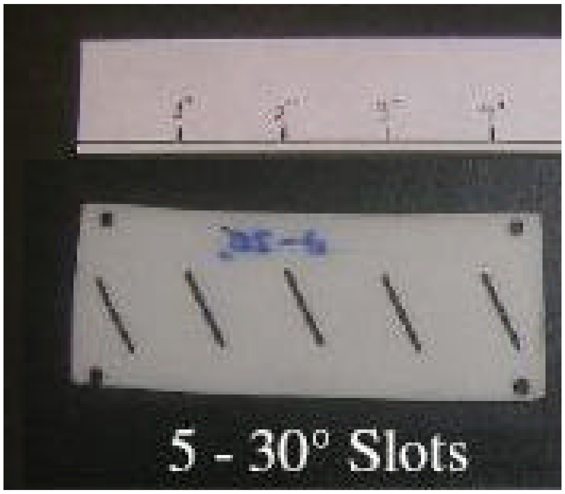

Figure 61: 5 – 30° slot plate

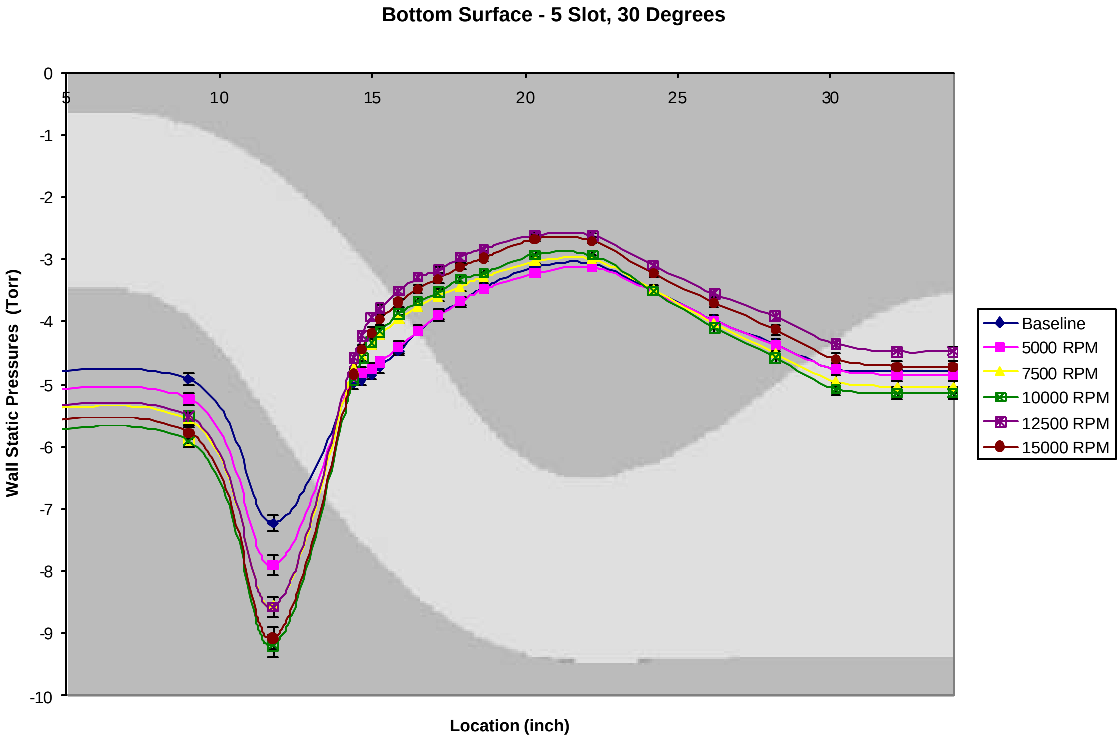

Figure 62: Bottom surface pressures 5 slot, 30 degrees

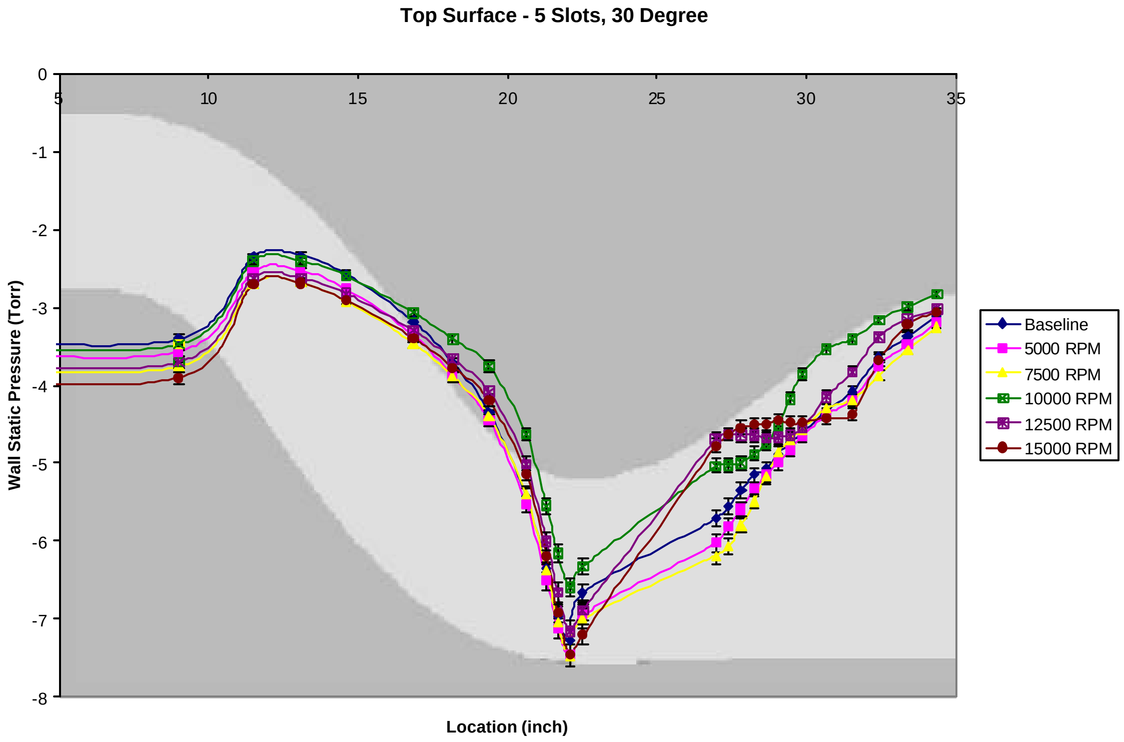

Figure 63: Top surface pressures 5 slot, 30 degrees

Table 1: Duct performance descriptors for 5 slots 30 degrees plates

Fan Speed (RPM)	Jet Velocity (m/s)	C_m	Mass Flow	$C_{Ploss,avg}$	DC_{60}
0	0.0	0.0	0.0 %	51.39 ± 0.98	99.34 ± 4.09
5000	13.5	0.0029	0.63 %	44.19 ± 1.32	85.12 ± 3.57
7500	20.0	0.0063	0.94 %	40.87 ± 1.22	91.76 ± 3.78
10000	26.5	0.011	1.24 %	35.34 ± 1.13	87.00 ± 3.47
12500	33.0	0.017	1.54 %	28.80 ± 0.92	74.34 ± 3.36
15000	39.5	0.024	1.85 %	27.40 ± 0.88	67.43 ± 3.09

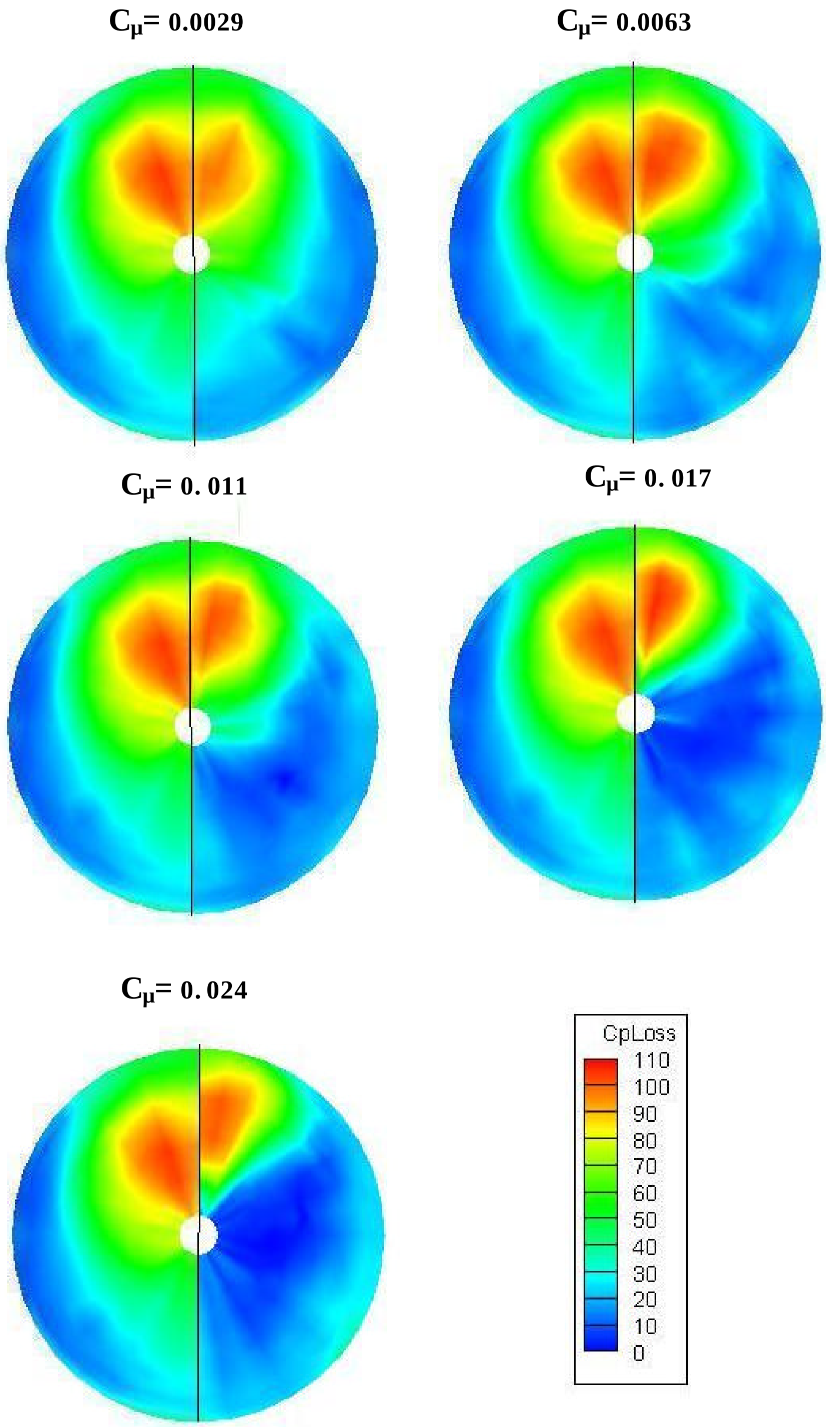

C_μ= 0.0029

C_μ= 0.0063

C_μ= 0. 011

C_μ= 0. 017

C_μ= 0. 024

Figure 64: Cploss for 5, 30 degree slots per plate case

Changing the orientation of slots for 5 slot plates proved to do be lesser effective than expected in controlling flow distortion at the engine face. These results called for further probing and reconsidering the implementation of SJAs for the duct geometry. The 5 slot configuration could have had slots close enough for each other to have interfered with each others jet vorticity, an effect possibly detrimental for secondary flow control as shown in CFD simulation showing two slots ejecting close to each other. A reduction in number of slots was contemplated which would possibly lead to higher momentum through each slot enabling an increased penetration with higher mixing. The interference with vortices from adjacent jets would be lower as well, this could be particularly important when targeting particular vorticity through the jets as required in countering secondary flow vorticity.

Three slot configurations were thus tried in subsequent experimental studies, with a hope of higher localized momentum through lesser slots enabling higher turbulent mixing through jets. Though the bench top tests for these configurations did not show a significant increase in momentum over 5 slot equivalents, the effects of increased separation between slots motivated further studies on these configurations.

The flow configurations tested included stream-wise blowing, blowing at 10 degrees and 30 degrees to the streamlines. Standard conditions were maintained for test as explained for earlier tests. These configurations were designed and installed separately for both bends. Comparisons are provided for total pressure at the engine face for all attempted $C\mu$'s.

3 Stream Wise Slots

The 3 Slot stream-wise plates (Figure 65) show little improvement over baseline results, they apparently weaken the effects of separation and secondary slow distortion, however, failing to show any substantial improvement. The results look better for higher fan RPMs but definitely not better than the 5 slot case. The wall static pressures shown in Figure 66 and 67 show a definite improvement with increase in jet momentum. The first bend separation captured by baseline bottom wall static pressures shows a gradual delay with increase in RPMs with an almost complete elimination at higher RPMs marked by a smooth and steep recovery. The ineffectiveness of the technique at the second bend is clearly depicted by closely coinciding recovery patterns for all RPMs. Though higher RPMs show a delay in separation, the slight improvements are mainly insignificant as opposed to the earlier configurations. The engine face total pressure (Figure 68) plots show little reduction in distortion. The effects of flow control cease to get any better at the Cμ 0.0081 depicted in Table 2 These results were somewhat expected as the stream wise slots did not introduce any net vorticity in the flow, on the contrary a reduction in number of slots had caused a decrease in net jet momentum at a specified RPM as can be seen in Table 2 when compared to Table 1. The main purpose of using 3 stream wise slot plates was to develop a basis of comparison for angled 3 slot plates so as to isolate the effects of vorticity induction.

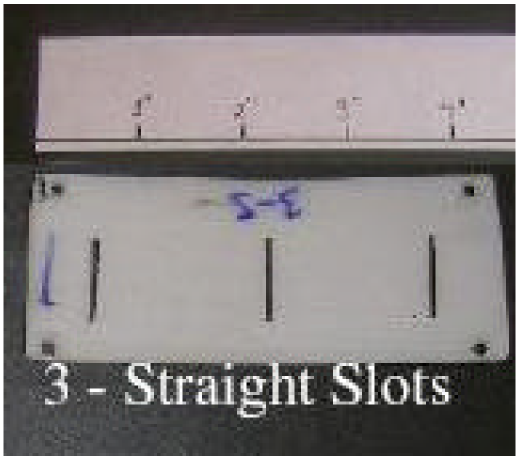

Figure 65: 3 Stream-wise slot plate

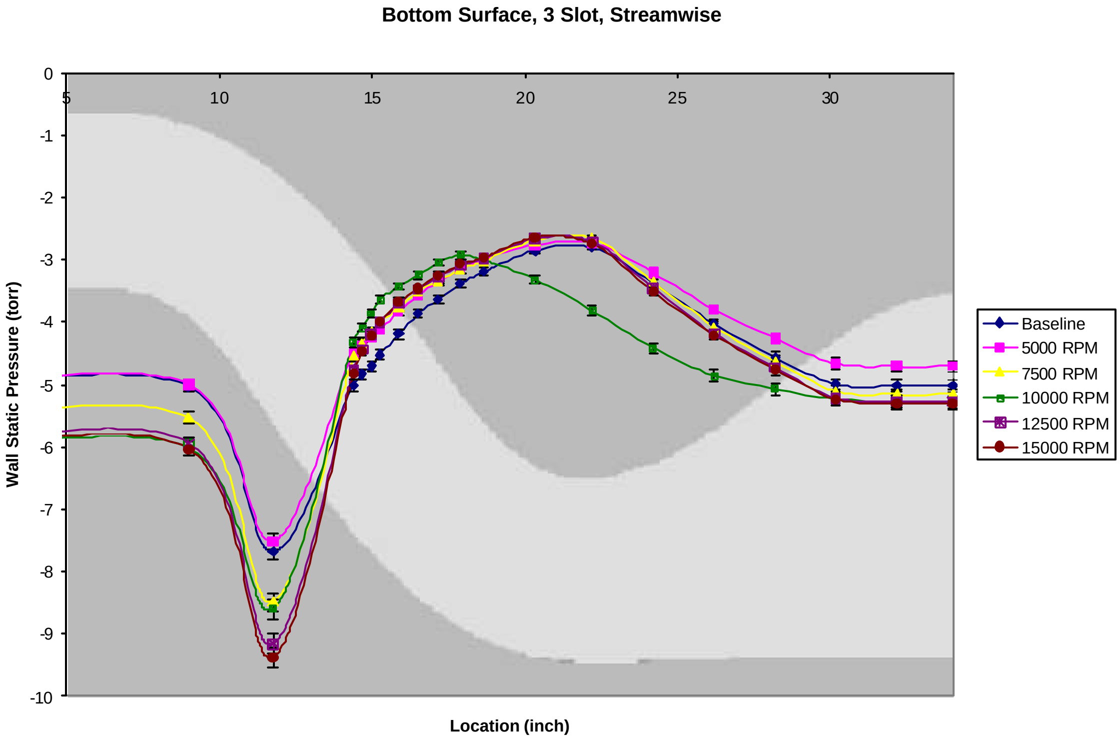

Figure 66: Bottom surface pressures 3 slot, stream-wise

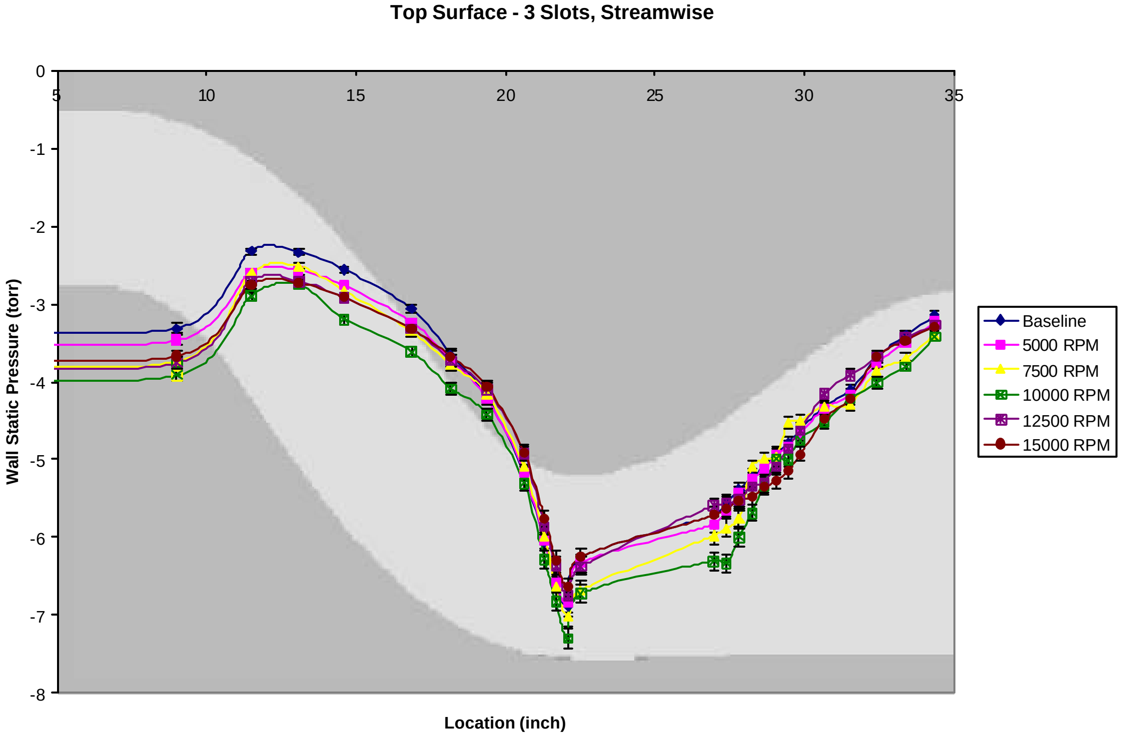

Figure 67: Top surface pressures 3 slot, stream-wise

Table 2: Duct performance descriptors for 3 slots streamwise plates

Fan Speed (RPM)	Jet Velocity (m/s)	C_m	Mass Flow	$C_{Ploss,avg}$	DC_{60}
0	0.0	0.0	0.0 %	46.29 ± 1.38	90.26 ± 3.61
5000	14.67	0.0020	0.41 %	45.46 ± 1.34	105.68 ± 4.43
7500	21.80	0.0044	0.61 %	41.37 ± 1.24	110.30 ± 4.55
10000	29.42	0.0081	0.82 %	36.93 ± 1.18	100.56 ± 4.02
12500	36.25	0.0123	1.01 %	35.16 ± 1.13	97.79 ± 4.42
15000	43.88	0.0180	1.23 %	37.03 ± 1.19	106.94 ± 4.9

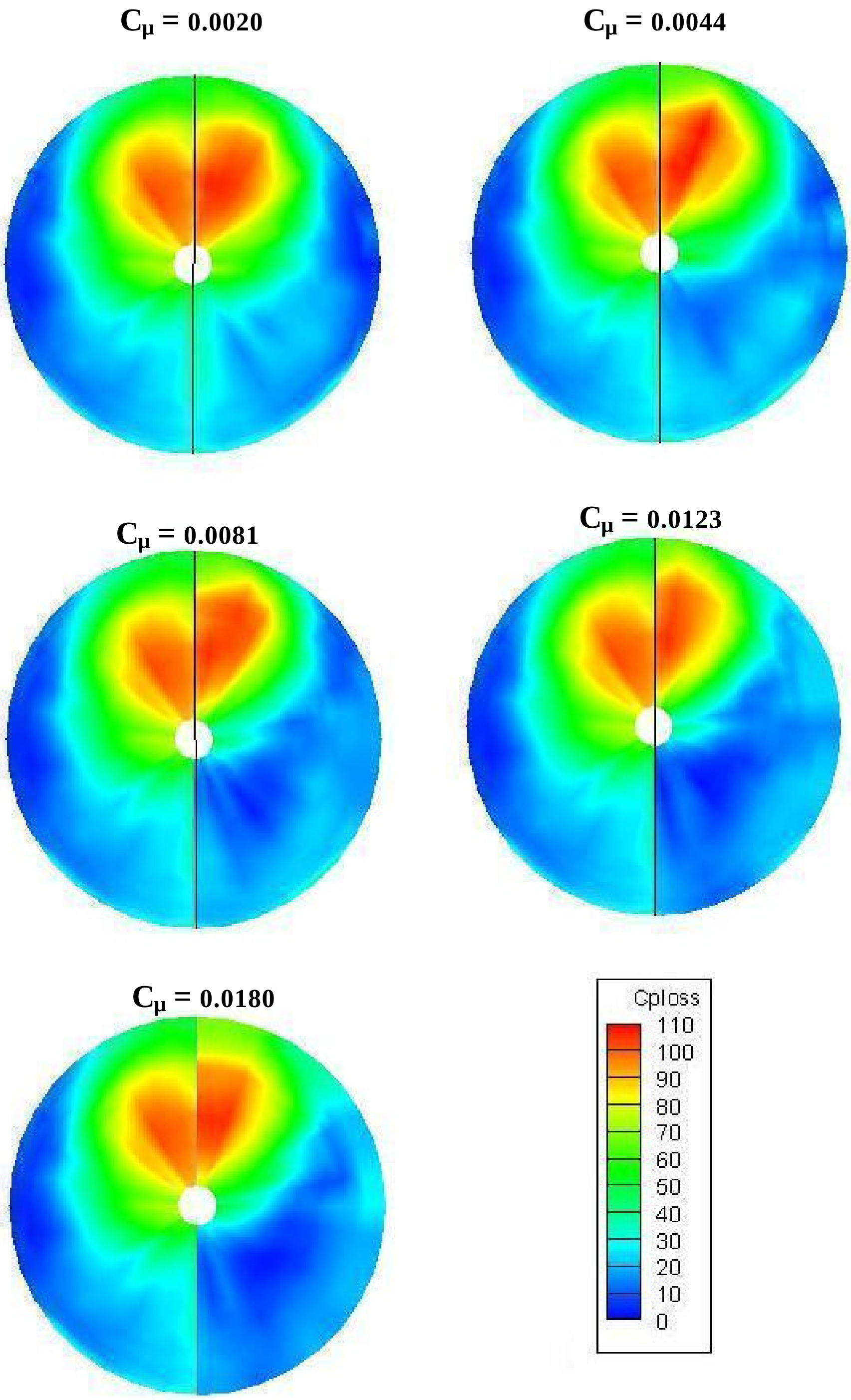

Figure 68: Cploss for 3 streamline slots per plate case

3 10 Degree Slots

For initial tests with angled slots, smaller angles of 10 degree to local free stream were used (Figure 69). As explained earlier the slots were oriented so as to introduce a net vorticity opposite to the local secondary flow vorticity. As observed for most of the earlier cases, the less severe first bend shows good recovery curves for even small amounts of synthetic jet momentum as shown in Figure 70. The top surface static pressure distributions (Figure 71) show a definite improvement over the stream-wise slot case, Figure 67. Though separation can be seen for all RPMs, a definite delay patter can be seen with increase in RPMs. Higher RPMs show a smooth initial recovery curves before eventually leading to separation under adverse recovery pressures giving random fluctuations in the recovery region. The total pressure face plots shown in Figure 72, show an improvement trend with increasing C_μ. The distortion shows a gradual diminishing accompanied by weakening vortices. The vortices also appear to move closer to the wall with higher C_μs signifying a weakening migration due to induced jet vorticity resulting in delayed vortex lift-off. Even though the results shows a gradual improvement with increasing jet momentum and slightly better results than 3 stream wise slot case which can be attributed to the jet vorticity, the results fall behind 5 slot cases by a significant margin with an improvement in Cp_{loss} of just 14% as seen in Table 3.

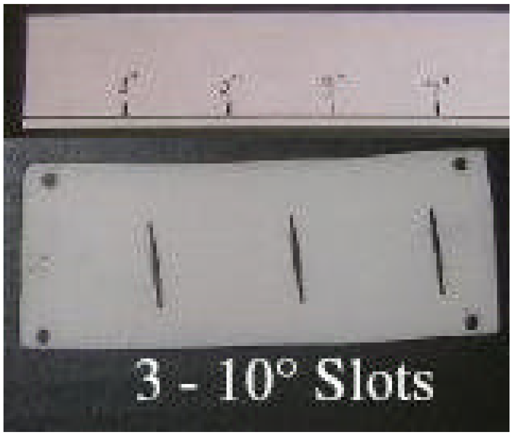

Figure 69: 3-10° slot plate

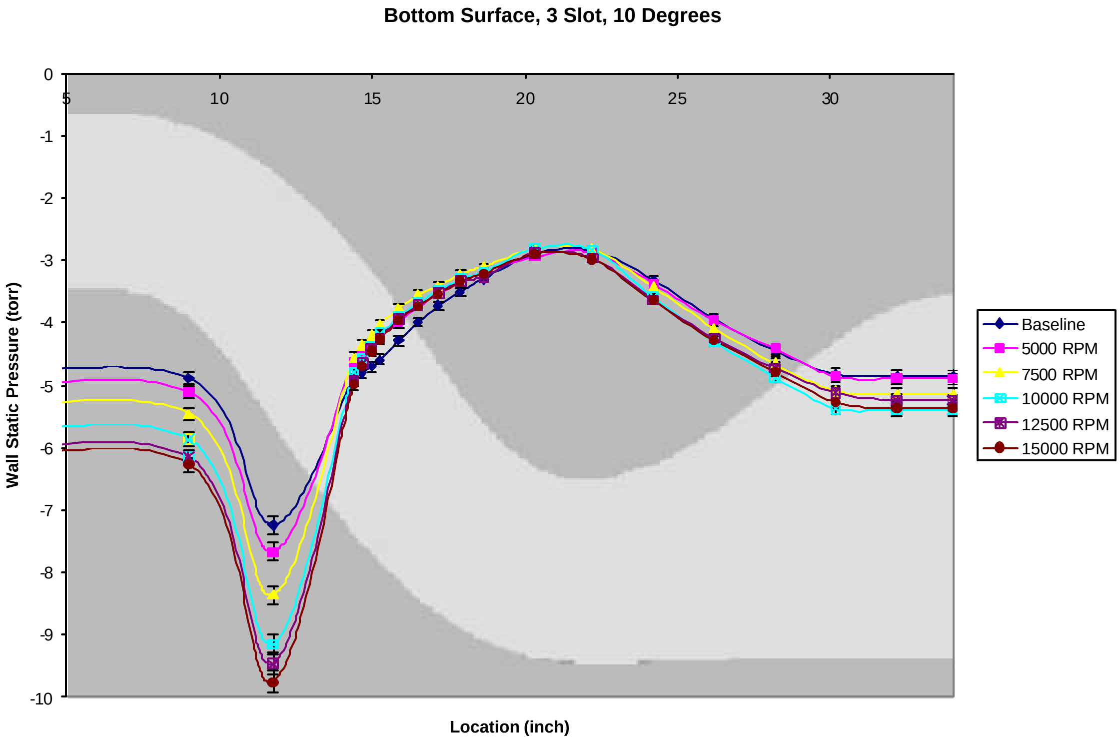

Figure 70: Bottom surface pressures 3 slot, 10 degrees

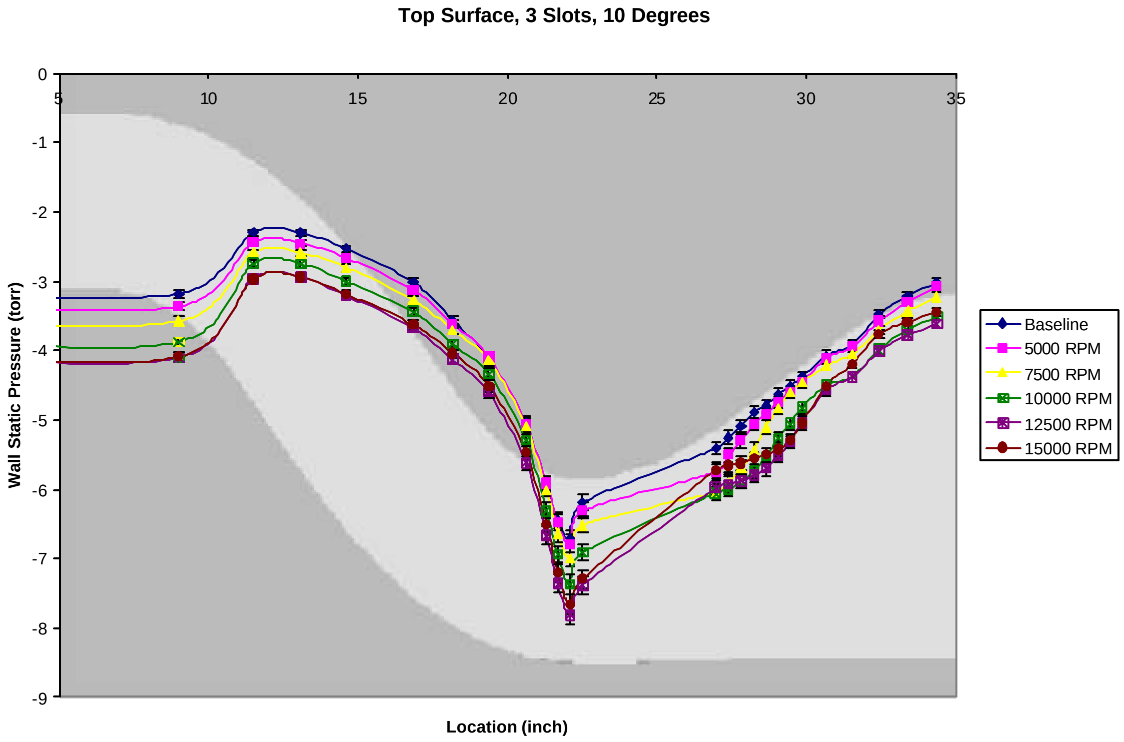

Figure 71: Top surface pressures 3 slot, 10 degrees

Table 3: Duct performance descriptors for 3 slots 10 degrees plates

Fan Speed (RPM)	**Jet Velocity (m/s)**	C_m	**Mass Flow**	$C_{Ploss,avg}$	DC_{60}
0	0.0	0.0	0.0 %	47.96 ± 0.91	93.46 ± 3.86
5000	14.67	0.0020	0.41 %	44.94 ± 1.33	107.54 ± 4.50
7500	21.80	0.0044	0.61 %	41.49 ± 1.24	109.02 ± 4.49
10000	29.42	0.0081	0.82 %	38.42 ± 1.23	103.02 ± 4.15
12500	36.25	0.0123	1.01 %	34.77 ± 1.17	97.58 ± 4.42
15000	43.88	0.0180	1.23 %	34.15 ± 1.10	93.53 ± 4.29

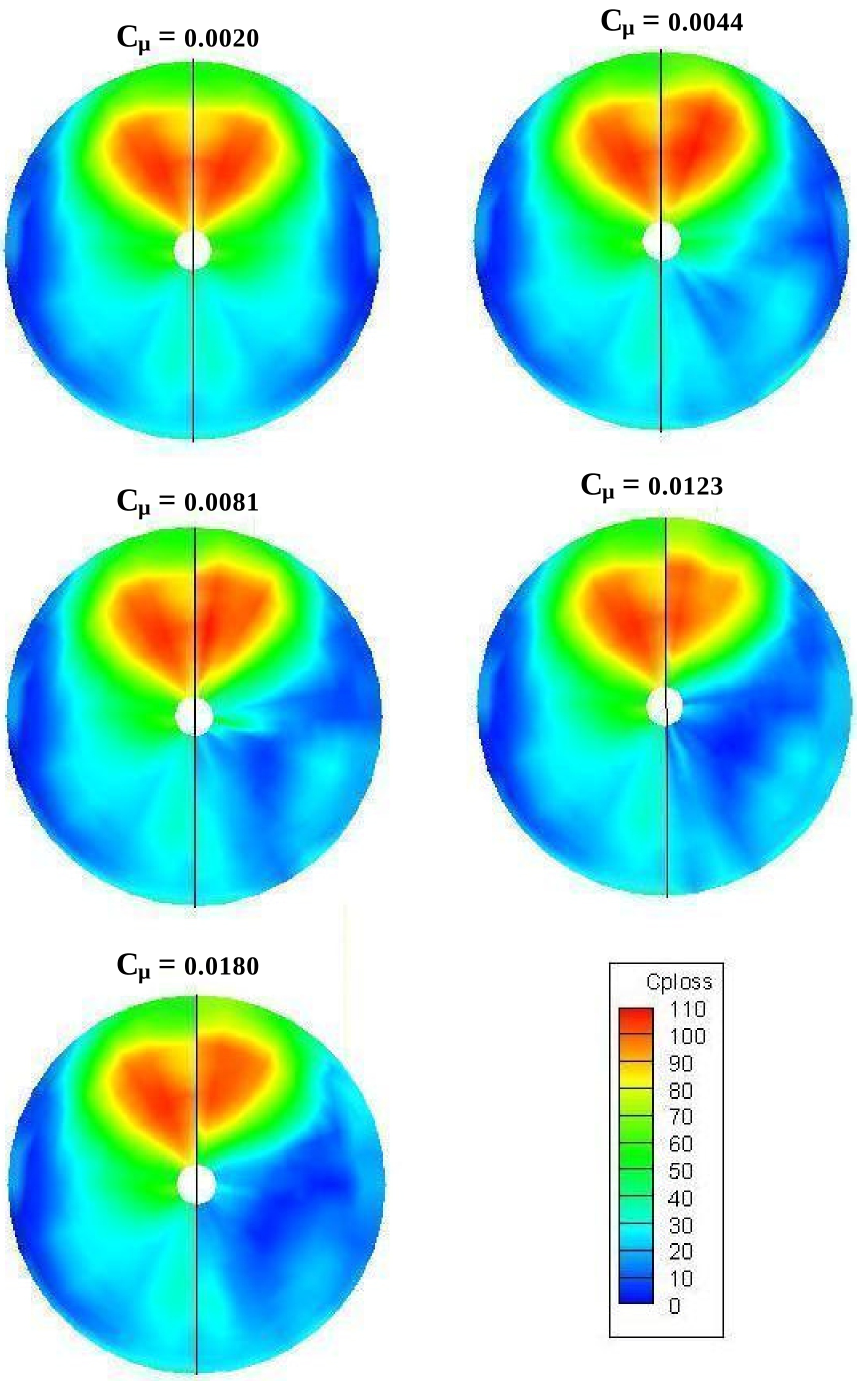

C_μ = 0.0020

C_μ = 0.0044

C_μ = 0.0081

C_μ = 0.0123

C_μ = 0.0180

Figure 72: Cploss for 3,10 degree slots per plate

3 30 Degree Slots

A straight slot at 30 degree to the free stream gives a single strong vortex at the downstream side of the slot as seen from the CFD simulations, at higher angles though the vortices start to disintegrate accompanied by lower penetration in the free stream. The 30 degree 3 slot configurations shown in Figure 73 were the final attempt with normal blowing to be tried on the serpentine duct model. The wall static pressures showed no significant improvement over previous results. As seen in earlier results the wall static pressure at the first bend visible in Figure 74 shows almost coincident recovery curves for all fan RPMs with no signs of separation at any downstream location, clearly representative of the success of flow control in eliminating at the less severe first bend. The crucial second responsible for maximum total pressure losses at the engine face however shows strong resistance to flow control. As seen in Figure 75, smaller RPMs of 5000 and 7500 show almost no improvement over baseline results, higher RPMs show slight delay in separation but eventually lead to separation a small distance downstream to the second bend. The total pressure contours (Figure 76) show a certain improvement till the C_μ of 0.0081 at 10000 RPM over the earlier 3 slot configurations attributing the gains to countering vorticity signature; however the results clearly deteriorate at higher RPMs also supported by Table 4, a result definitely counter-intuitive. Further investigations and theory would be required to support these results before this phenomenon can be effectively addressed.

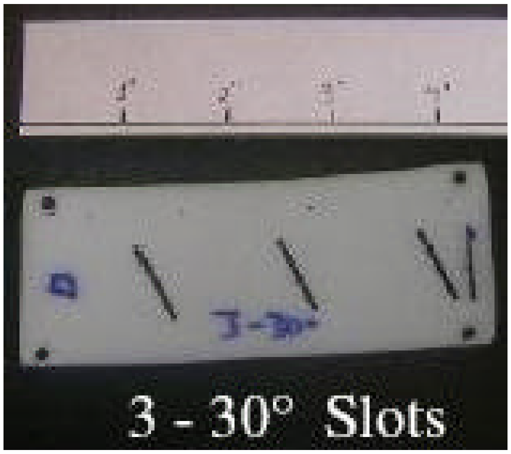

Figure 73: 3-30° slot plate

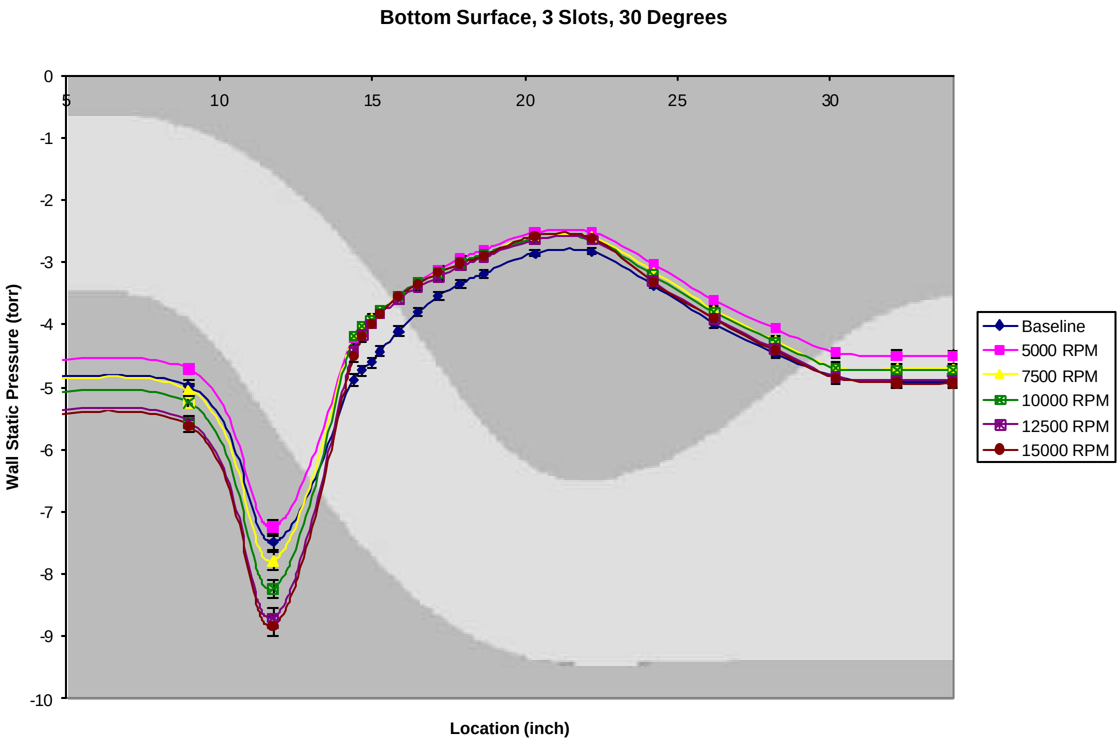

Figure 74: Bottom surface pressures 3 slot, 30 degrees

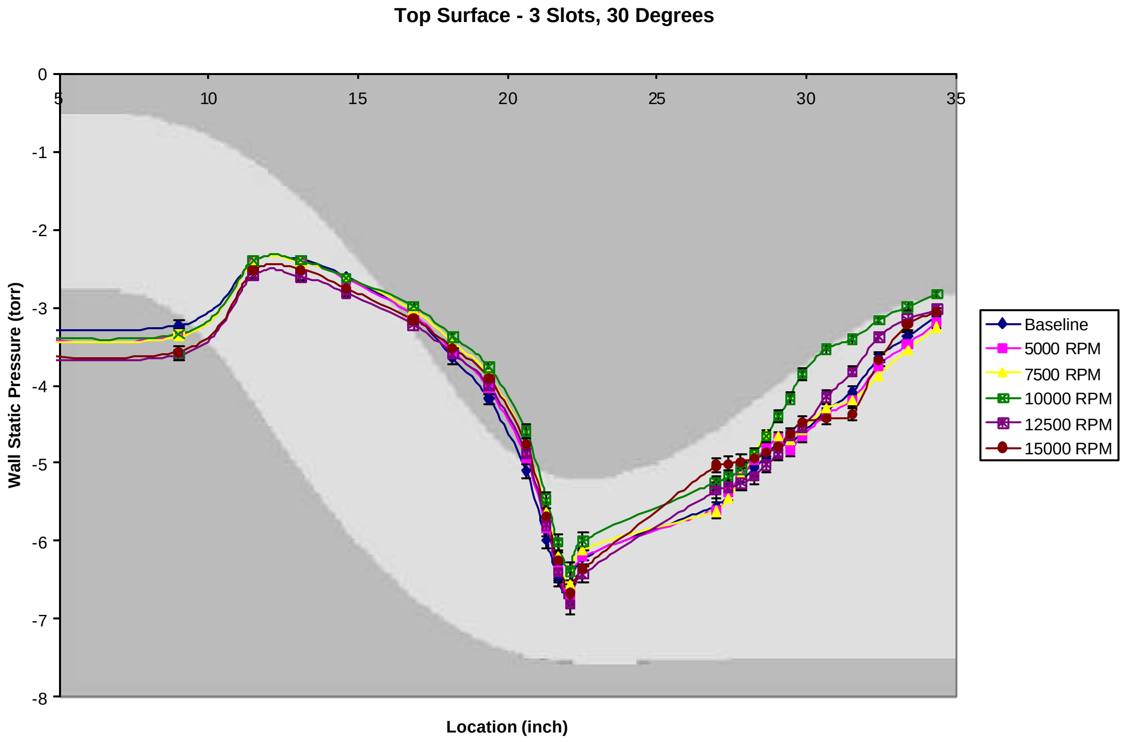

Figure 75: Top surface pressures 3 slot, 30 degrees

Table 4: Duct performance descriptors for 3 slots 30 degrees plates

Fan Speed (RPM)	Jet Velocity (m/s)	C_m	Mass Flow	$C_{Ploss,avg}$	DC_{60}
0	0.0	0.0	0.0 %	45.58 ± 0.87	90.00 ± 3.72
5000	14.67	0.0020	0.41 %	42.92 ± 1.28	101.00 ± 4.24
7500	21.80	0.0044	0.61 %	36.71 ± 1.10	94.27 ± 3.89
10000	29.42	0.0081	0.82 %	32.87 ± 1.05	90.31 ± 3.61
12500	36.25	0.0123	1.01 %	37.16 ± 1.19	113.77 ± 5.13
15000	43.88	0.0180	1.23 %	35.03 ± 1.13	110.35 ± 5.06

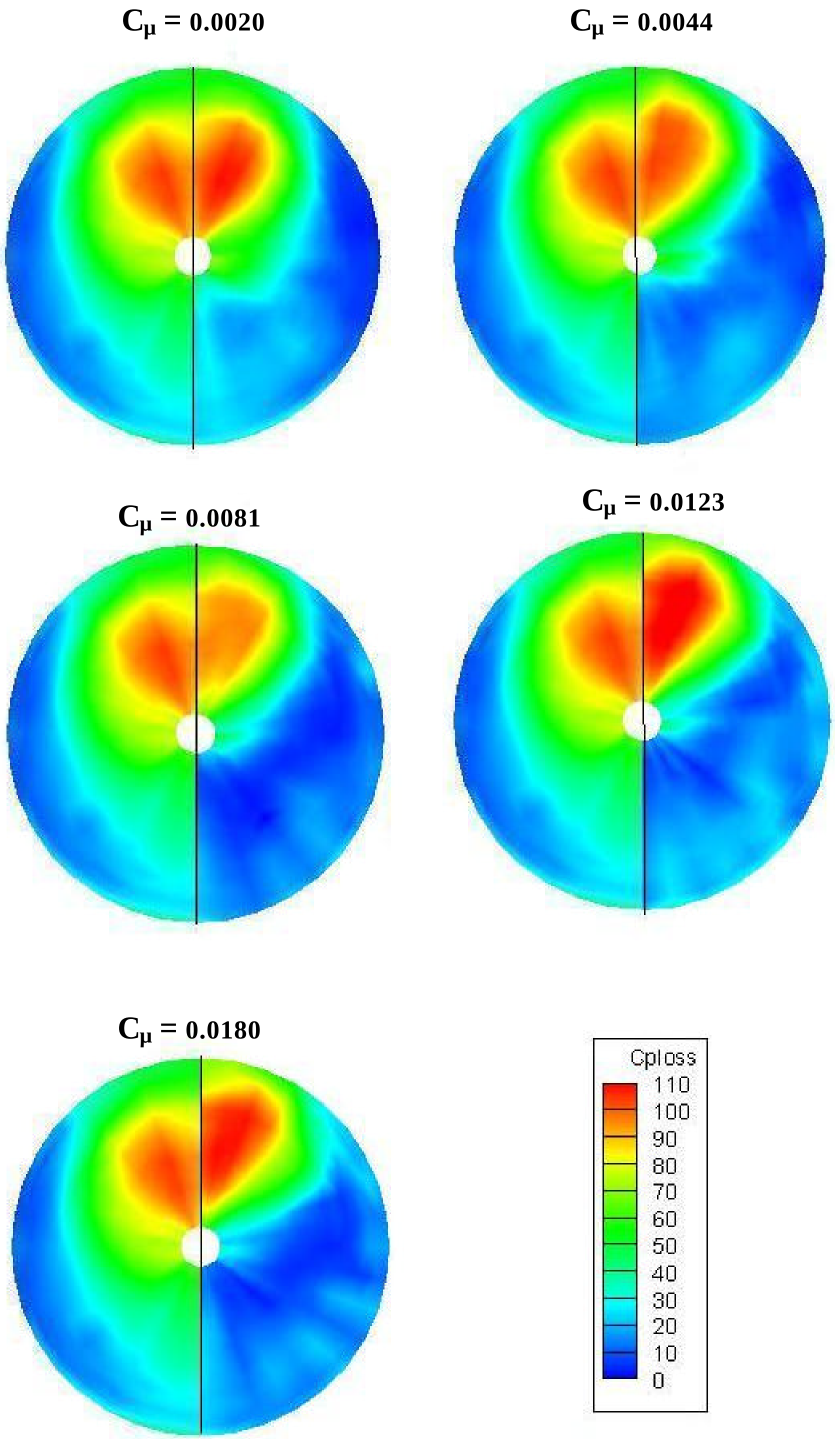

Figure 76: Cploss for 3, 30 degree slots per plate case

Tangential Blowing

The final effort towards flow control in support of this thesis was the use of tangential blowing. Tangential blowing as opposed to normal blowing directly energizes the boundary layer proving to be most effective for separation control. The plates for this configuration had 4 slots with a length of 25.4 mm and a depth of 1.5 mm so as to have the same mass flux as for the 5 slot plates. Tangential blowing required careful internal profiling as shown in Figure 77 to correctly vector the flow at approximately 10 degrees to the wall. Tangential blowing was only attempted for 2nd bend while as distortion from 1st bend could be suppressed by almost any of the tried flow control configuration. 5 Stream wise slots configuration, which had proved most effective among the normal blowing case was used for the 1st bend. Tangential blowing proved to very effective in controlling separation at second bend as shown in Figure 79. At higher RPMs the distributions show a smooth and sharp recovery with delayed separation. 15000 RPM shows an extremely delayed and weakened separation evident from an almost smooth curve. The face plots show a significant weakening of vortices and diminishing distortion with increasing C_μ. At 15000 RPM or C_μ of 0.01942 the Cp_{loss} shows a reduction of 37% from baseline and a DC_{60} as low as 22% shown in Table 5. Tangential blowing beyond doubt proved to be the most effective configuration among the ones tested in this particular thesis.

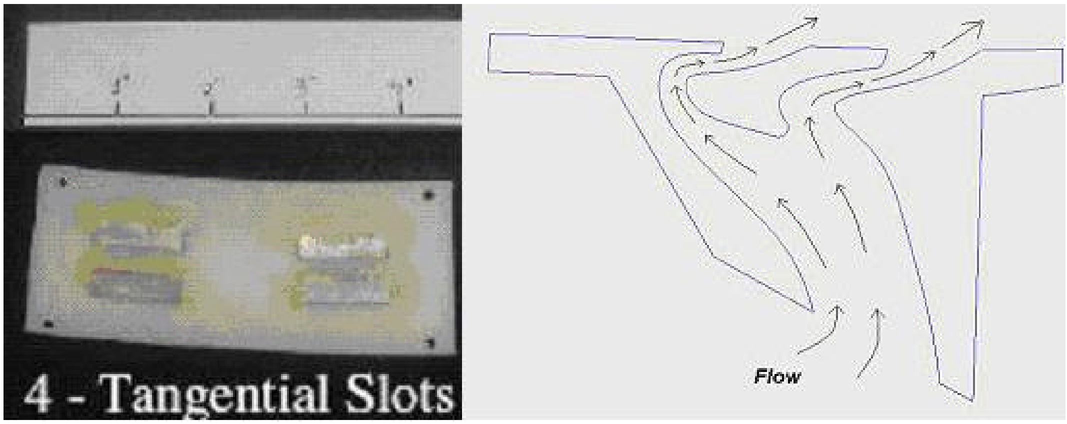

Figure 77: Cross section of tangential blowing plates

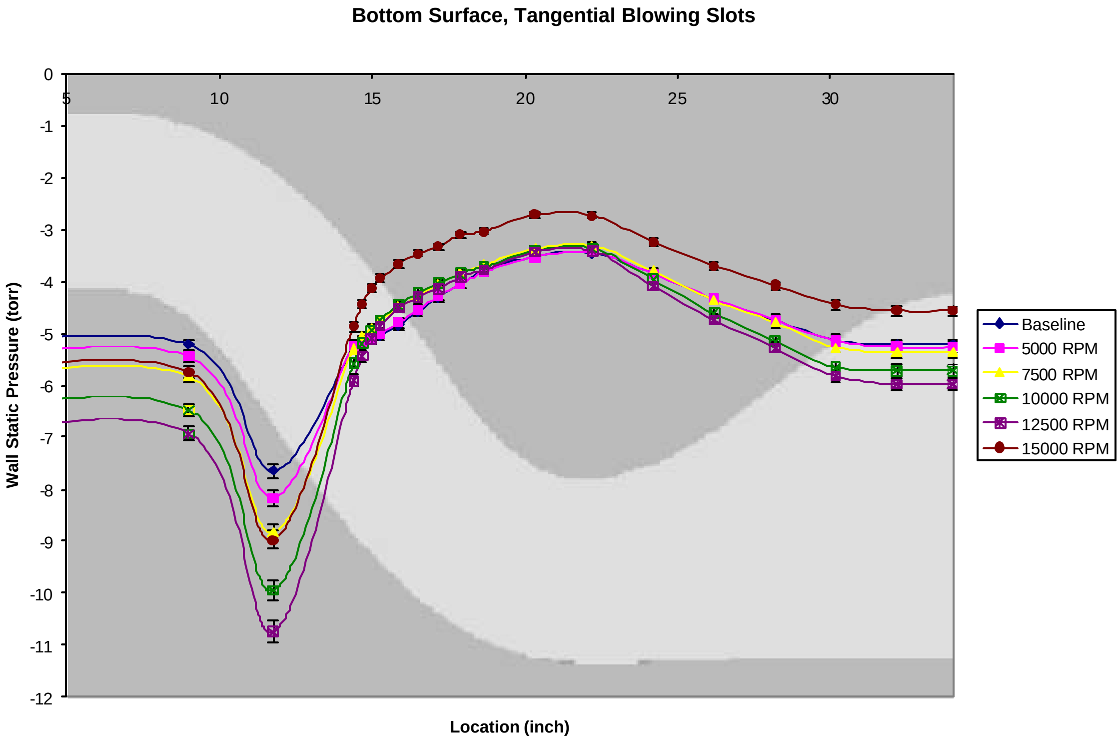

Figure 78: Bottom surface pressures, tangential slots

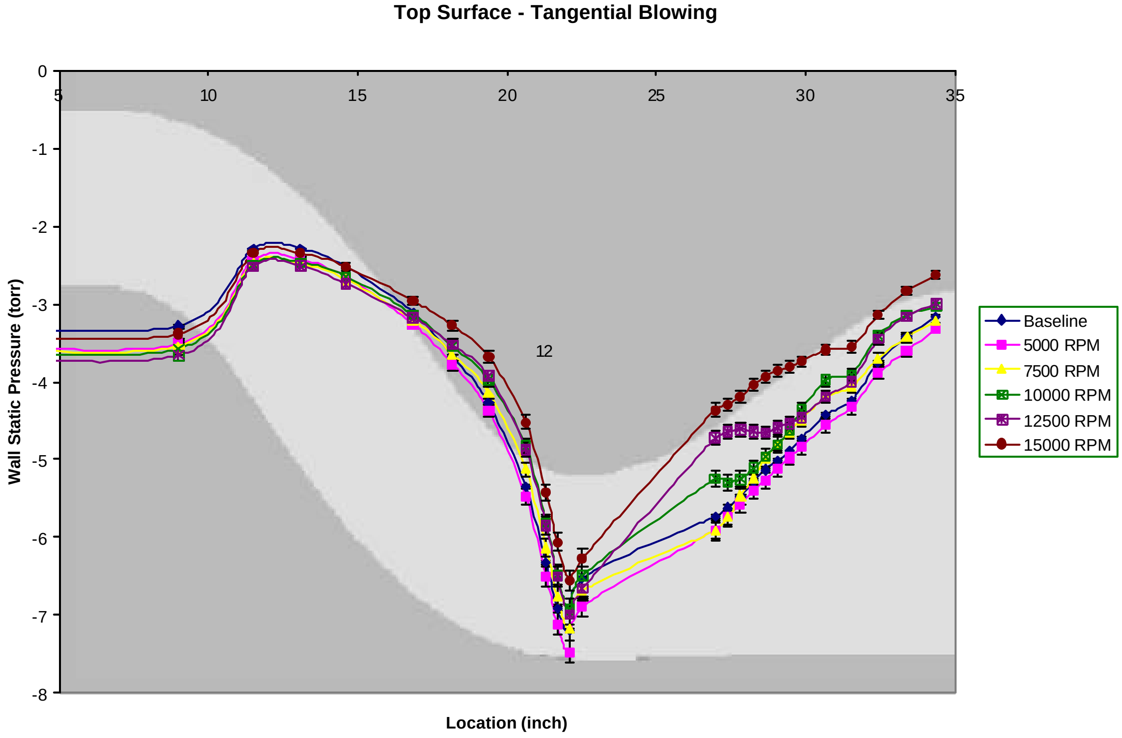

Figure 79: Top surface pressures, tangential slots

Table 5: Duct performance descriptors for tangential blowing

Fan Speed (RPM)	Jet Velocity (m/s)	C_m	Mass Flow	$C_{Ploss,avg}$	DC_{60}
0	0.0	0.0000	0.0 %	58.21±1.11	157.27±6.47
5000	12.5	0.00247	0.59 %	54.73±1.63	138.50±5.808
7500	19.0	0.00572	0.90 %	39.21±1.17	89.03±3.66
10000	25.0	0.00990	1.18 %	29.31±0.94	63.51±2.53
12500	30.0	0.01426	1.42 %	23.87±0.76	40.35±1.823
15000	35.0	0.01942	1.66 %	21.21±0.68	22.90±1.049

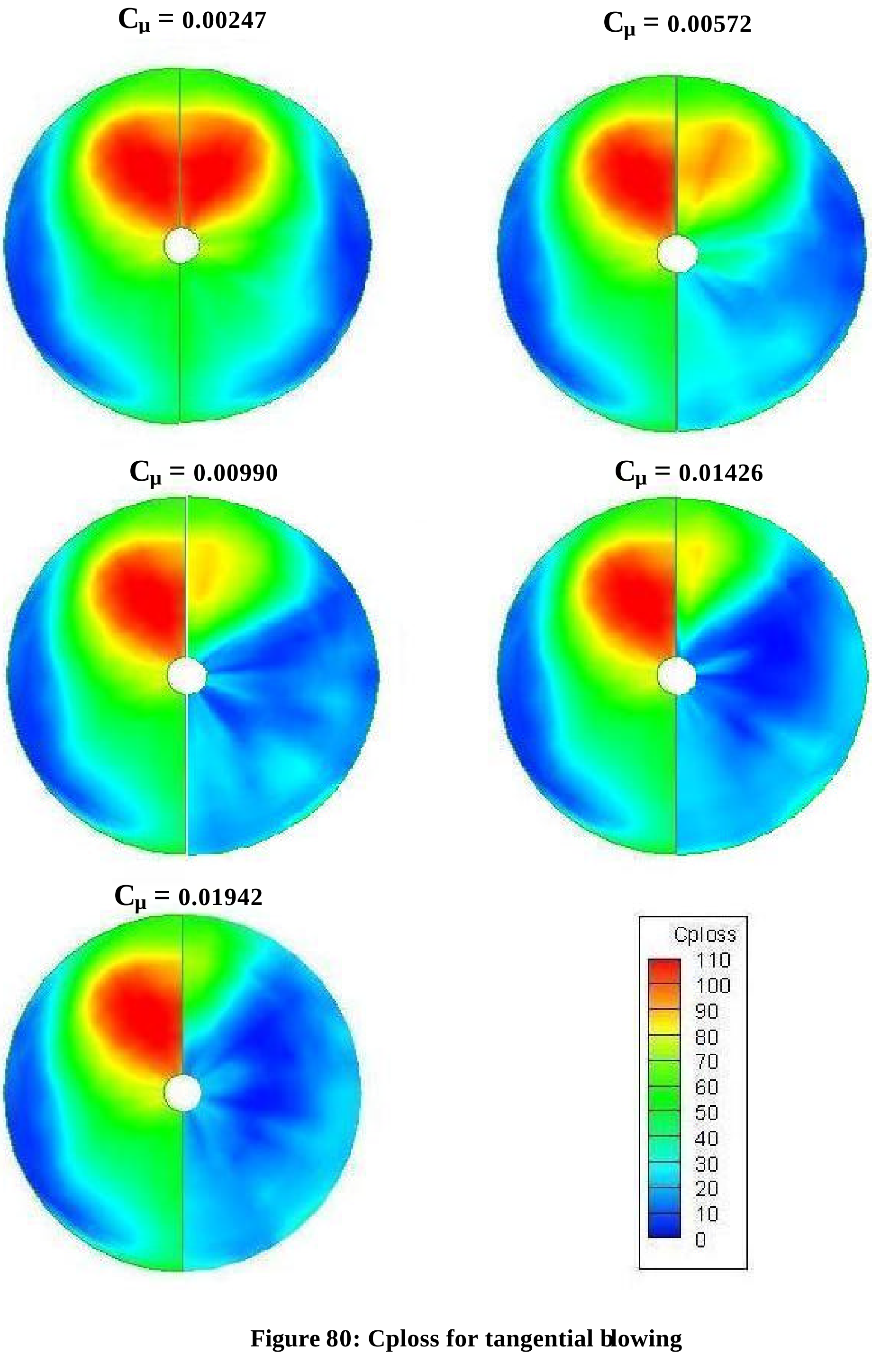

Figure 80: Cploss for tangential blowing

CONCLUSIONS AND RECOMMENDATIONS

The final section of this thesis would summarize the results discussed earlier. Conclusions relevant to the motive of the research would be derived from both experimental and computational studies. Recommendations would be provided based on the conclusions to lead future research on this problem.

Conclusions

Diffusing ducts are integral part of a modern aircraft. These ducts can be modified in shape to get additional advantages including reduction in aircraft size, weight and thermal & radar signature. The serpentine duct analyzed in this problem is designated for use with advanced UCAVs and would greatly reduce the thermal signature of these aircrafts sent out from the engine intake also blocking compressor from incoming radar signal.

The baseline flow which was simulated using experimental and computational models as part of this study showed heavy losses characterized by highly distorted flow at the engine face. These losses were mainly due to development of secondary flows produced at the bends of the S duct dominated by presence of counter rotating vortices. The distorted flow was found to be extremely detrimental for compressor and can greatly decrease the stability limit of the engine, making a stall more likely. The main objective of the study was to develop a good understanding of the underlying flow physics governing the development and propagation of secondary flows followed by implementation of active flow control methods which decrease distortion to an acceptable value if not completely eliminate it. Zero net mass flux modular fluidic actuators integrating blowing and suction were installed at the bends. Though earlier studies with blowing alone showed partial success in pressure recovery at engine the essence of secondary control was in introducing vorticity through synthetic jets capable of countering secondary flow vorticity. It was found, changing the orientation of a straight jet slot with respect to the local free stream could introduce a net vorticity in the desired sense. Initial studies were carried out on CFD which showed the first bend of the S duct less severe compared to the second bend hence use of 1% suction and blowing through stream wise slots showed a complete elimination of flow separation and a greatly reduced or negligible distortion at the engine face. Also the secondary flows due to first bend traveled a longer length downstream before reaching the engine hence had greatly reduced influence at the engine due to diffusion and presence of highly dominant secondary flow structures due to the more recently encountered second bend. The secondary flows due to boundary layer migration at the steeper and more geometrically complex second bend showed much resistance towards standard flow control methods applied at the first bend. Though there were definite improvements over the baseline results at high blowing and suction rates of 1.8% of the total mass flux entering the duct with a Cp_{loss} reduction of 23% and a distortion coefficient reduction of 32%. There was a definite need to better the results to meet acceptable standards. The results were equally supported by both CFD and experimental simulations. As an initial attempt to induce vorticity through synthetic jets, configurations with 5 slots at 30 degree to the local free stream for each plate were installed on the blowing plenum. As seen in earlier tests, an improving trend with increase in actuator mass flux was seen, however the results failed to do any better than stream wise slots. The failure though not explored in depth was attributed to the interference of adjacent jet vorticity as seen in CFD simulations. The next step was to use plates with lesser slots (3 slots), in hope of higher localized jet momentum and lesser interference from neighboring jets. Though the bench top testing of these configurations showed a marginal increase in momentum per slot over the 5 slot per plate configurations, they were employed mainly in the hope of reaping benefits from the principle of vorticity signature. 3 slot stream wise configurations showed slight improvements over baseline results but definitely could not match up to 5 slot stream-wise slots. The 10 degree slots however showed little improvements over the stream-wise case, assigning some definite credibility to the vorticity negation through slot orientation. Further to the use of angled slots, 30 degree 3 slot configurations were attempted. These plates showed an obvious improvement over earlier 3 slot configurations upto fan RPM of 10000, however beyond 10,000 the effects of flow control deteriorated causing strong secondary vortices with with reduced pressure recovery to reappear. This was similar to the results of CFD showing the failure of angled slots to reduce secondary flows any more than stream wise slots. This unexpected failure of angled slots at high C_μs forced radical changes in blowing configurations. As a final attempt to reduce distortion tangential blowing plates were employed. Tangential blowing proved to be more effective than expected. Though clearly more effective in reenergizing boundary layer than normal blowing, they were somehow able to even reduce distortion to values way below the best normal blowing case. For a maximum jet momentum coefficient of 0.01942, the Cp_{loss} pressure loss descriptor decreased by 37% and the description descriptor was brought down to 22.9% which is close to the acceptable industry standard of 20%. As a final comparison of performance, the Cp_{loss} and DC_{60} variation for the various configurations discussed in this thesis are provided in figure 81 & 82.

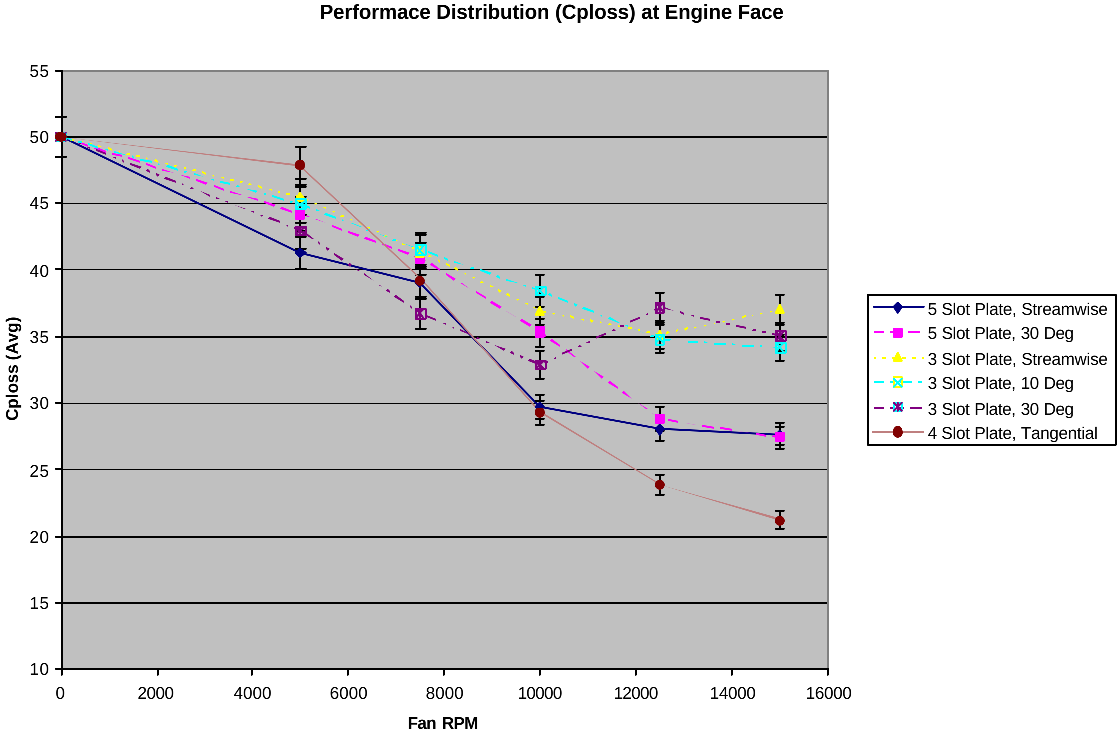

Figure 81: $Cp_{loss,avg}$ comparison for different configurations

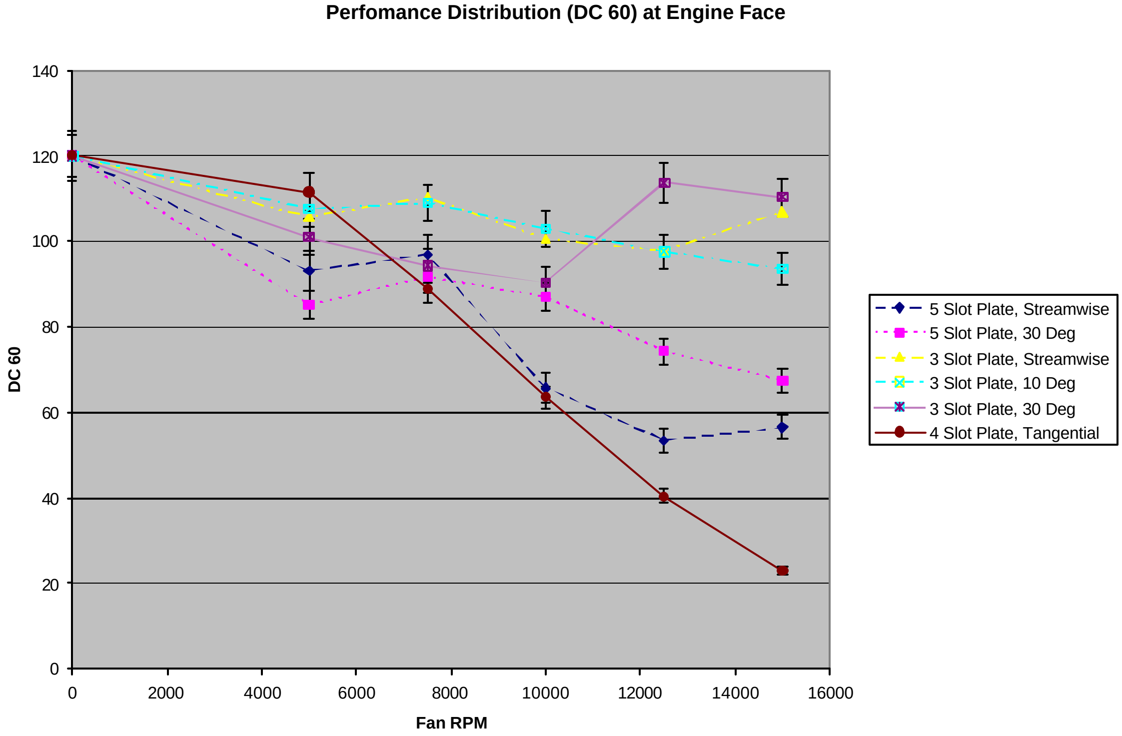

Figure 82: DC$_{60}$ comparison for different configurations

Recommendations

Various observations and occurring over the length of the project have opened areas for further exploration and betterment pertaining to this duct problem and flow control in general. Of the areas with immediate interests, synthetic jet slot orientation definitely requires further investigations. The interaction of slanted jets normal to the surface require better understanding which can have definite improvements in flow control implementations. One of the major short coming of this research could have been the placement of the SJA assembly, boundary layer migration as indicated by earlier studies is irreversible once initiated and its prevention relates a lot to the positioning of the suction and blowing plenums. The positioning of the current actuator may be reconsidered and accordingly altered to optimize the effect of flow control.

Earlier attempts at Texas A&M University had attempted the use of pulsed blowing in the hope of matching natural frequencies of separation and increase the effectiveness of blowing. This however proved to be highly ineffective due to a loss in average jet momentum. Blowing pulsation can be reattempted with use of compressed air which is able to conserve the average jet momentum hence giving higher peak velocities at the times of jet ejections.

Of the various problems encountered during experimental testing, the susceptibility of the actuator setup to physical failure was one of the major hindrances. The ABS plastic though reasonably strong, showed poor resistance to heat and vibrations. Higher RPMs always posed threat to the actuator setup and hence there was always a need for a better cooling system and dampers for motors.

Further to recommendations, the essence of using active control over passive control lies in the ability to control the amount and characteristics of the synthetic jets with flow conditions. Though this study featured only open loop control, closed loop systems would be a practical solution for industrial applications. This would require real time monitoring of the flow within the duct through worthy sensing device able to resolve the deciding parameters such as the separation and liftoff locations, span of separation and vortex strengths.

Recommendations for CFD include use of better grid development methods and use of wall Y_{plus} estimates, further control over turbulence models through a more suitable specification of model constants. Also the boundary conditions can be better understood and specified for a more accurate problem definition.

REFERENCES

[1] Anderson, B. H., Gibb, J., "Vortex Generator Installation Studies on Steady State and Dynamic Inlet Distortion." AIAA Paper 96-3279, July 1996.

[2] Towne, C. E., "Computation of Viscous Flow in Curved Ducts and Comparison with Experimental Data." AIAA Paper 84-0531, January 1984.

[3] Scribben, A. R, Ng, W., Burdisso, R., "Effectiveness of a Serpentine Inlet Duct Flow Control Technique at Design and Off Design Simulated Flight Conditions." *Journal of Turbomachinery*, Vol. 44, April 2006, pp. 332-339.

[4] Anabtawi, A. J., Blackwelder, R. F., Lissaman, P. B. S. and Liebeck, R. H., "An Experimental Investigation of Boundary Layer Ingestion in a Diffusing S-Duct with and without Passive Flow Control," AIAA Paper 99-0739, January 1999.

[5] Anabtawi, A. J., Blackwelder, R . J., Lissaman, P. B. S. and Liebeck, R. H., "An Experimental Study of Vortex Generators in Boundary Layer Ingesting Diffusers with a Centerline Offset," AIAA Paper 99-2110, June 1999.

[6] Reichert, B. A. and Wendt, B. J., "Improving Diffusing S-Duct Performance by Secondary Flow Control," AIAA Paper 94-0365, January 1994.

[7] Reichert, B. A. and Wendt, B. J., "The Effects of Vortex Ingestion on the Flow in a Diffusing S-Duct," NASA *Technical Memorandum 106652*, June 1994.

[8] Sullerey, R. K., Mangat, V. S. and Padhi, A., "Flow Control in Serpentine Inlet Using Vortex Generator Jets," AIAA Paper 2006-3499, June 2006

[9] Kumar, V. and Alvi, F. S., "Use of Supersonic Microjets for Active Separation Control in Diffusers," AIAA Paper 2003-4160, June 2003.

[10] Kumar, V., and Alvi, F. S., "Use of High-Speed Microjets for Active Separation Control in Diffusers," *AIAA Journal*, Vol. 44, No.2, Feb. 2006, pp. 273-281.

[11] Pradeep, A. M. and Sullerey, R. K., "Secondary Flow Control in a Circular S-Duct Diffuser Using Vortex Generator Jets," AIAA Paper 2004-2615, July 2004.

[12] Amitay, M., Pitt, D. and Glezer, A., "Separation Control in Duct Flows," *Journal of Aircraft*, Vol. 39, No. 4, July – Aug 2002, pp. 616-620.

[13] Harper, D. K., "Boundary Layer Control and Wall-Pressure Fluctuations in a Serpentine Inlet," M.S. Thesis, Mechanical Engineering Department, Virginia Polytechnic Institute and State University, Blacksburg, VA, May 2000.

[14] Bridges, A. and Smith, D. R., "The Influence of Orifice Orientation on the Interaction of a Synthetic Jet with a Turbulent Boundary Layer," AIAA Paper 2001-2774 June 2001.

[15] Kirk, A. M., "Active Flow Control in an Advanced Serpentine Jet Engine Inlet Duct," M.S. Thesis, Aerospace Engineering Department, Texas A&M University, College Station, TX, December 2006.

[16] Peifen, W. and Jue, D., "Numerical Analysis of Three-Dimensional Flows Inside / Outside a Submerged Air Inlet under Maneuver," AIAA Paper 2003-4138, June 2006.

[17] Marvin, J. G., "Perspective on Computational Fluid Dynamics Validation," *AIAA Journal*, Vol. 33, No. 10, Oct. 1995, pp. 1778-1787.

[18] Xiong, C., Ya, Z, Changsheng, Z. and Yutao., "Numerical Simulation on Ramjet Inlet with Different Cowl Leading Edge," AIAA Paper 2005-5288, June 2005.

[19] Bahar, C., Alemdaroglu, N. and Özyörük, Y., "Euler Solutions for a Medium Range Cargo Aircraft," AIAA Paper 2002-0402, January 2002.

[20] Ding. J. and Weng, P. F., "Numerical Simulation of Separated Flows around Missile / Inlet," AIAA Paper 2003-4404, July 2003.

[21] Taskinoglu, E. S. and Knight, D. D, "Design Optimization for Submerged Inlets- Part I," AIAA Paper 2003–1247, January 2003.

[22] Jirasek, A., "Vortex-Generator Model and Its Application to Flow Control," *Journal of Aircraft*, Vol. 42, No. 6, Nov.–Dec. 2005, pp. 1486-1491.

[23] Gribben, B. J., Badcock, K. J. and Richards, B. E., "Towards Automatic Multiblock Topology Generation," AIAA Paper 99-3299, 1999.

[24] Logan, R. W. and Nitta, C. K., "Comparing 10 Methods for Solution Verification, and Linking to Model Validation," *Journal of Aerospace Computing, Information, and Communication*, Vol. 3, July 2006, pp. 354-373.

[25] Anderson, B. H. and Gibb, J., "Study on Vortex Generator Flow Control for the Management of Inlet Distortion," *Journal of Propulsion and Power*, Vol. 9, No. 3, pp. 422-430, June 1993.

[26] Mohler, S. R., Jr., "Wind-US Flow Calculations for the M2129 S-Duct Using Structured and Unstructured Grids," AIAA Paper 2004–0525, December 2003.

[27] SAE Committee S-16, Turbine Engine Inlet Flow Distortion, "Aerospace Recommended Practice: Gas Turbine Engine Inlet Flow Distortion Guidelines," ARP 1420, Society of Automotive Engineers, June 1977.

[28] Gilarranz, J. L., Traub, L. W. and Rediniotis, O. K., "Characterization of a Compact, High-Power Synthetic Jet Actuator for Flow Separation Control," AIAA Paper 2002-0127, January 2002.

[29] Harper, D. K., Leitch, T. A., Ng, W. F., Guillot, S. G. and Burdisso, R. A., "Boundary Layer Control and Wall-Pressure Fluctuations in a Serpentine Inlet," AIAA Paper 2000-3597, July 2000.

[30] Kim, J. H., Simmon, T. W., Viskanta, R., " Journal of Heat Transfer Policy on Reporting Uncertainties in Experimental Measurements and Results", *Journal of Heat Transfer*, Vol. 115, February 2003, pp. 5-6.

[31] Kline, S. J. and McClintock, F. A., "Describing Uncertainties in Single-Sample Experiments," *Mechanical Engineering*, Vol. 75, pp. 3-8, January 1953.

[32] Feakins, S. H., MacMartin, D. G. and Murray, R. M., "Dynamic Separation Control in a Low-Speed Asymmetric Diffuser with Varying Downstream Boundary Condition," AIAA Paper 2003-416, 2003.

[33] Guy, Y., McLaughlin, T. E. and Mo, J. A., "Velocity Measurements in a Synthetic Jet," AIAA Paper 2001-0118, January 2001.

[34] Amitay, M., Pitt, D., Kibens, V., Parekh, D. and Glezer, A., "Control of Internal Flow Separation Using Synthetic Jet Actuators," AIAA Paper 2000-0903, January 2000.

VITA

Name: Abhinav Kumar

Address: c/o Dr. Othon Rediniotis
H.R. Bright Building, Rm. 631A
3141 TAMU
College Station, TX 77843-3141

Education: B.E., Mechanical Engineering, Mumbai University, 2005
M.S., Aerospace Engineering, Texas A&M University, 2007